Experimental studies of flow control techniques for future aircraft

Thesis by
Emile Kazuo Oshima

In Partial Fulfillment of the Requirements for the
Degree of
Doctor of Philosophy

CALIFORNIA INSTITUTE OF TECHNOLOGY
Pasadena, California

2023
Defended December 16, 2022

Emile Kazuo Oshima
ORCID: 0000-0002-1689-3726

ACKNOWLEDGEMENTS

This thesis would not have been possible without the support, guidance, and encouragement of countless people. I will make every effort to thank all of you personally in the coming months.

First, I would like to extend my deepest gratitude toward my advisor Dr. Mory Gharib and unofficial co-advisor Dr. Israel Wygnanski. Their different mentorship styles and areas of expertise helped me grow tremendously as a scientist. Thank you for taking me under your wings and challenging me with such diverse and fulfilling opportunities. Special thanks to the other committee members Dr. Tim Colonius, Dr. John Dabiri, and Dr. Jane Bae.

To those who have been a part of my research journey: it was an absolute pleasure working with or alongside you. Gharib group members past and present, collaborators, GALCIT colleagues, administrative staff, APS reunion buddies – I truly appreciate your insights, feedback, conversations, and company.

To those friends who added color to my life outside the lab: you are the reason I made it through. I am grateful for your energy during fun times and patience during stressful times. Whether you saw me on campus every week or kept in touch remotely, thank you for being a part of my Caltech experience.

And finally, to my family: thank you for keeping my life on course and in perspective. All my successes and happinesses are reflections of your unconditional and unwavering love. This thesis is dedicated to you.

Many components of the swept wing model used in Part I were initially designed by Damian Hirsch and Stephanie Rider (Gharib, D. Hirsch, et al., 2016) and Marcel Veismann.

The author of this thesis has received financial support from the Foster and Coco Stanback Fellowship; the Center for Autonomous Systems and Technologies; the Ohio Aerospace Institute to support an Air Force Research Laboratory contract; the DARPA CRANE program in partnership with Aurora Flight Sciences; the Center for Teaching, Learning & Outreach; and the Boeing Company University Innovation Leadership program.

ABSTRACT

From the signing of the Paris Agreement to the COVID-19 outbreak, the past decade has truly challenged the aviation industry to adapt. New technologies need to be developed constantly to meet the increasing commercial and defense demands for more efficient, quiet, safe, and agile aircraft. To keep up with these rapidly changing times, an approach that marries a fundamental understanding of aerodynamics with systems design and optimization is necessary. This thesis explores two promising concepts for controlling flow over next-generation aircraft: active control on a swept wing for airplane applications, and passive control on a rotating blade for drone applications. In each, force measurements are combined with advanced flow visualization techniques to create a research framework that is both data-driven and physics-informed.

In Part I, a comprehensive wind tunnel campaign is carried out on a swept wing model of modular geometry equipped with an array of sweeping jet actuators, which have demonstrated tremendous promise for flow control authority in both laboratory settings and full-scale flight tests. The flow physics and performance of the wing is investigated first without actuation, revealing separation behaviors at both the leading and trailing edges that are crucial to consider when flow control is applied. This paves the way for an optimization study in a newly proposed framework that relies on fluid power coefficients rather than the momentum coefficient that has been the accepted parameter of choice for characterizing blowing systems over the past seven decades of active flow control research.

Part II explores the feasibility of a "prop-shroud" concept for small-scale aerial vehicles, in which the shroud is directly attached to the blade tips and thus co-rotates with the propeller. Such a configuration has the potential to provide the various aerodynamic and engineering benefits of a shrouded propeller without the associated costs and complexities of its installation. The hover efficiency of a prop-shroud is shown to be comparable to commercially available drone propellers, even without a rigorous optimization of its geometry. The effect of the co-rotating shroud is then analyzed in detail on the time-averaged, phase-averaged, and unsteady features of the flow field. A model based on vortex formation time is developed, laying out a foundation for future research and understanding.

PUBLISHED CONTENT AND CONTRIBUTIONS

Oshima, E., Lee, N., Gharib, M., Lee, V., and Khodadoust, A. (2023). "Development of a physics-informed neural network to enhance wind tunnel data for aerospace design". In: *AIAA SciTech 2023 Forum*. National Harbor, MD: AIAA. DOI: 10.2514/6.2023-0540.

E.O. participated in the conception of the project, prepared the manuscript, and closely worked with and mentored N.L. (undergraduate researcher at the time of writing) in algorithm development. A previous Master's exchange student, Pablo Hermoso Moreno, was also involved in the conception of the project.

Oshima, E., Gharib, M., Reichert, J., and Wygnanski, I. (2022). "On the use of power-based parameters for blowing active flow control systems". In: *AIAA Journal*. DOI: 10.2514/1.J061419.

This journal article is based on the conference paper "Parameters defining active flow control" (2021). E.O. prepared the manuscript collaboratively with I.W.

Oshima, E., Gharib, M., and Wygnanski, I. (2022). "Interactions between the leading-edge vortex and sweeping jet actuators on a simple swept wing". In: *AIAA SciTech 2022 Forum*. San Diego, CA: AIAA. DOI: 10.2514/6.2022-2426.

E.O. performed the experiments, analyzed the data, and participated in the writing of the manuscript.

Oshima, E., Gharib, M., Reichert, J., and Wygnanski, I. (2021). "Parameters defining active flow control". In: *AIAA Aviation 2021 Forum*. virtual: AIAA. DOI: 10.2514/6.2021-2855.

E.O. performed the experiments on the swept wing at Caltech, analyzed the data, and wrote the manuscript collaboratively with I.W. Experiments on the elliptical airfoil at the University of Arizona were performed by J.R., and E.O. participated in the data analysis and preparation of the associated figures, which have been reproduced in Chapter 3 of this thesis.

TABLE OF CONTENTS

Acknowledgements . . . iii
Abstract . . . iv
Published Content and Contributions . . . v
Table of Contents . . . v
List of Illustrations . . . viii
List of Tables . . . xv
Nomenclature . . . xvi

I Sweeping jet actuators on swept wings of finite aspect ratio 1
Chapter I: Introduction . . . 2
1.1 Objectives . . . 3
1.2 Sweeping jet actuators and active flow control . . . 3
1.3 Experimental setup . . . 6
1.4 Parameter definitions . . . 9
Chapter II: Characterization of baseline flow and performance . . . 14
2.1 Lift, drag, and LEV formation dynamics . . . 15
2.2 Pitch stability . . . 20
2.3 Effect of flap deflection . . . 31
2.4 Validation of *Re* and tufting effects . . . 34
Chapter III: Fluid power coefficients and system design . . . 40
3.1 Momentum vs power coefficients . . . 41
3.2 Measuring power coefficients on the swept wing . . . 47
3.3 Integration of AFC into systems design . . . 50
Chapter IV: Understanding and optimization of AFC . . . 55
4.1 Interactions at the leading and trailing edges for lift enhancement . . . 55
4.2 Drag reduction and cruise efficiency . . . 59
4.3 Pitch control and stabilization . . . 61
Chapter V: Concluding remarks & future work . . . 69

II Propellers with co-rotating shrouds 72
Chapter VI: Introduction . . . 73
6.1 Objectives . . . 75
6.2 Experimental Setup . . . 76
Chapter VII: Comparisons of hover performance in air . . . 80
7.1 Validation of prototyping methodology . . . 81
7.2 Shroud geometry comparisons . . . 83
Chapter VIII: Effect on the steady-state wake . . . 87

8.1 Time-averaged velocity and vorticity fields 87
8.2 Vorticity distribution 93
Chapter IX: Unsteady dynamics of the starting vortex ring 98
9.1 Overview of the phenomenon 99
9.2 Vortex propagation and growth 102
9.3 Analogy with vortex ring formation time 108
Chapter X: Concluding remarks & future work 115
Bibliography 118

LIST OF ILLUSTRATIONS

Number *Page*

1.1 Airbus A32X family of aircraft share the same vertical tail design even though body length differs by over 40% (31.44 to 41.51 m), adapted from (Scavini, 2011). 2

1.2 (a) Lift and (b) form drag measured on a NACA 0015 airfoil at $Re = 5 \times 10^5$ with flap deflection $\delta = 20°$, redrawn using data digitzed from (Seifert et al., 1993). 5

1.3 Schematic of the internal geometry of a sweeping jet actuator, adapted from (Cattafesta and Sheplak, 2011). 6

1.4 CAD drawings of the three-element configurations of the MOBLE model tested in the subsonic Lucas Wind Tunnel facility at Caltech (dimensions in mm). 8

1.5 Schematic of the MOBLE wing assembly and its plumbing, with various components labeled. 9

1.6 Tools required to make the fluorescent tufts. 9

1.7 Images of the two-element MOBLE model installed in the LWT test section. A triangular turbulator strip is installed across the entire span at $x/c = 0.08$. Tufts made of UV-fluorescent thread visualize the surface flow over the suction side of the wing. 10

1.8 LAVLET airfoil cross-section geometry with conventions for lift, drag, and pitching moment coefficients. 10

2.1 Lift and drag performance for the three A_R tested at (a,c,e) $\Lambda = 30°$ and (b,d,f) $\Lambda = 45°$. Markers are colored at maximum lift (blue) and glide ratio (green). 16

2.2 Superposition of tuft images taken at α immediately before (red) and after (blue) LEV inception for different A_R at $\Lambda = 30°$. 17

2.3 Superposition of tuft images taken at α immediately before (red) and after (blue) LEV inception for different A_R at $\Lambda = 45°$. 17

2.4 (a,b) Lift slope $dC_L/d\alpha$ and (c,d) drag slope $dC_D/d\alpha$ of all six wing configurations. Markers are colored at LEV inception (red). 19

2.5 Empirically derived stability boundary of various wing planforms. Typical design areas of subsonic transport aircraft (blue) and combat jet aircraft (red) are shown, as well as the parameter space of the tested MOBLE configurations (gray). 21
2.6 (a,c) Drag and (b,d) pitching moment polars for all wing configurations. 22
2.7 Comparisons of the pitching moment curve as the longitudinally stable $\Lambda = 30°$, $A_R = 2.6$ wing is made unstable through an increase in Λ and A_R. 24
2.8 Progression of the surface flow field as C_L is increased on the two-element wings. (a,b) $C_L = 0.3$, (c,d) $C_L = 0.5$, and (e,f) $C_L = 0.7$. Dashed red lines indicate the MRP. 25
2.9 Comparison of the surface flow field at $\Lambda = 30°$ on the stable $A_R = 2.6$ wing and unstable $A_R = 3.8$ wing. (a,b) $C_L = 0.7$, (c,d) $C_L = 0.9$. . . 27
2.10 Pitching moment curves for (a) all stable configurations and (b) all unstable configurations extended to the high α range. Pink lines indicate the overall trend of $dC_{LM}/d\alpha$. 29
2.11 Tuft visualizations of LEV propagation at high α. (a) Stable $\{\Lambda = 30°, A_R = 2.6\}$ wing at $\alpha = 16°, 17°, 19°$. (b) Unstable $\{\Lambda = 45°, A_R = 3.2\}$ wing at $\alpha = 11°, 13°, 17°$. 30
2.12 Tuft visualizations on the $\Lambda = 45°$, $A_R = 3.2$ wing when the flap is deflected to $\delta = 15°$ and $30°$. 32
2.13 (a,b) Lift and (c,d) drag performance on the three-element wings at different flap deflections. $C_{L,D}$ are plotted with open markers and $dC_{L,D}/d\alpha$ are plotted with dots. 33
2.14 Re dependence of C_L, C_D, and C_{LM} for different α and δ on the $\Lambda = 30°$, $A_R = 1.3$ wing. 35
2.15 Repeatability of C_L, C_D, and C_{LM} measurements across ten trials on $\Lambda = 45°$, $A_R = 3.2$, $\delta = 0°$ at $Re = 1.0 \times 10^6$. 35
2.16 Uncertainty across the ten trials reported in Figure 2.15, computed as the ratio of standard deviation to the mean. 36
2.17 Effect of Re and tufts on the drag and pitching moment polars of the $\Lambda = 30°$, $A_R = 3.8$ wing. 36
2.18 Effect of tufting on the changes effected by AFC on the $\Lambda = 45°$, $A_R = 3.2$, $\delta = 0°$ wing. All $n_j = 36$ actuators are active at five different levels of C_μ. 38

2.19 Effect of Re on the changes effected by AFC on the $\Lambda = 30°$, $A_R = 1.3$ wing oriented at $\alpha = 8°$, $\delta = 30°$. 39
3.1 Variation of lift on a thick airfoil with (a) C_Q, (b), $C_{\mu,inc}$ and $C_{\pi,0}$. Data from (Poisson-Quinton, 1948), taken at $\delta = 45°$ and $Re = 0.9 \times 10^6$, was digitized and recast in terms of the plenum power coefficient. . . 41
3.2 (a) Elliptical airfoil in the University of Arizona wind tunnel, and (b) a schematic drawing of its cross-section at $\alpha = 0°$ and $\delta = 15°$. Only TE blowing is used. 43
3.3 Lift increment ΔC_L due to steady blowing supplied by a centrifugal blower with minimal internal losses. The C_μ was estimated from (a) flow rate measurement and (b) Bernoulli's equation. 44
3.4 Dependence of ΔC_L on (a) $C_{\mu,mod}$ and (b) $C_{\pi,0}$ with the blower setup. 45
3.5 Dependence of ΔC_L on (a) $C_{\pi,0}$ and (b) $C_{\pi,sys}$ with the compressed air setup. Light gray points are from the blower setup (Figure 3.4(b)). 46
3.6 Ashcroft pressure gauge setup for calibrating plenum pressure on the swept wing model. 47
3.7 Calibration of plenum pressure p_0 against (a) flow rate $\dot{m}_j$ and (b) pressure p_t measured at the system inlet. 48
3.8 Plenum calibration data plotted on a per-actuator basis to validate the uniformity assumption. (a) The x-values of Figure 3.7(a) have been divided by the respective n_j, and (b) different actuators in the array are tested individually (Act 1 is closest to the wing root). 49
3.9 Relative pressure losses in the supply chain as a function of mass flow rate per actuator on the $\Lambda = 45°$ wing at different A_R for a fixed actuator spacing ξ_s. 49
3.10 Effect of operational geometry (α, δ) for a fixed wing planform geometry ($\Lambda = 30°$, $A_R = 1.3$) and actuator distribution $n_j = 12$. . . . 50
3.11 Effect of wing planform geometry (Λ, A_R) and actuator distribution sparsity on ΔC_L for a fixed operational geometry ($\alpha = 8°$, $\delta = 30°$). . 51
3.12 Dependence of ΔC_L on (a) $C_{\mu,inc}$, (b) $C_{\pi,0}$, and (c) $C_{\pi,sys}$ for different actuator distributions (left schematic) for fixed $n_j = 12$ and wing geometry $\Lambda = 45°$, $A_R = 3.2$, $\alpha = 8°$, $\delta = 30°$. (d) Fluid power losses incurred in the supply chain as a function of total system input power. 52

4.1 Comparison of lift (solid lines) and lift slope (dashed lines) when $n_j = 18$ SJAs are uniformly distributed across the three-element wing. (a) $\Lambda = 30°$, $\delta = 0°$, (b) $\Lambda = 45°$, $\delta = 0°$, (c) $\Lambda = 30°$, $\delta = 30°$, (d) $\Lambda = 45°$, $\delta = 30°$. 56
4.2 Comparison of lift increment (solid lines) and drag slope (dashed lines) for the same configurations as Figure 4.1. (a) $\Lambda = 30°$, $\delta = 0°$, (b) $\Lambda = 45°$, $\delta = 0°$, (c) $\Lambda = 30°$, $\delta = 30°$, (d) $\Lambda = 45°$, $\delta = 30°$. . . . 58
4.3 Effect of different spanwise actuation locations at $C_\mu = 2.0\%$ on (a) lift and (b) drag of the $\Lambda = 45°$, $A_R = 2.3$, $\delta = 0°$ wing, and (c) tuft visualization of root actuation at $\alpha = 16°$. 60
4.4 Tuft visualizations of the changes in LEV behavior with spanwise actuation location on the $\Lambda = 45°$, $A_R = 3.2$, $\alpha = 8°$, $\delta = 30°$ wing. . 60
4.5 (a) Pitching moment curves of the $\Lambda = 45°$, $A_R = 2.3$ wing at different C_μ with all $n_j = 24$ actuators. (b) C_μ required at every α to maintain trim ($C_{LM} = 0$) and the resulting C_L. 62
4.6 (a) $C_{\mu,trim}$ for different actuator distributions on the $\Lambda = 45°$, $A_R = 2.3$ wing, and (b) the resulting L/D at trim. 63
4.7 Tuft visualizations show the region of influence of each actuator distribution over the flow at the trailing edge. The MRP is indicated as a dashed black line. 63
4.8 (a) Baseline pitching moment curve of the $\Lambda = 45°$, $A_R = 2.3$ wing as MRP is varied. (b) C_μ required to maintain trim using Jets 13-18 at the desired C_L. Values are provided in Table 4.1. 65
4.9 Effect of a single actuator activated at $C_\mu = 0.1\%$ at different spanwise locations on (a) pitching moment polar and (b) lift increment of the unstable $\Lambda = 30°$, $A_R = 3.8$ wing. The gray region corresponds to the uncertainty in the baseline curve across all tests. 67
4.10 Effect of a single actuator activated at $C_\mu = 0.1\%$ at different spanwise locations on (a) pitching moment polar and (b) lift increment of the stable $\Lambda = 30°$, $A_R = 2.6$ wing. The gray region corresponds to the uncertainty in the baseline curve across all tests. 68
6.1 The Stipa-Caproni aircraft whose fuselage was an "intubed propeller" (Aviation History, 1932). 74
6.2 Reynolds number range for various flight vehicles, adapted from (Mueller, 1999). 74

6.3 (a) Isometric, (b) front, and (c) cross-sectional views of the "prop-shroud" geometry. 77
6.4 Experimental setup in air showing the prop-shroud mounted to the integrated *RC Benchmark* test stand. 78
6.5 (a) Isometric, (b) front, and (c) transparent side views of the stationary shroud mounted to the test stand. 78
6.6 Experimental setup in water showing (a) the flow visualization components and (b) a zoomed-in view of the propeller test rig. 79
7.1 (a) Commercially available propeller for small-scale multicopters and (b) 3D-printed propeller with the same diameter. Their airfoil thicknesses are compared in (c). 82
7.2 Hover performance of two 3D-printed propellers compared with an off-the-shelf propeller of the same diameter. (a) Thrust, (b) torque, (c) efficiency, and (d) figure of merit. 83
7.3 Comparisons of stationary and rotating shrouds for different shroud lengths h. The same hover performance metrics as those in Figure 7.2 are used. 84
7.4 Comparison of different rotating shroud profiles for $h/c = 1$, using the same hover performance metrics as those in Figure 7.2. 85
8.1 Time-averaged velocity field around the baseline propeller at $\Omega = 53$ rad/s. (a) 2D velocity field showing both magnitude and direction, and (b,c) profiles of horizontal & vertical velocity component at select streamwise locations corresponding to the color of the dashed line in (a). 88
8.2 Time-averaged velocity field around the propeller with symmetric shroud at $\Omega = 53$ rad/s. 90
8.3 Time-averaged velocity field around the propeller with cambered shroud at $\Omega = 53$ rad/s. 90
8.4 Jet momentum produced by the three tested propellers as a function of streamwise distance. 92
8.5 Jet momentum as a function of streamwise distance for different rotation rates of the (a) baseline propeller, (b) propeller with symmetric shroud, and (c) propeller with cambered shroud. Dashed lines represent the mean thrust produced at each Ω. 92
8.6 Time-averaged vorticity field of the three propeller designs at $\Omega = 53$ rad/s. 94

8.7 Phase-averaged vorticity fields of the baseline propeller at Ω = 62 rad/s, spaced 20° apart in angular position. 95
8.8 Phase-averaged vorticity field of the three propeller designs at Ω = 62 rad/s. 96
9.1 Visualization of vortices that form as an airfoil is impulsively started and stopped. Adapted from Figure 55 of (Prandtl and Tietjens, 1934). 99
9.2 Pathlines (exposure = 25 ms) visualizing the development and propagation of the starting vortex as the baseline propeller is accelerated from rest. 100
9.3 Pathlines (exposure = 25 ms) visualizing the development and propagation of the starting vortex as the propeller with cambered shroud is accelerated from rest. 101
9.4 Raw and filtered thrust signals during startup of the (a) baseline propeller and (b) propeller with cambered shroud. 102
9.5 Total circulation in the FOV for the (a) baseline and (b) shrouded propellers, as well as the (c,d) positive and (e,f) negative decomposition. Three cases of propeller stopping time t_s are shown. 103
9.6 Positive, negative, and total circulation in the FOV for the t_s = 1.0 s cases of (a) the baseline propeller and (b) shrouded propeller. 104
9.7 Pathline visualizations (exposure = 50 ms) of the six cases presented in Figure 9.5 as the starting vortex reaches the edge of the FOV. . . . 105
9.8 Different methods used to locate the vortex center at t = 0.5 s on the baseline propeller. (a) Velocity field and magnitude, (b) pathlines with 20 ms exposure, (c) vorticity, and (d) vortex discriminant. 106
9.9 Different methods used to locate the vortex center at t = 0.5 s on the propeller with cambered shroud. (a) Velocity field and magnitude, (b) pathlines with 20 ms exposure, (c) vorticity, and (d) vortex discriminant. 107
9.10 Comparison of vortex propagation path of the two propellers as determined by the vortex discriminant method. Marker color corresponds to time. 107
9.11 Visualization of vortex rings generated by a piston-cylinder apparatus, taken from Gharib, Rambod, and Shariff, 1998. Different stroke ratios were used to vary the formation time $\hat{T}$. 109
9.12 Tracking the position and size of the starting vortex at various times for (a) the baseline propeller and (b) propeller with cambered shroud. 110

9.13 Circulation Γ_v contained within the starting vortex plotted against (a,c) dimensional time and (b,d) dimensionless formation time for the two propellers tested. 111
9.14 The starting vortex grows under different mechanisms (a) at very early times upon initial inception by the blade tip and (b) after it has propagated away from the blades. 112
9.15 Possible mathematical models for the propeller ramp-up velocity profile. 113
9.16 Pathline visualizations of 20 ms exposure time in 10 ms increments, showing the transition into the phase where vortex grows via jet entrainment. Dashed grid is aligned with the vortex center in the first frame (a). 114

LIST OF TABLES

Number *Page*

0.1 Variables in Part I xvii

0.2 Variables in Part II xviii

2.1 Location of MRP and trim offset applied to compute the C_{LM} values. Note that x is measured along the wing root from the LE. 23

2.2 Values of α, C_L, and C_{LM} for tuft visualizations presented in Figures 2.8 & 2.9. The C_L is approximately matched in each image pair. . . . 25

2.3 Effect of Re and tufts on MRP location and required trim offset. . . . 37

2.4 Nominal free stream velocity and Re each wing was tested at. 38

4.1 MRP location and trim offset applied to obtain each of the C_{LM} curves in Figure 4.8. Then, the C_L range over which the wing is trimmed and the maximum C_μ required to achieve trim are provided. 65

7.1 Aggregate performance metrics of the propellers tested in Figure 7.2 based on a quadratic fit of the thrust and torque data. 83

NOMENCLATURE

AC. aerodynamic center.

AFC. active flow control.

BLC. boundary layer control.

DPIV. digital particle image velocimetry.

FM. figure of merit.

FOV. (camera) field of view.

LE. leading edge (of wing).

LEV. leading-edge vortex.

LWT. Lucas Wind Tunnel.

MAV. micro aerial vehicle.

MRP. mean rotation point.

SJA. sweeping jet actuator(s).

TE. trailing edge (of wing).

TES. trailing-edge separation.

VTOL. vertical take-off and landing.

a	=		sound speed [m/s]
b	=		wing span (half wing) [m]
$\mathcal{A}$	=	A_j/S	actuator-to-wing area ratio [-]
A_j	=		total actuator nozzle area [mm^2]
A_R	=	$2b^2/S$	wing aspect ratio [-]
c	=		wing chord [m]
C_D	=	$\frac{F_D}{\frac{1}{2}\rho_\infty u_\infty^2 S}$	drag coefficient [-]
C_L	=	$\frac{F_L}{\frac{1}{2}\rho_\infty u_\infty^2 S}$	lift coefficient [-]
C_{LM}	=	$\frac{M_P}{\frac{1}{2}\rho_\infty u_\infty^2 Sc}$	pitching moment coefficient [-]
$C_\mathcal{M}$	=	$\frac{\dot{m}_j}{\rho_\infty u_\infty S}$	AFC mass flow coefficient [-]
C_Q	=	$\frac{Q_j}{u_\infty S}$	AFC volume flow coefficient [-]
C_μ	=	$\frac{J}{\frac{1}{2}\rho_\infty u_\infty^2 S}$	AFC jet momentum coefficient [-]
C_π	=	$\frac{\rho_j u_j^3 A_j}{\frac{1}{2}\rho_\infty u_\infty^3 S}$	AFC jet power coefficient [-]
$C_{\pi,0}$	=	$4C_\mathcal{M}\frac{p_0-p_\infty}{\rho_\infty u_\infty^2}$	AFC plenum power coefficient [-]
$C_{\pi,sys}$	=	$4C_\mathcal{M}\frac{p_t-p_\infty}{\rho_\infty u_\infty^2}$	AFC system power coefficient [-]
h	=		blowing slot width [cm]
J	=	$\dot{m}_j u_j$	jet momentum flux [kg m/s^2]
$\dot{m}$	=	$\rho u A$	mass flux [kg/s]
n_j	=		number of sweeping jet actuators [-]
p	=		pressure [Pa]
Q	=		volume flow rate [m^3/s]
Re	=	$\frac{u_\infty c}{\nu}$	Reynolds number [-]
S	=		wing planform area [m^2]
Sup_{loss}	=	$\frac{C_{\pi,sys}-C_{\pi,0}}{C_{\pi,sys}}$	relative supply system losses [-]
$\mathcal{T}$	=		thrust [N]
u	=		velocity [m/s]
α	=		angle of incidence [°]
δ	=		flap deflection [°]
Λ	=		wing sweep [°]
ξ_0	=		spanwise location of first actuator [cm]
ξ_s	=		spacing between adjacent actuators [cm]
ρ	=		density [kg/m^3]

Table 0.1: Variables in Part I

c	=		blade chord [m]
d	=		core jet diameter [m]
D_p	=		propeller diameter [m]
$\mathcal{D}$	=	$\left(\frac{\partial u}{\partial x}+\frac{\partial v}{\partial y}\right)^2-4\left(\frac{\partial u}{\partial x}\frac{\partial v}{\partial y}-\frac{\partial u}{\partial y}\frac{\partial v}{\partial x}\right)$	vortex discriminant [s^{-2}]
FM	=	$\sqrt{\frac{2}{\pi}}\frac{k_{\mathcal{T}}^{3/2}}{k_Q}$	figure of merit [-]
h	=		shroud height [m]
J	=		jet momentum [kg m/s^2]
R	=		radius [m]
Re	=	$\frac{u_{tip}c}{\nu}$	Reynolds number [-]
k_Q	=	$\frac{Q}{\rho_\infty \Omega^2 D_p^5}$	torque coefficient [-]
$k_{\mathcal{T}}$	=	$\frac{\mathcal{T}}{\rho_\infty \Omega^2 D_p^4}$	thrust coefficient [-]
Q	=		torque [N·m]
$\mathcal{T}$	=		thrust [N]
t	=		time [s]
$\hat{T}$	=	$\frac{1}{c}\int u_{tip}\,dt$; $\frac{1}{D_p}\int \tilde{u}_{jet}\,dt$	formation time [-]
u	=		streamwise velocity [m/s]
v	=		radial velocity [m/s]
x	=		streamwise coordinate [m]
y	=		radial coordinate [m]
α	=		blade pitch angle [°]
β	=		shroud polar angle [°]
Γ	=	$\int \omega\,dA$	circulation [m^2/s]
ω	=	$\frac{\partial v}{\partial x}-\frac{\partial u}{\partial y}$	vorticity [s^{-1}]
Ω	=		propeller rotation rate [rad/s]
ρ	=		density [kg/m^3]

Table 0.2: Variables in Part II

Part I

Sweeping jet actuators on swept wings of finite aspect ratio

Chapter 1

INTRODUCTION

In the coming decades, commercial fight will be subject to tighter environmental regulations, and military missions will demand higher agility and maneuverability. Safety is also of the highest priority in the aviation industry, requiring aircraft designs to account for emergency situations. This robustness, however, is often traded for manufacturing cost and fuel efficiency.

The vertical tail on a commercial airplane, which primarily provides yaw control, serves as a clear example of how these design constraints play out in practice. The surface is sized to overcome the worst-case scenario of an engine failure at low speed in strong crosswinds. Thus, under normal flight conditions, a significant portion of the tail simply adds drag and weight penalties without contributing useful control forces. Furthermore, the same tail design is often used within a single model family for manufacturing convenience, as demonstrated in Figure 1.1 for the Airbus A32X family, making it even more oversized for the versions with longer bodies and resulting in increased fuel consumption of the entire family.

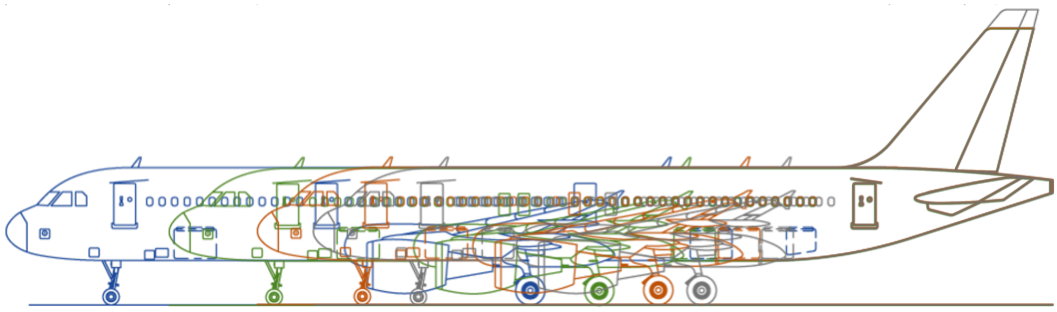

Figure 1.1: Airbus A32X family of aircraft share the same vertical tail design even though body length differs by over 40% (31.44 to 41.51 m), adapted from (Scavini, 2011).

A system integration study for the NASA Environmentally Responsible Act (ERA) project and a campaign series ranging from subscale wind tunnel testing to a full-scale flight test showed that fundamental design changes involving active flow control (AFC) technologies have the potential to achieve significant performance improvements. The flow control device used for these studies was the sweeping jet actuator

(SJA), a fluidic oscillator that operates on a supply of compressed air. The control efficacy of SJAs is well-established, but the difficulty of their characterization and lack of a comprehensive experimental database impedes their application to aircraft design. Part I of this thesis seeks to bridge some of these gaps by maturing fundamental understanding of how sweeping jets interact with flow separation phenomena and developing a framework for integrating that knowledge into system-level design.

1.1 Objectives

In Part I of this thesis, a swept wing of modular geometry equipped with an array of SJA at the flap shoulder is investigated through balance measurements and surface tuft visualizations. The objectives are to:

- analyze the effects of leading-edge vortices and trailing-edge separation on the aerodynamic performance of a swept wing,
- demonstrate the importance of an approach that integrates active flow control into system design, and
- optimize sweeping jet actuator configurations with respect to specific performance or control objectives.

The current Introduction chapter continues with an overview of SJA technology and details of the wind tunnel setup. Then, Chapter 2 presents a comprehensive analysis of the baseline flow and performance (i.e., without any flow control) of the swept wing model. Unifying trends in lift, drag, and pitching moment on the wing are related to its geometry and observed flow structures. In Chapter 3, AFC is added to the mix. We begin by challenging the long-standing practice of relying on momentum coefficient C_μ to characterize blowing AFC input, and advocate for an approach that also considers measures of fluidic power. This framework paves the way for an optimization process that seamlessly integrates the physics of flow control with the engineering of real aircraft. Chapter 4 dives deeper into the flow physics of the interactions between the LEV, TES, and SJAs. Details of optimizations under different objectives and constraints are presented and interpreted. Chapter 5 concludes Part I with outlooks on future research directions and design approaches.

1.2 Sweeping jet actuators and active flow control

Flow control is a catch-all term that can be used to describe any attempt at altering the flow over a body in a favorable way. There are many functional definitions in

the literature for different types of flow control based on mechanism, effect, and application. Here, we introduce a few key concepts and terminologies relevant to this thesis.

Passive flow control involves geometrical modifications, such as installing vortex generators on a wing or chevrons on the exhaust nozzle of an airplane. These devices do not require any auxiliary power input, and therefore are permanently "on" regardless of their need. In contrast, active flow control requires an external energy input which can be adjusted on-demand. Traditional airplane designs utilize a system of mechanical actuators that deflect control surfaces, resulting in geometrical modifications as the need arises. For example, flaps are deployed during takeoff and landing to provide extra lift at low speeds but stowed during cruise flight to avoid drag penalties. Fluidic active flow control involves the addition or removal of flow, referred to as blowing and suction, respectively. The control level may be characterized through mass, momentum, or energy flux. Fluidic actuators may be steady or oscillatory in nature, and some zero-net-mass-flux devices introduce pure oscillations into the flow field.

One advantage of oscillatory blowing is the ability to efficiently exploit instabilities in turbulent shear flows. The concept emerged from many decades of fundamental investigations of free mixing layers (Oster and Wygnanski, 1982; Gaster, Kit, and Wygnanski, 1985) and wall-bounded shear flows (Katz, Seifert, and Wygnanski, 1990; Elsberry et al., 2000), and provides the leverage necessary to alter the state of the flow to achieve large performance gains with small energy inputs. This contrasts with early boundary layer control (BLC) research with steady blowing, whose objective was to recover mean frictional losses in the boundary layer by energizing it, and thus performance improvements were roughly proportional to the energy expended.

The performance difference between these two approaches was demonstrated on a NACA 0015 airfoil with a deflected flap from which the flow separated at small incidence angles (Seifert et al., 1993). Different methods of blowing at the flap hinge increased maximum lift from 1.4 to 2.3 and eliminated the form drag between $0.9 < C_L < 1.5$, as shown in Figure 1.2. $C_\mu = 0.10$ was required using steady blowing (red triangles), while nearly identical $C_{L,max}$ and form drag polar were achieved by superposing momentum oscillations $\langle c_\mu \rangle = 0.016$ onto a much weaker jet $C_\mu = 0.008$ (blue squares). Both control approaches reattached the separated shear layer to the flap surface, but the advantage of the latter is clear: it required

less than 1/4 of the momentum by destabilizing the shear layer through periodic perturbations that are amplified by the mean flow.

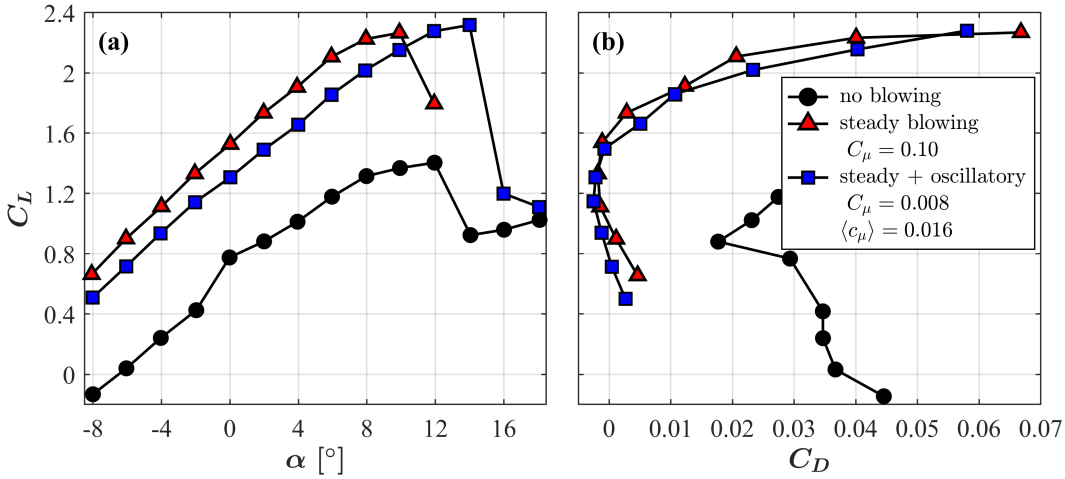

Figure 1.2: (a) Lift and (b) form drag measured on a NACA 0015 airfoil at $Re = 5 \times 10^5$ with flap deflection $\delta = 20°$, redrawn using data digitzed from (Seifert et al., 1993).

Thus, one emerging definition of AFC to distinguish it from classical BLC is that it seeks to generate performance changes of much larger order than the energy input by targeting flow instabilities. The dominant flow instability in 2D flows is Kelvin-Helmholtz (inviscid) which is often associated with the inflectional velocity profile preceding separation (Elsberry et al., 2000; M.D. Zhou, Heine, and Wygnanski, 1996). Wall jets on curved surfaces are also susceptible to viscous Tollmien-Schlicting (viscous) and centrifugal instabilities of the Gortler type (Han, M. de Zhou, and Wygnanski, 2006; Neuendorf, Lourenco, and Wygnanski, 2004). 3D flows over swept wings are susceptible to attachment line and crossflow instabilities, and the leading-edge vortex (LEV) in such flows undergoes a mix of absolute and convective instabilities that lead to vortex breakdown (Mitchell and Delery, 2001; Margalit et al., 2005).

The SJAs used on the thin swept wing model in this thesis are AFC devices that draw from a supply of compressed air to produce oscillatory blowing. Their origins lie in fluidic analogs of electronic amplifiers, developed at the Harry Diamond Labs in the 1950s. A schematic drawing of the selected SJA geometry is provided in Figure 1.3, although other geometries that operate on similar principles are also available (Ganesh et al., 2022). When a pressure difference is applied across the actuator, a jet from the inlet initially attaches to one of the two walls in the interaction region

due to the Coanda effect. Most of this jet exits through the nozzle, but part of it impinges on the far wall and feeds the corresponding feedback path. The fluid passing through the feedback path pushes the inlet jet away and toward the opposite wall. This process is repeated to create an oscillatory (sweeping) motion of the jet whose frequency depends on the pressure ratio and the length of the feedback path (Schmidt et al., 2016). A detailed analysis of the startup mechanism of a SJA via Schlieren visualization is presented in (D.G. Hirsch, 2017). The SJA thus produces a highly three-dimensional jet from a relatively simple two-dimensional geometry with no moving parts. These factors contribute greatly to its control authority, manufacturability, and reliability, rendering it an attractive option for application to real vehicles.

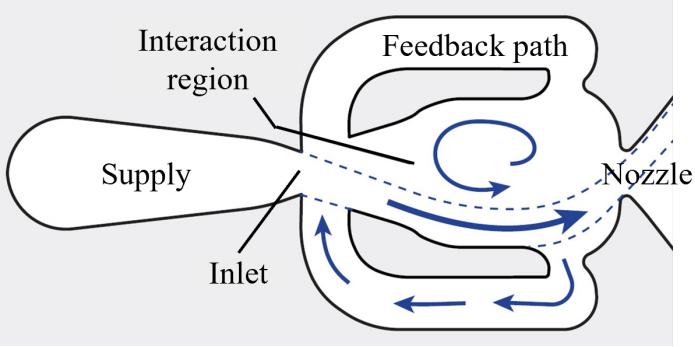

Figure 1.3: Schematic of the internal geometry of a sweeping jet actuator, adapted from (Cattafesta and Sheplak, 2011).

Most comprehensive application-focused experiments using these actuators were carried out on a swept back, tapered vertical stabilizer with a spanwise array of identical SJAs at the rudder hinge. Investigations ranging from subscale wind tunnel experiments to full-scale flight tests (Seele et al., 2013; Whalen, Lacy, et al., 2015; Whalen, Spoor, et al., 2016) contributed significantly to the maturity and understanding of the technology. At the same time, the experiments revealed the challenges to engineering design and complexity of 3D flow physics that need to be further explored.

1.3 Experimental setup

Experiments were performed on a semi-span non-tapered thin swept wing model in the 1.3 m × 1.8 m × 7.5 m test section of Caltech's Lucas Wind Tunnel (LWT), a closed-loop subsonic wind tunnel with maximum freestream speed of $u_\infty = 65$

m/s. The highly configurable "MOBLE"[1] model was designed and initially tested by Hirsch under a grant by the Northrop Grumman Corporation and the Air Force Research Laboratory (D.G. Hirsch, 2017). This previous study sought to understand the flow physics when AFC is applied at different chordwise locations, and explored different actuation methods (steady vs sweeping jets) on a specific wing geometry ($\Lambda = 30°$, $A_R = 2.6$, $\delta = 0°$ or $45°$). This thesis focuses on SJAs at the flap hinge ($x/c = 0.8$), which Hirsch found to be most effective at lift enhancement, and significantly expands the parameter space for wing geometry and spanwise actuation location.

The model is comprised of three identical elements at native sweep back $\Lambda = 30°$ and a root wedge to increase the sweep to 45°. Thus, it can be tested at three different aspect ratios for each of the two sweep angles: {1.3, 2.6, 3.8} at $\Lambda = 30°$ and {1.5, 2.3, 3.2} at $\Lambda = 45°$. CAD drawings for the high A_R configurations are shown in Figure 1.4. Each wing element has a flap located at 80% chord that can be deflected separately or in unison in 15° increments.

A spanwise array of twelve SJAs is installed at the flap shoulder of each element. Nozzles are spaced 38.1 mm (1.5 in) apart and have cross-sectional dimensions of 1.0 mm × 2.0 mm (0.04 in × 0.08 in). They have a fixed orientation perpendicular to the leading edge. A single flow controller at the system entrance regulates and records the total pressure p_t and flow rate $\dot{m}_j$, but a four-way valve divides the air to the common plenum of each wing section, as depicted in Figure 1.5. Individual actuators can be manually enabled or disabled to vary the active jet distribution by turning a sealing plug on the cover.

The chord-based Reynolds number range tested was $0.6 \sim 1.7 \times 10^6$. An aluminum fairing provides a smooth aerodynamic transition from the tunnel floor to the model root to minimize edge effects. Turbulator strips are installed 5 cm from the leading edge ($x/c = 0.08$) on both the pressure and suction sides to avoid boundary layer transitional effects. The model is mounted on a six-component strain gauge balance to measure aerodynamic forces and moments, which is in turn mounted on a rotary table to vary α.

Flow over the model is visualized through surface tufting. Tuft arrays are made in-house using UV-fluorescent thread, fluorescence-suppressing kapton tape, and an alignment board, as shown in Figure 1.6. Tufts consist of five threads that are

[1] Acronym for "Multi-Objective Blown Leading Edge". Name of the model is inherited from previous projects for consistency, but this thesis does not study leading-edge blowing.

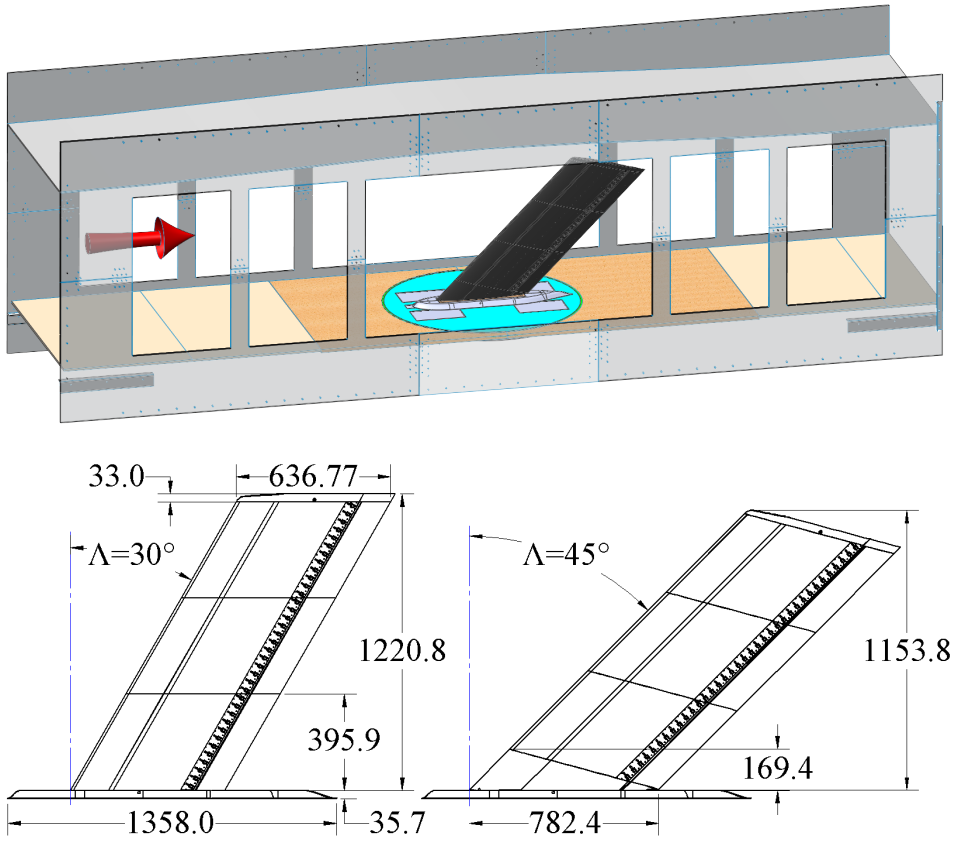

Figure 1.4: CAD drawings of the three-element configurations of the MOBLE model tested in the subsonic Lucas Wind Tunnel facility at Caltech (dimensions in mm).

3.81 cm long (1.27 cm covered by the tape) and are spaced 1.91 cm apart. They are then installed in eleven rows parallel to the leading edge on the suction side of the wing, as shown in Figure 1.7. The region corresponding to the SJA cover plate remains untufted to retain access to the actuator sealing plugs. The leading edge, wing tip, and root are also outlined with the same fluorescent thread so that the wing outline appears as a dashed line in the images.

Images are taken with a Sony RX10-IV camera under a UV light source. A low ISO, large F#, and exposure time of approximately 3 seconds is used. The high contrast between the tufts and background provided by the fluorescence facilitates the extraction and identification of relevant flow features during post-processing.

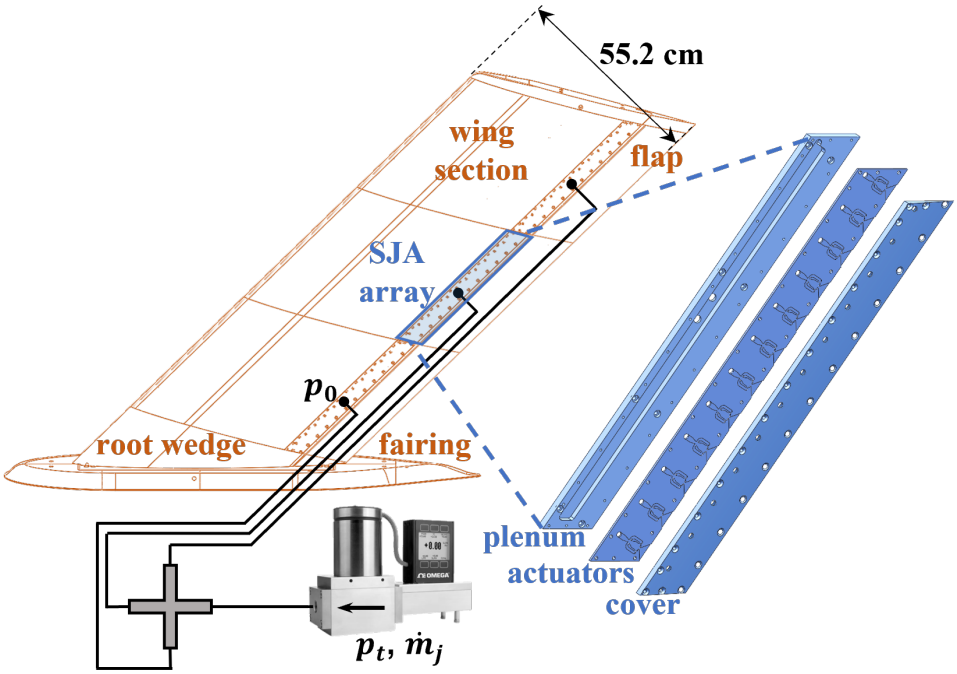

Figure 1.5: Schematic of the MOBLE wing assembly and its plumbing, with various components labeled.

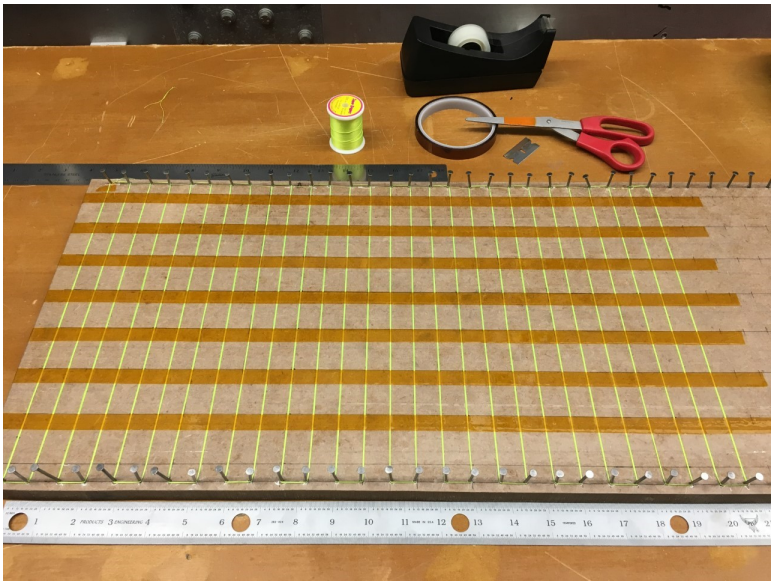

Figure 1.6: Tools required to make the fluorescent tufts.

1.4 Parameter definitions

The cross-section of the wing along the streaming direction is shown in Figure 1.8. The airfoil design is based on the LAVLET configuration, originally developed

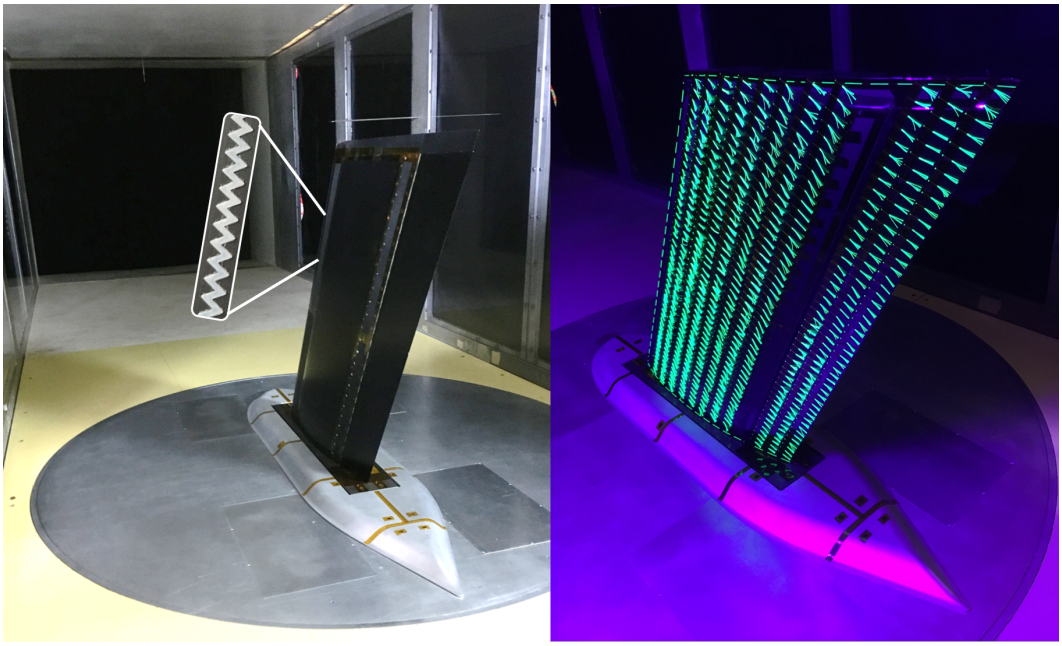

Figure 1.7: Images of the two-element MOBLE model installed in the LWT test section. A triangular turbulator strip is installed across the entire span at $x/c = 0.08$. Tufts made of UV-fluorescent thread visualize the surface flow over the suction side of the wing.

for high-lift laminar flow control applications (Bright et al., 2013). It has a slight camber and relatively small radius at the LE.

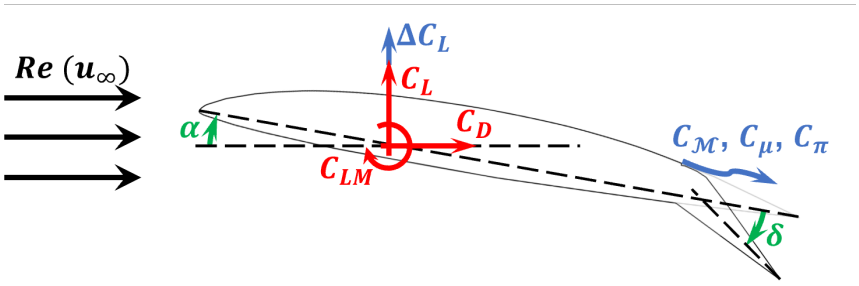

Figure 1.8: LAVLET airfoil cross-section geometry with conventions for lift, drag, and pitching moment coefficients.

Red arrows define conventions for lift, drag, and pitching moment coefficients, which are the primary dependent variables investigated. Lift force F_L and drag force F_D are measured parallel and perpendicular to the freestream direction, respectively, and pitching moment M_P is in the same direction as α ("nose up"). To obtain the dimensionless coefficients, they are normalized by the freestream dynamic pressure

and relevant length scales:

$$C_L = \frac{F_L}{\frac{1}{2}\rho_\infty u_\infty^2 S} \tag{1.1}$$

$$C_D = \frac{F_D}{\frac{1}{2}\rho_\infty u_\infty^2 S} \tag{1.2}$$

$$C_{LM} = \frac{M_P}{\frac{1}{2}\rho_\infty u_\infty^2 Sc} \tag{1.3}$$

When AFC is applied, the effected change Δ is reported for fixed geometry and fixed actuator configuration. The lift increment ΔC_L is shown in the diagram as an example.

Since the spanwise actuator distribution may be freely varied with the sealing plugs, three parameters are used to quantitatively characterize the distributions considered: coordinate ξ_0 of the first active actuator (measured vertically from the wing root), spacing ξ_s between active actuators, and total nozzle area A_j. For convenience, actuators are numbered 1 through 36 from root to tip, and intuitive descriptions are provided throughout the thesis. For example, "Jets 1-6" or "twelve actuators sparsely and uniformly distributed across the span" may be used. In a similar vein, the number of active actuators n_j may be used in lieu of A_j when appropriate. Note that the size, internal geometry, and installation orientation of the actuators remain fixed throughout this study.

The momentum coefficient C_μ is commonly used in the AFC literature to quantify the total momentum injected into the flow. Since momentum and force have the same dimensions, the coefficient takes on a similar form:

$$C_\mu = \frac{J}{\frac{1}{2}\rho_\infty u_\infty^2 S} \tag{1.4}$$

However, the jet momentum flux $J = \int (\rho_j u_j^2)\, dA_j$ is difficult to measure accurately in situ.

Point measurements of subsonic velocities at the nozzle may be obtained by hot wires or pitot probes in the laboratory (Seifert et al., 1993) and on a full-scale airplane (McVeigh et al., 2011), but such intrusive techniques may affect the sweeping behavior of the jet. Resolving the velocity profile of a jet emanating from a small (mm) nozzle and oscillating at high (kHz) frequency is challenging, and characterizing all jets in an array is time-consuming, so assumptions about spatial and temporal invariance must often be made.

Modeling the internal flow of a sweeping jet actuator enables prediction of nozzle conditions from upstream chamber conditions which are generally easier to measure. However, the complex geometry and flow physics involved poses a challenge to this approach. Different models have different errors in different flow regimes (Otto et al., 2022); for example, Hirsch established different relationships between momentum and mass flow injection in the subsonic and supersonic regimes, supported by Schlieren visualizations of the jet behavior (D.G. Hirsch, 2017). Furthermore, modeling assumptions that may hold in idealized lab conditions, such as stagnation in settling chamber and adiabaticity, can easily break down in applications due to design constraints or operational environments.

Injected momentum can also be inferred from the thrust generated in the absence of a free stream, analogous to the calibration of a jet engine. Such "jet tares" could be misleading, however, when the jets are embedded into a curved surface. The thrust recovery of a SJA array on a V-22 flap model depended significantly on the flap deflection angle and the actuator spacing tested (Lucas et al., 2008) due to the Coanda effect and interactions between adjacent actuators.

There are many studies on measuring or modeling C_μ accurately (Sayed et al., 2018; Semaan, 2020; Otto et al., 2022) but this is not an objective of this thesis. Unless otherwise specified, C_μ in this study is computed assuming incompressible flow ($\rho_j = \rho_\infty$) and uniform jet velocity profile, simplifying to a function of mass flow coefficient $C_\mathcal{M} = \dot{m}_j/(\rho_\infty u_\infty S)$ and nozzle area ratio $\mathcal{A} = A_j/S$ only:

$$C_\mu = 2\frac{C_\mathcal{M}^2}{\mathcal{A}} \tag{1.5}$$

While this may not be an accurate model for the actual jet momentum injected by an array of SJAs, it greatly simplifies the data acquisition process since mass flow rate is conserved throughout the AFC system. Under many cases, the parameter also serves as a fair platform for comparing different actuation configurations during the optimization process.

Although momentum is a key parameter when studying the fundamental dynamics (i.e., forces) of the flow, its use is limited when designing an AFC system for real vehicles where constraints are placed on flow rate and/or pressure. Thus, this thesis will also consider fluidic power coefficients C_π, which will be discussed in further detail in Chapter 3.

In summary, the independent dimensionless parameters investigated in this thesis

are:

$$(C_L, C_D, C_{LM}) = f\left(Re, \Lambda, A_R, \alpha, \delta, \frac{\xi_0}{b}, \frac{\xi_s}{b}, \mathcal{A}, C_{in}\right) \tag{1.6}$$

where C_{in} may refer to any mass, momentum, or power coefficient quantifying the total AFC input.

Chapter 2

CHARACTERIZATION OF BASELINE FLOW AND PERFORMANCE

Wind tunnel testing is a cornerstone of aircraft design and development. Although the field of computational fluid dynamics has grown rapidly over the past few decades, it will not completely replace experiments in the foreseeable future. Accurate modeling of turbulence and separation phenomena continue to challenge us, and fully resolved direct numerical simulations for high Re flight remain infeasibly expensive.

The first "flying machines" modeled after birds in the early-19th century were immediately taken to flight tests, which expectedly resulted in failure (NASA Glenn Research Center, 2021). To first understand the dynamics of flight in controlled environments, aerodynamicists tried mounting models inside caves with relatively steady wind or at the end of a rotating arm. Despite their limitations, these led to successful designs of gliders. Frank Wenham operated the first wind tunnel in 1871, and it wasn't until 30 years later that the Wright brothers successfully flew a controllable powered airplane.

The utility of a wind tunnel is obvious to modern aerodynamicists, and many unique facilities exist around the world to simulate various flight conditions: cascade tunnels (Niehuis and Bitter, 2021), full-scale tunnels (Dino and Dunbar, 2008), high-pressure hypersonic shock tubes (Hornung, 1992), and turbulence-inducing fan arrays (Dougherty, 2022), just to list a few. Such highly controlled testing environments have contributed significantly not only to the development of flying vehicles but also to our understanding of fundamental flow physics and scaling laws that drive future design.

In designing an AFC-integrated swept wing of finite aspect ratio for commercial and military applications, the first step is to understand the baseline flow without any control applied over a wide geometric design space. What forces and moments act on the wing? What flow structures or phenomena should be targeted for control, and when/where do they occur?

This chapter develops a unifying theme across the six wing planform configurations tested by relating the lift, drag, and pitching moment performance to interactions

between the leading-edge vortex (LEV) and trailing-edge separation (TES). Then, experimental effects of Re and surface tufting are carefully considered. These results pave the path for a comprehensive investigation of different AFC configurations.

2.1 Lift, drag, and LEV formation dynamics

The baseline lift and drag performance of the six (Λ, A_R) planform configurations of the MOBLE wing are shown in Figure 2.1, all with respect to α. The vertical axes between $\Lambda = 30°$ and $45°$ have been matched for ease of comparison, and data points corresponding to maximum lift $C_{L,max}$ and glide ratio C_L/C_D (also called L/D) are color-coded in blue and green, respectively.

Since the airfoil is slightly cambered, all wings produce positive lift at $\alpha = 0°$. At small positive values of α where the flow is expected to be fully attached, lift increases linearly and the drag quadratically. In this regime, the lift slope is higher for configurations that are closer to a 2D airfoil (i.e., high A_R and low Λ), giving them a higher glide ratio. Minimum drag for all wings occur between $-1° \leq \alpha \leq 0°$, but maximum glide ratio occurs between $3° \leq \alpha \leq 5°$. These are functions of the cross-sectional airfoil shape and seems to be independent of Λ or A_R.

Higher A_R wings achieve higher maximum glide ratio, which drives commercial aircraft designers to use long, slender wings. Ultimately, however, the wings closer to a 2D airfoil stall earlier, achieving a lower $C_{L,max}$ at lower α. At high angles of attack, lower A_R wings have slightly higher glide ratio. Lift curves for $\Lambda = 45°$ wings undergo a drastic change in slope between $\alpha = 10 \sim 15°$ that allow them to reach very high $C_{L,max}$, and all wings experience severe drag penalties beyond the quadratic regime. These effects are all related to the LEV and will be investigated in further detail.

Current aerodynamic practices often strive to achieve attached flow throughout the entire flight envelope, but many high-speed combat aircraft also rely on vortex lift because they have highly swept back thin wings to delay the drag rise associated with shock wave generation. LEVs, which characterize the highly 3D flows over such wings, have also been observed in various other natural and manmade flight across a wide range of Reynolds numbers Re. When harnessed successfully, the LEV has been shown to provide significant lift augmentation for autorotating plant seeds (Lentink et al., 2009), slow-flying bats (Mujires et al., 2008), horizontal-axis wind turbines (Roy, Das, and Biswas, 2022), and various delta wings (Gursul, Wang, and Vardaki, 2007). However, their sudden formation and breakdown can also create

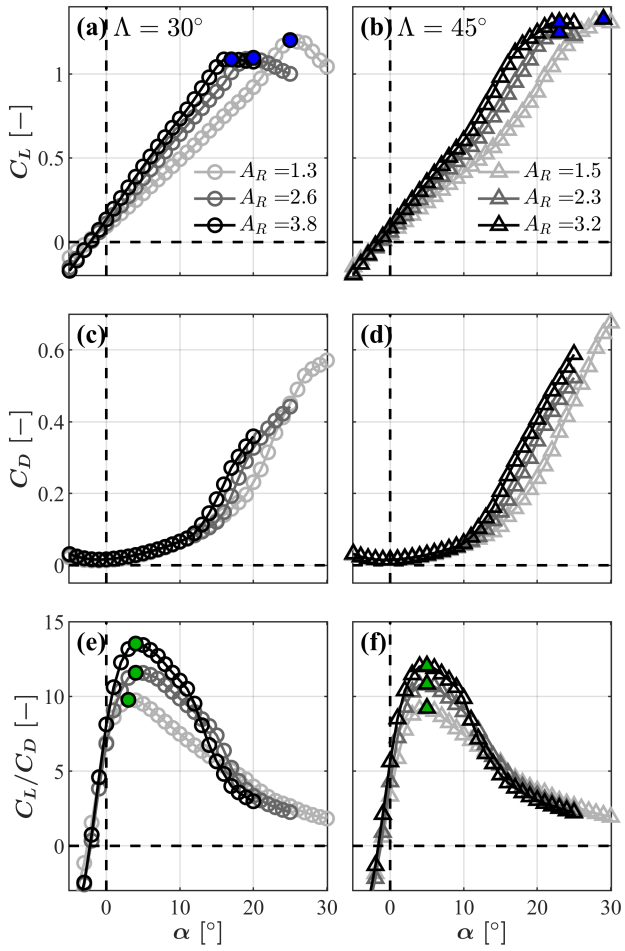

Figure 2.1: Lift and drag performance for the three A_R tested at (a,c,e) $\Lambda = 30°$ and (b,d,f) $\Lambda = 45°$. Markers are colored at maximum lift (blue) and glide ratio (green).

control and stability challenges.

Since the LEV takes various forms across many applications, a universal definition for the phenomenon does not exist. The geometry of the wing as well as the type of its motion (e.g., gliding, rotating, flapping) can significantly impact the separation and vortex dynamics. For the present study, the LEV is identified as unsteady flow separation that originates near the leading edge of the wing and whose presence results in increased lift.

The inception of the LEV on the MOBLE wing is observed through surface tuft visualizations. In Figure 2.2, tuft images taken immediately below and above the α of vortex inception on the $\Lambda = 30°$ wings are superposed in different colors. Tufts in red are well-aligned with the general streaming direction, indicating that the flow is fully attached and steady at the lower α. As α is increased by approximately 1°,

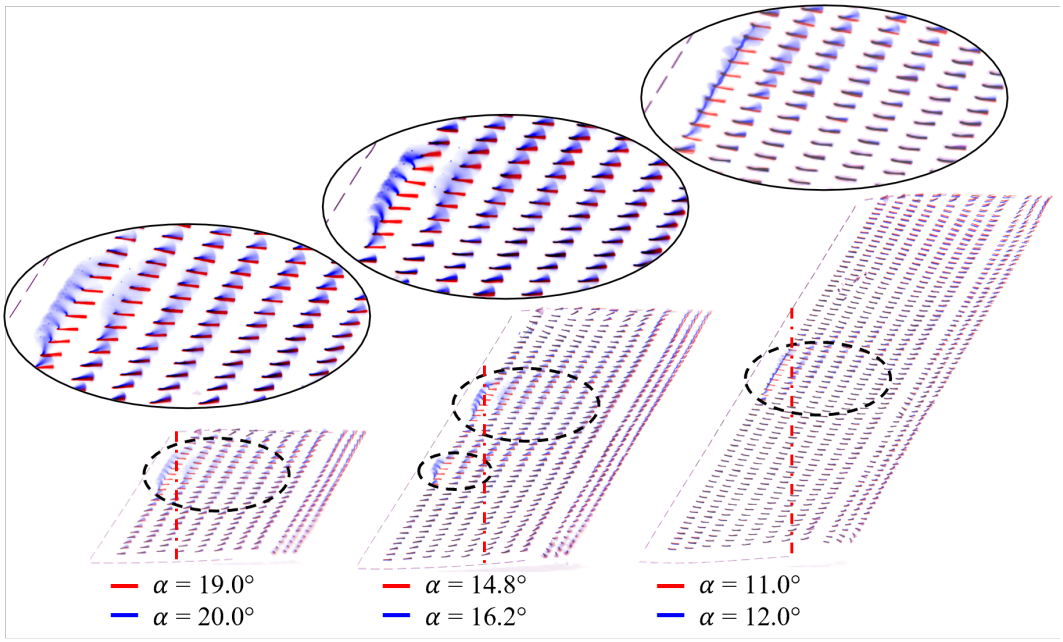

Figure 2.2: Superposition of tuft images taken at α immediately before (red) and after (blue) LEV inception for different A_R at $\Lambda = 30°$.

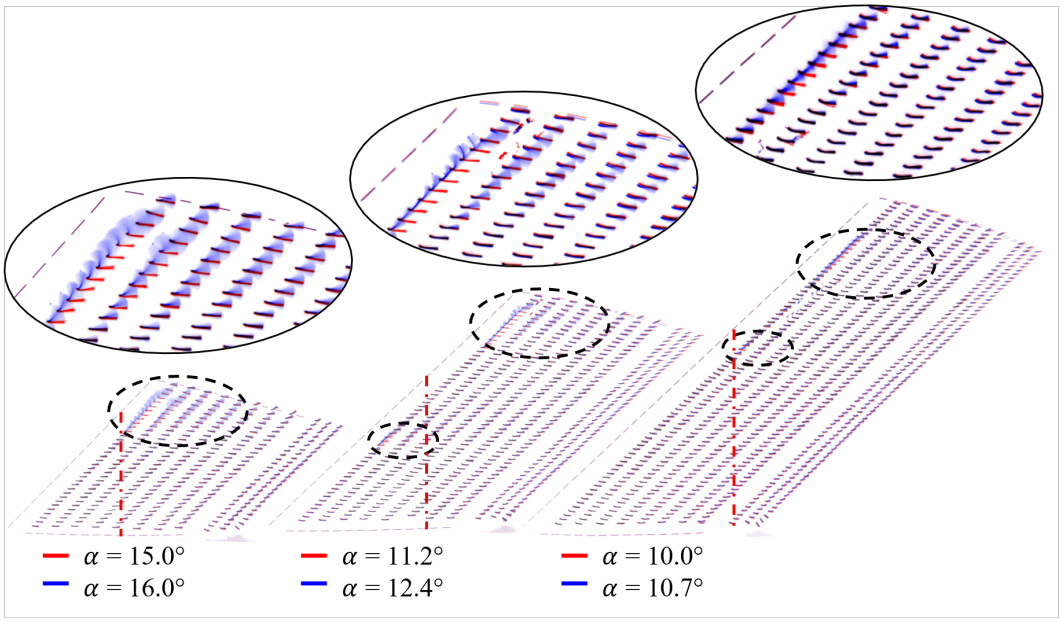

Figure 2.3: Superposition of tuft images taken at α immediately before (red) and after (blue) LEV inception for different A_R at $\Lambda = 45°$.

the vortex creates a small region of separated flow. This is depicted by the blue part of the image in zoomed view inside the dashed oval. Unsteadiness of the flow manifests as blurred wedge shapes that point up and away from the wing surface in

the long-exposure image. Note that in all these cases, the flow separation does not imply stall; the lift continues to increase beyond α_{LEV} as seen in Figure 2.1.

As the A_R of the wing is increased, few important changes occur in the formation dynamics of the LEV. First, the incidence angle of vortex inception α_{LEV} decreases. At $A_R = 1.3$, $\alpha_{LEV} \approx 20°$ while for $A_R = 3.8$, it occurs much earlier at 12°. The spanwise location of the vortex inception also seems to move inboard. The vortex forms near the tip of the short wing but around mid-span of the long wing. Interestingly, the location of vortex formation seems to coincide with the mean rotation point (MRP) of the wing indicated by a vertical dashed red line, which will be explained in the next section in conjunction with pitching moment. Finally, the strength of flow reversal seems to decrease with increasing A_R. At $A_R = 1.3$, the blue tufts in the first row are fully peeled off the surface, pointing mostly upstream and displaying highly unsteady behavior. At $A_R = 3.8$, the tufts are also peeled off the surface but to a lesser degree and no longer point upstream. While the phenomenon is difficult to quantify from these qualitative images, the amplitude of the tufts' fluttering clearly decreases.

The same technique is repeated for the $\Lambda = 45°$ wings and shown in Figure 2.3. The increase in Λ at a given A_R lowers the α_{LEV}. Decreasing α_{LEV} and flow reversal strength are again observed with respect to increasing A_R. However, the location of LEV formation does not seem to move inboard at this increased sweep back. It consistently occurs near the wing tip and sufficiently downstream of the mean rotation point.

While surface tufting provides a simple and meaningful flow diagnostic, it has drawbacks. The technique is intrusive and largely qualitative. Furthermore, spatial resolution is limited. Adjacent bundles must be spaced sufficiently far apart to avoid interference, and the first row of tufts is located downstream of the trip strip ($x/c = 0.08$), limiting access to the flow close to the LE.

Despite these shortcomings of tuft visualization, however, the observed trends correlate well with balance measurements. Formation of the vortex is accompanied by sudden changes in the integrated forces and moments on the wing. Vortex lift provides an additional contribution to lift, but the associated drop in LE suction pressure and momentum losses due to re-circulation also leads to a substantial increase in drag.

The lift and drag slopes of all six planform configurations are shown in Figure 2.4.

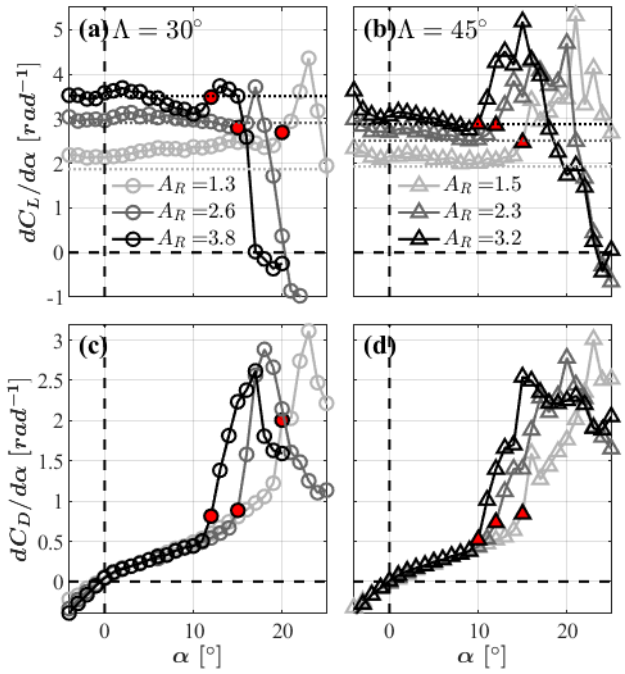

Figure 2.4: (a,b) Lift slope $dC_L/d\alpha$ and (c,d) drag slope $dC_D/d\alpha$ of all six wing configurations. Markers are colored at LEV inception (red).

The point corresponding to α_{LEV} measured by tuft visualizations is marked in red, and Kuchemann's model for lift slope of a low aspect ratio swept wing (Kuchemann, 1956):

$$\frac{dC_L}{d\alpha} = \frac{\eta_0 \cos\Lambda}{k + \sqrt{1 + k^2}} \tag{2.1}$$

where $\eta_0 = 2\pi\sqrt{1 - M_\infty^2}$ and $k = (\eta_0 \cos\Lambda)/(\pi A_R)$, is indicated by a dotted line for reference. For both Λ, the lift slope in the low α regime agree well with Equation 2.1 especially at the higher A_R tested and outperform the model's prediction at the lowest A_R. After LEV inception, the lift slope increases due to vortex lift. For $\Lambda = 30°$ in (a), this effect is observed to be strongest on the shortest A_R of 1.3, achieving the highest maximum lift slope of 4.36 despite starting with the lowest value at low α. This difference in vortex strength was also observed qualitatively in tuft images (Figure 2.2) and enables $A_R = 1.3$ to achieve the highest maximum lift as well (Figure 2.1).

Similar trends are observed for $\Lambda = 45°$ wings in (b). At this higher sweep, the effect of vortex lift relative to the conventional lift due to attached flow is much more pronounced, as noted by (Polhamus, 1966). Although both the lift slope and glide

ratio suffer at low α, the $\Lambda = 45^\circ$ wings ultimately achieve much higher $C_{L,max}$ than the $\Lambda = 30^\circ$ wings.

The drag slope $dC_D/d\alpha$ shown is proved to be the best indicator of LEV formation across all configurations tested. In every case plotted in (c) and (d), α_{LEV} (red marker) corresponds to the first point that deviates from the initial linear trend at low α that implies the well-known quadratic drag increase in the attached flow regime. The collapse of data across different A_R onto a single representative curve in this regime enhances the visibility of the "spike" in drag due to the LEV.

Analyzing the lift and drag performance of low aspect ratio swept wings in conjunction with surface tuft visualizations illuminated important trends regarding LEV inception and the interplay between conventional and vortex lift. In the following section, we expand the discussion to include pitching moment as well as the growth and propagation behavior of the LEV. Unifying themes that emerge are explored in the context of higher-level wing design considerations that provide the foundation for understanding and optimizing AFC configurations in the later chapters.

2.2 Pitch stability

Understanding and controlling the longitudinal stability of aircraft wings has been a research topic of interest for many decades. The swept wing concept was first proposed by Adolf Busemann in 1935 (Busemann, 1935), triggering extensive research during the 1950s when the aerodynamic complexity regarding longitudinal stability at subsonic speeds came to light. NACA investigated the pitching moment behavior of hundreds of wing shapes (Furlong and McHugh, 1957) to reveal that most swept back wings were difficult to control at $C_L > 0.4$ due to two principal flow separation features: leading-edge vortex (LEV) and trailing-edge separation (TES). Both modes of stall precipitate strong spanwise flow near the wing surface and result in highly non-linear pitching moment curves due to shifts of the aerodynamic center (AC). Such pitch departures severely limit the operational range of C_L and require extensive use of control surfaces, which jeopardize the maneuverability and survivability (stealth) of the aircraft.

Sweep back Λ and aspect ratio A_R were determined as the primary factors affecting pitch stability, and empirical correlations were established across various wing shapes including delta, lambda, and trapezoidal configurations as well as those with non-linear leading edges. Conceptual design data sheets ("ESDU 01005" 2001) suggest that $2.6 < A_R \tan(\Lambda_{1/4}) < 3.0$ represents a region of marginal stability

separating the stable and unstable platforms, where $\Lambda_{1/4}$ represents the average sweep angle at quarter-chord. The empirical stability curve is illustrated in Figure 2.5, marked with general design spaces for common transport and combat aircraft.

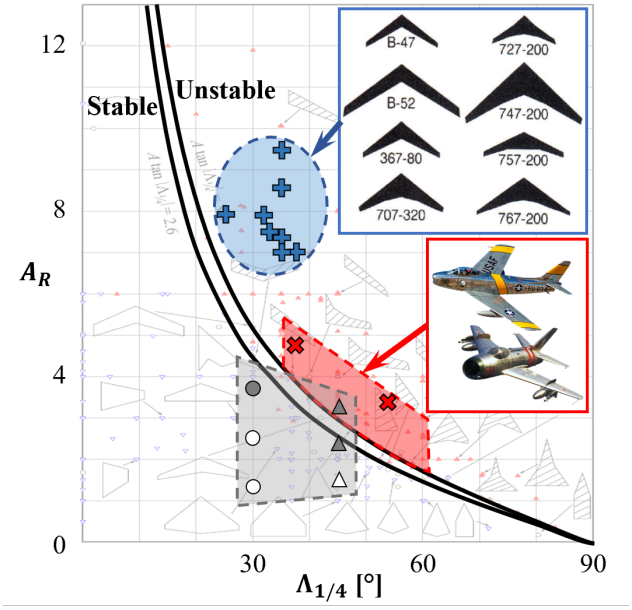

Figure 2.5: Empirically derived stability boundary of various wing planforms. Typical design areas of subsonic transport aircraft (blue) and combat jet aircraft (red) are shown, as well as the parameter space of the tested MOBLE configurations (gray).

Subsonic bombers and commercial airliners lie in the blue region, with eight examples from Boeing indicated by + symbols. These designs cluster around $\Lambda = 30°$ and employ high aspect ratio for efficient long-range flight, placing them in a highly unstable region of the diagram. The instability is partly alleviated through engine pylons, which effectively divide the wing into segments with smaller A_R and mitigate the spanwise flow component.

Combat aircraft designs lie in the red region, which is still unstable but much closer to the neutral stability curve. They employ wings at higher sweep and shorter aspect ratio to trade efficiency for agility, enabling flight at transonic and supersonic speeds. The *North American F-86 Sabre* and the *Russian MiG-19* are indicated by x symbols. Various passive flow control mechanisms have been implemented to improve pitch stability, such as strakes, fences, vortilons, canards, and snags.

Let us now revisit the MOBLE wing, whose six tested configurations are shown in gray in Figure 2.5, with circle symbols for $\Lambda = 30°$ and triangle symbols for $\Lambda = 45°$

following the conventions of previous figures. The shaded markers correspond to unstable configurations, and the unshaded markers correspond to stable configurations; the trend roughly conforms to the stability curve and their derivation will follow next. The tested parameter space traverses the marginal stability region and is representative of simplified transport and combat aircraft wing configurations, enabling investigation of and insight into a rich set of flow physics and applications.

The drag and pitching moment polars of all configurations are shown in Figure 2.6. The point of maximum lift to drag ratio, LEV inception, and maximum lift are marked in green, red, and blue, respectively. A horizontal red band indicates the region of $C_{L,max}/1.21$, representing the operational velocity limit as determined by FAA regulations, which requires a 10% stall speed safety margin at takeoff.

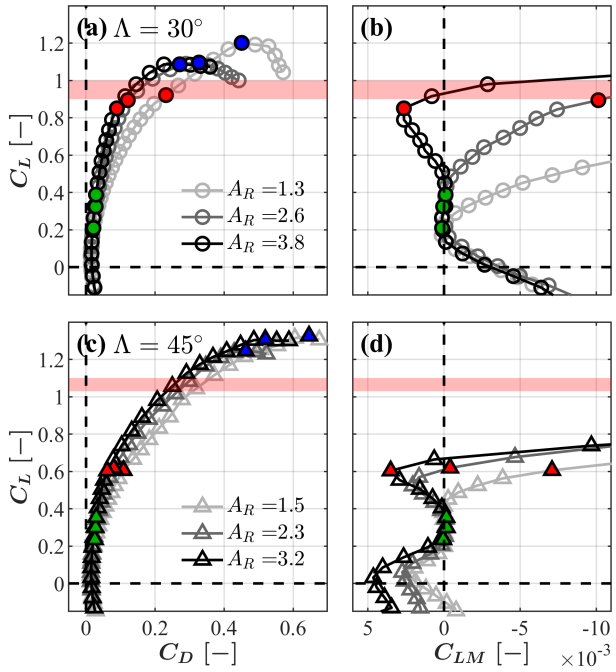

Figure 2.6: (a,c) Drag and (b,d) pitching moment polars for all wing configurations.

Airplanes typically cruise within the "drag bucket" where high lift-to-drag ratio (green) enables efficient flight. For the configurations tested, this occurs between $0.2 \leq C_L \leq 0.4$. To compute pitching moment, the mean rotation point (MRP) was selected to coincide with the AC in this cruising range and then a trim offset was applied to obtain $C_{LM} = 0$. The AC coincides with the quarter-chord on thin 2D airfoils in the absence of flow separation but shifts with α on swept wings due to 3D flow effects. Thus, the pitching moment can only be constant over a limited range of C_L in practice. Values of the streamwise MRP location and trim optimized for each

Λ	A_R	x_{MRP}/c	$C_{LM,0}$
30°	1.3	0.418	-0.0459
	2.6	0.583	-0.0483
	3.8	0.754	-0.0548
45°	1.5	0.493	-0.0297
	2.3	0.691	-0.0347
	3.2	0.895	-0.0382

Table 2.1: Location of MRP and trim offset applied to compute the C_{LM} values. Note that x is measured along the wing root from the LE.

configuration are provided in Table 2.1 and illustrated on the tuft images in Figures 2.2 & 2.3. As A_R is increased, the MRP moves downstream and the required offset increases in magnitude.

As C_L is further increased, the LEV forms (red). Although we saw that α_{LEV} depends on both Λ and A_R, Figure 2.6 illustrates that the vortex inception occurs at constant C_L for given Λ and is independent of A_R. The value occurs around $C_L = 0.9$ for $\Lambda = 30°$ and $C_L = 0.6$ for $\Lambda = 45°$. Thus, Λ seems to govern some sort of limit to the amount of circulation that can be contained on a wing with fully attached flow.

In summary, the cruising α of a wing and the C_L at which the LEV forms do not depend on aspect ratio. This has important implications for general wing design when taken together with the FAA regulatory velocity limit. At $\Lambda = 30°$, LEV begins to from near this limit resulting in fully attached flow throughout the wing's operational range. This renders the LEV to be irrelevant to longitudinal stability design considerations and disqualifies it as a target for active flow control. However, as Λ is increased to 45°, the operational threshold is increased due to the higher $C_{L,max}$ obtained by vortex lift while the LEV is initiated at much lower C_L. The wing now operates across two regimes, one characterized by fully attached flow and the other in the presence of a strong LEV. This presents interesting challenges and opportunities for integrating flow control into the design of the wing.

The pitching moment polars in Figure 2.6 (b) & (d) establish the stability characteristics of each wing. Note that the direction of the C_{LM} axis is reversed to conform to convention. An instability, by definition, amplifies small perturbations to an equilibrium state. Thus, the pitch departure of a statically unstable wing induces a nose-up moment as α is increased (positive C_{LM} under the convention given in Figure 1.8), causing the aircraft to flip over on its back. In contrast, a stable con-

figuration induces a negative restoring moment that tends to reduce α back to the trimmed equilibrium state.

Three of the six configurations—$\{\Lambda = 30°, A_R = 3.8\}$, $\{\Lambda = 45°, A_R = 2.3\}$, and $\{\Lambda = 45°, A_R = 3.2\}$—exhibit an unstable pitch departure at $C_L > 0.4$, and have been shaded in dark gray in Figure 2.5. Although these points do not precisely adhere to the empirically established neutral stability curves, they follow the trends with respect to Λ and A_R. In all three unstable configurations, the LEV does not contribute to pitch-up departure which occurs around $C_L = 0.4$. In fact, the LEV upon its inception contributes to a strong negative pitching moment. For the two configurations with $A_R > 3$, the LEV forms at the peak of the unstable pitch departure and restores stability at larger α. This is because the vortex creates a region of low pressure behind the MRP, as was shown in tuft visualizations and induces a negative pitching moment.

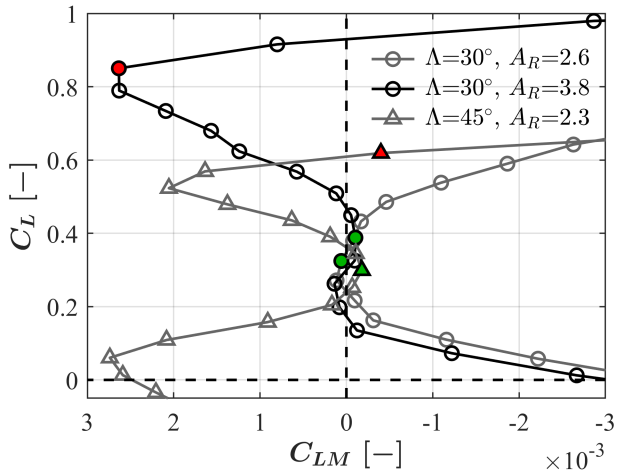

Figure 2.7: Comparisons of the pitching moment curve as the longitudinally stable $\Lambda = 30°$, $A_R = 2.6$ wing is made unstable through an increase in Λ and A_R.

Since the LEV did not contribute to pitch departure in any of the configurations tested, flow behavior at the trailing edge was scrutinized in search of an explanation. Consider the stable $\Lambda = 30°$, $A_R = 2.6$ wing that becomes unstable as either Λ is increased to 45° at approximately constant A_R, or A_R is increased to 3.8 at constant Λ. The C_L vs C_{LM} curves showing these destabilization processes are replotted in Figure 2.7 on an expanded scale. Tuft visualizations obtained at different points along the pitch curves shed light on the separation process. The values of α, C_L, and C_{LM} corresponding to the observations presented in Figures 2.8 & 2.9 are tabulated in Table 2.2.

	Figure 2.8			Figure 2.9		
	α [°]	C_L [-]	C_{LM} [-]	α [°]	C_L [-]	C_{LM} [-]
(a)	4	0.32	$+5.9\times10^{-5}$	11	0.69	-3.9×10^{-3}
(b)	5	0.30	-1.8×10^{-4}	9	0.68	$+1.6\times10^{-3}$
(c)	7	0.49	-4.6×10^{-4}	15	0.89	-1.0×10^{-2}
(d)	9	0.48	$+1.4\times10^{-3}$	13	0.92	$+8.0\times10^{-4}$
(e)	11	0.69	-3.9×10^{-3}			
(f)	13	0.68	-4.7×10^{-3}			

Table 2.2: Values of α, C_L, and C_{LM} for tuft visualizations presented in Figures 2.8 & 2.9. The C_L is approximately matched in each image pair.

Tuft visualizations of the two-element wings (A_R decreases slightly from 2.6 to 2.3 with increase in Λ) are compared at selected lift coefficients of $C_L = 0.3$, 0.5, and 0.7 in Figure 2.8. The MRPs are indicated by dashed red lines and vertically aligned for each pair of images.

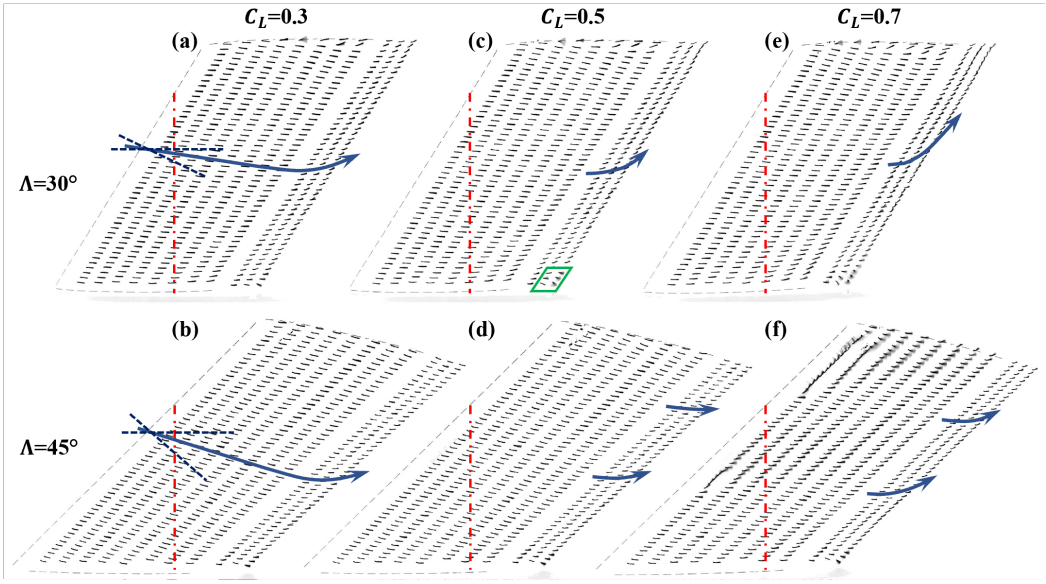

Figure 2.8: Progression of the surface flow field as C_L is increased on the two-element wings. (a,b) $C_L = 0.3$, (c,d) $C_L = 0.5$, and (e,f) $C_L = 0.7$. Dashed red lines indicate the MRP.

Both wings provide the maximum L/D at $C_L = 0.3$, which lies in the naturally trimmed range for cruise flight. The flow is fully attached in Figure 2.8(a) & (b), traveling relatively straight down the main body of the wing at an angle approximately halfway between the free stream direction and the normal to the LE, indicated by dashed black lines. This may be due to the averaging nature of tufts in

the wall-normal direction. At about $x/c = 0.7$, the flow bends slightly outboard as it approaches the TE to avoid the strong adverse pressure gradient existing along the direction normal to the LE. The streamline around mid-span represented by a blue arrow shows this change in flow direction.

At $C_L = 0.5$, the $\Lambda = 30°$ wing in Figure 2.8(c) experiences a stable pitch departure while the $\Lambda = 45°$ wing in (d) experiences an unstable departure. The difference in this pitch behavior can be mainly attributed to the flow over the TE. For $\Lambda = 30°$, flow begins to separate at the root of the wing (green box), and the spanwise outboard component of the flow becomes dominant elsewhere. Such a flow separation at the TE results in a pressure drop behind the MRP, inducing an overall nose-down pitching moment. In contrast, the outboard flow is mitigated for $\Lambda = 45°$ because the longer chord projection along the free stream direction alleviates the adverse pressure gradient. This suggests a larger pressure recovery that pushes the TE down and induces an unstable nose-up pitching moment.

By $C_L = 0.7$, a strong negative pitching moment acts on both wings but for different mechanisms. On $\Lambda = 30°$ in Figure 2.8(e), it is due to dominance of the spanwise velocity in the TES that is now almost parallel to the TE. The unsteady corner flow at the root has also grown, and some flow reversal near the tip is observed due to interactions with the tip vortex. On the other hand, the stabilization on the $\Lambda = 45°$ in (f) comes from the LEV which mostly lies behind the MRP. Note that the magnitude of the pitch gradient dC_{LM}/dC_L changes drastically after LEV inception (red marker) in Figure 2.7. We also observe some outboard flow component at the TE but not as dominant as that on the $\Lambda = 30°$ wing.

Relating balance measurements to surface flow visualizations illuminated a complex interaction between the flow separation process at the TE and the vortex formation process at the LE. Both contribute to highly nonlinear pitching moment behavior beyond the cruising range characterized by fully attached flow. The analysis revealed that a strong pressure recovery at the TE is primarily responsible for the unstable pitch departure as Λ is increased across the stability line at (approximately) constant A_R.

We now proceed to investigate the transition from stable to unstable pitch behavior as A_R is increased from 2.6 to 3.8 at constant $\Lambda = 30°$. Tuft visualizations at $C_L = 0.7$ and 0.9 are compared in Figure 2.9. Important flow features are again emphasized using colored shapes and arrows.

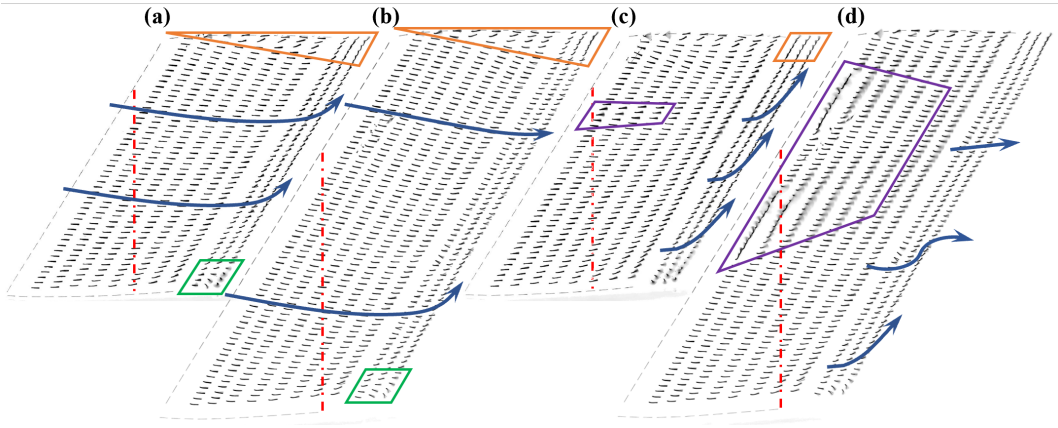

Figure 2.9: Comparison of the surface flow field at $\Lambda = 30°$ on the stable $A_R = 2.6$ wing and unstable $A_R = 3.8$ wing. (a,b) $C_L = 0.7$, (c,d) $C_L = 0.9$.

At $C_L = 0.7$, the shorter wing in Figure 2.9(a) experiences a stabilizing (negative) pitching moment while the longer wing in (b) experiences an unstable pitching moment. However, their surface flow fields exhibit many similar features. Sizes of the wingtip vortex footprint outlined in orange are comparable, which makes sense since the wings are producing the same C_L. The size of the separated corner flow at the TE juncture marked in green is also similar across the two. In the inboard half of the span, flow leaving the TE is characterized by a strong outboard velocity component.

The main difference between the flow patterns that may explain the contrasting directions of C_{LM} is the TES on the outboard half of the span. For the shorter wing, the outboard flow component still dominates. The last row of tufts in Figure 2.9(a) point uniformly upward and nearly tangential to the TE expect inside the separated root corner flow region. However, the last row of tufts in (b) point more normal to the TE starting around 1/2 span, indicating a stronger pressure recovery that pushes the TE down.

At $C_L = 0.9$, the distinction between the TES behaviors across the two wings is more pronounced. The shorter wing in Figure 2.9(c) continues to have strong outboard flow at the TE across its entire span. Flow at the tip even indicates signs of flow reversal due to interactions with the tip vortex. In contrast, on the TE of the longer wing (d), the outboard velocity component becomes stronger on the inboard half of the span while the tufts remain relatively parallel to the free stream direction in the outboard half. The intersection of these two regions, where spanwise flow meets

chordwise flow, is indicated by an S-shaped arrow. We observe the splitting of tufts in this region, suggesting a low-momentum vortex peel-off phenomenon.

The LEV begins to form on both wings at $C_L = 0.9$, as outlined in purple. Balance measurements indicate that the vortex contributes a nose-down pitching moment, as it creates a low-pressure region mostly behind the MRP. The relative contributions of the LEV and TES can be inferred from the value of C_{LM}. On the shorter wing, the size of the LEV is small yet C_{LM} is already highly negative, implying that the moment contribution from the outboard TE flow is much larger. On the longer wing, C_{LM} is still slightly positive, suggesting a tentative balance between the nose-up moment due to partial pressure recovery at the outboard TE and nose-down moment due to LEV suction. However, the subsequent rapid decrease in C_{LM} over $0.9 < C_L < 1.0$ indicates that the LEV dominates at higher α as it grows in strength.

The interesting flow features illuminated by surface tufting warrant further investigation with advanced diagnostics tools. Future work to quantitatively resolve the current observations may include pressure-sensitive paint to show the directions of favorable and adverse pressure gradient, or particle image velocimetry to compare the relative strength of chordwise and spanwise flow.

We have now come full circle in analyzing the effect of LEV and TES on longitudinal stability behavior of a simple swept wing at various Λ and A_R. We first demonstrated that although the LEV induced strong nose-down pitching moments on the wing, its formation occurred at much higher C_L than the cruising range and therefore was not responsible for pitch departure. Thus, we turned to separation behavior at the TE to explain the difference between stable and unstable pitch departure mechanisms. Surface tuft visualizations revealed that flow at the TE pointed tangentially outboard for stable configurations and more along the streaming direction for unstable configurations. At higher C_L on the unstable wings, an interplay between the positive C_{LM} contributions from pressure recovery at the TE and negative C_{LM} contributions from the LEV was observed.

Tracking the pitching moment to higher α can further illuminate the nature of this interaction. In Figure 2.10, C_{LM} vs α curves are grouped into (a) stable and (b) unstable configurations. Note that the data extends beyond stall indicated by a blue marker for most configurations. Looking at the C_{LM} "residue" in this high α regime may not be practically relevant from an engineering design perspective but is physically insightful.

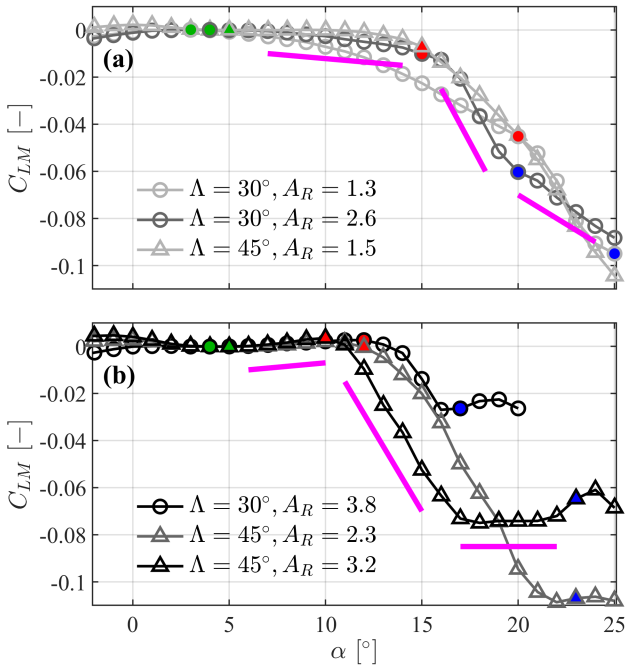

Figure 2.10: Pitching moment curves for (a) all stable configurations and (b) all unstable configurations extended to the high α range. Pink lines indicate the overall trend of $dC_{LM}/d\alpha$.

After LEV formation, C_{LM} of the stable configurations in (a) continues to decrease monotonically all the way beyond stall. That is, $dC_{LM}/d\alpha < 0$ for all α above the cruising range. The steepness of the slope depends on the strength and location of the LEV. On the other hand, C_{LM} curves of unstable configurations have a "tail" that plateaus and then briefly rises back up. In this case, $dC_{LM}/d\alpha < 0$ for a while after LEV formation but $dC_{LM}/d\alpha > 0$ as the wing approaches $C_{L,max}$. This data suggests that TES is the dominant mechanism contributing to pitching moment on stable wings, while unstable wings are characterized by a more intricate balance between TES and LEV that hinges on the growth and propagation dynamics of the LEV.

The stable $\{\Lambda = 30°, A_R = 2.6\}$ and unstable $\{\Lambda = 45°, A_R = 3.2\}$ wings are investigated further. The overall slope progression of their pitching moment curves is outlined in pink in Figure 2.10, and tuft image sequences showing LEV development are presented in Figure 2.11.

In Figure 2.11(a), flow over the stable wing is visualized from immediately after LEV inception at $\alpha = 16°$ to immediately before $C_{L,max}$ is achieved at $\alpha = 19°$. At $\alpha = 16°$, we observe the formation of three small vortex bubbles centered around

the MRP. As noted earlier in Figure 2.8, flow separation at the TE is dominated by a spanwise outboard component and even some flow reversal at the tip that leads to a strong negative pitching moment. As α is increased to 17°, the two outboard vortices grow and combine into a single vortex. The inner secondary vortex also grows, and the region of separated vortical flow extends slightly inboard. Most of the vortical structure lies behind the MRP so the resulting suction pressure contributes a negative pitching moment, working in the same direction as the TES. Thus, the slope $dC_{LM}/d\alpha$ is steepest (most negative) in this regime, $17° < \alpha < 19°$. The vortex continues to grow and propagate inboard, combining into a single structure at $\alpha = 19°$ that covers most of the wing surface including a significant portion upstream of the MRP. Maximum C_L is achieved once the vortex reaches the LE root and cannot propagate further inboard, causing the wing to stall. The slope remains negative and becomes less steep due to the suction contribution upstream of the MRP.

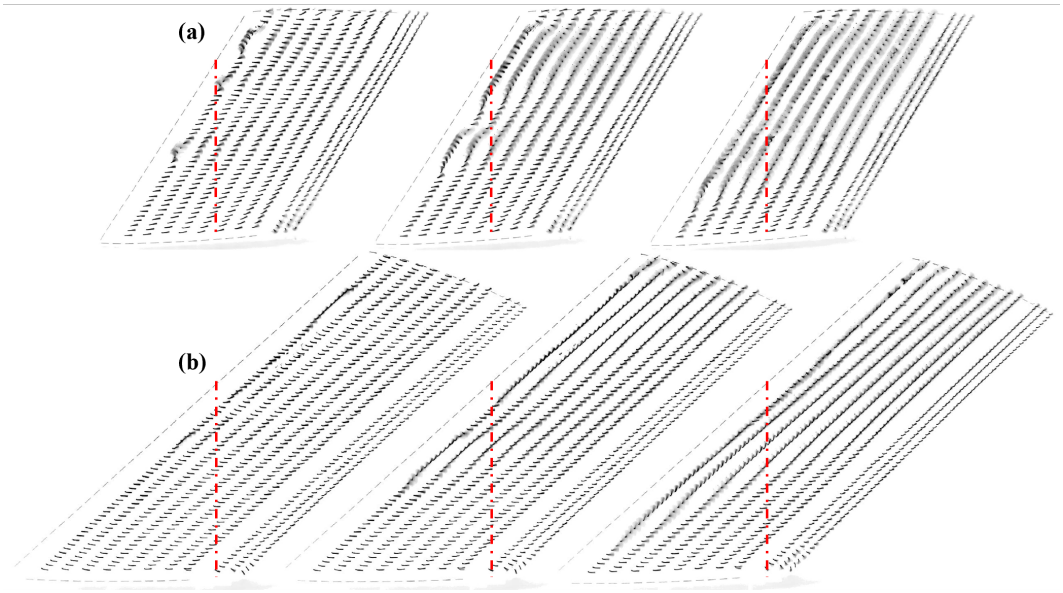

Figure 2.11: Tuft visualizations of LEV propagation at high α. (a) Stable $\{\Lambda = 30°, A_R = 2.6\}$ wing at $\alpha = 16°, 17°, 19°$. (b) Unstable $\{\Lambda = 45°, A_R = 3.2\}$ wing at $\alpha = 11°, 13°, 17°$.

A similar development of the LEV is observed on the unstable wing in Figure 2.11(b). A few small vortices form separately along the LE at $\alpha = 11°$, then grow and combine into a large structure at $\alpha = 13°$. As α is further increased toward stall, the vortex propagates inboard toward the root of the LE.

However, there are also key differences between the two visualizations that provide

insight on the C_{LM} behavior. At $\alpha = 11°$, the outboard velocity component at the TE seems weak, indicating still some pressure recovery that was responsible for the unstable pitch departure. Thus, although there may be some negative pitching moment induced by TES, we infer that the main contribution comes from the LEV, which now lies further behind the MRP compared to (a) for an increased moment arm. The vortex grows rapidly while remaining mostly behind the MRP, leading to a steep linear decrease in C_{LM} over $11° < \alpha < 17°$. Something interesting happens at $\alpha = 17°$, as the C_{LM} curve plateaus at -0.074 and remains relatively constant up to $\alpha = 22°$. This implies a balance between the growth of the LEV upstream of the MRP and the strengthening of spanwise flow at the TE, as they induce pitching moment contributions in opposite directions. Keep in mind, however, that the actual value of C_{LM} is still highly negative so the net effect is still a nose-down pitching moment. At maximum C_L, which is delayed all the way up to $\alpha = 23°$ (not shown in visualizations) due to the increased sweep, the slight increase in C_{LM} suggests that the LEV eventually won out the balance.

This plateau-bump behavior at the tail of the C_{LM} curve distinguishes unstable from stable longitudinal behavior across all six tested configurations. Integrated analysis of balance measurements with tuft visualizations showed that TES is the dominant mechanism on stable wings while the effect of the LEV is stronger on unstable wings.

2.3 Effect of flap deflection

Flaps are high-lift devices installed at the TE of an aircraft wing. When deflected, the increase in wing camber results in increased lift and drag. This reduces the stalling speed and enables flight at lower speeds, required especially during takeoff and landing. So far, we have investigated the interplay between separation phenomena at the LE and TE on a slightly cambered airfoil with no flap deflection (i.e., $\delta = 0°$). We now proceed to explore δ as an independent variable.

Figure 2.12 compares tuft visualizations on the $\Lambda = 45°$, $A_R = 3.2$ wing at $\delta = 0°$, 15°, and 30°. All images were taken with the same relative positioning of the camera to the wing, i.e., the camera was not rotated to accommodate the deflection of the flap. Tufts upstream of the last three rows are only shown once for $\delta = 0°$ since they are approximately the same across all cases.

With no flap deflection, the flow separates smoothly off the TE in a direction approximately parallel to the free stream across most of the span. Near the root and

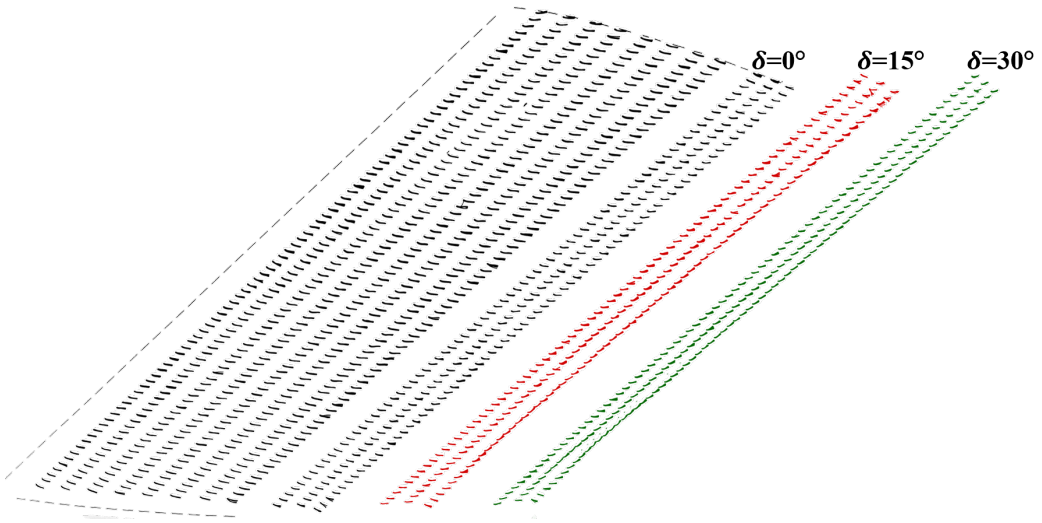

Figure 2.12: Tuft visualizations on the $\Lambda = 45°$, $A_R = 3.2$ wing when the flap is deflected to $\delta = 15°$ and $30°$.

tip of the wing, the flow direction is angled slightly downward, more perpendicular to the TE. The flow is fully attached over the entire wing. As δ is increased to 15°, the flow is largely unaffected near the wing root and in the third to last row of tufts, but gains a significant outboard component in the last two rows. In the last row, the flow points nearly parallel to the TE starting with the ninth tuft from the root. When δ is further increased to 30°, the region of strong outboard flow expands to include part of the third to last row as well as near the wing tip. It is interesting to note that unlike the LEV, the separated flow remains steady, since the tufts appear as clear lines rather than blurred wedges.

Increasing airfoil camber through δ therefore seems to increase the strength of TES. Let's quantify this observation by comparing force measurements on the ($\Lambda = 30°$, $A_R = 3.8$) and ($\Lambda = 45°$, $A_R = 3.2$) wings. The lift and drag coefficients are plotted in Figure 2.13 using open markers. Their slopes with respect to α are also plotted with dot markers. For each wing, the same reference area S is used in the coefficient calculations for all deflection angles.

At all α on both wings, an increase in δ resulted in an increase in both C_L and C_D, although to different extents. For a given δ, lift and drag increment are higher for the $\Lambda = 30°$ wing. A flap deflection of 45° increased $C_{L,max}$ from 1.09 to 1.59, as opposed to 1.30 to 1.55 on the $\Lambda = 45°$ wing.

It is also interesting to observe the effect of δ on the α at which important separation phenomena occur. As flap deflection is increased on both wings, the LEV forms

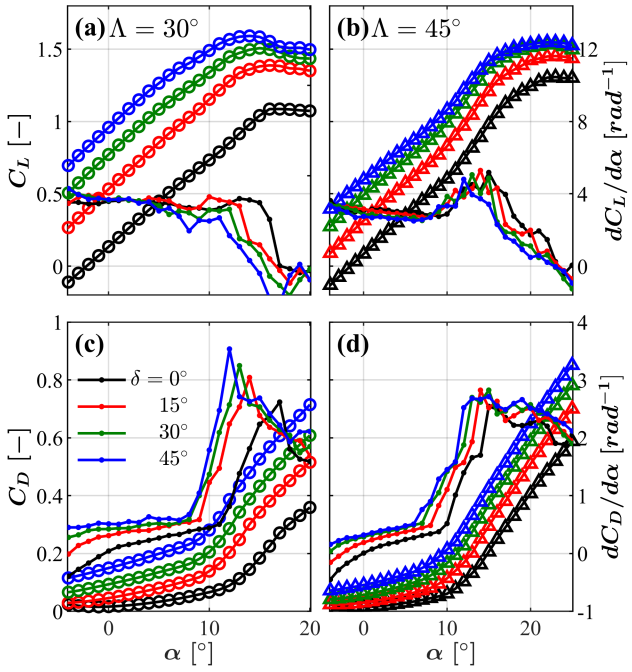

Figure 2.13: (a,b) Lift and (c,d) drag performance on the three-element wings at different flap deflections. $C_{L,D}$ are plotted with open markers and $dC_{L,D}/d\alpha$ are plotted with dots.

at earlier α on both wings as indicated by the spike in drag slope $dC_D/d\alpha$. The occurrence of stall also occurs earlier on the $\Lambda = 30°$. However, it is less affected on the $\Lambda = 45°$ and remains within $22° < \alpha < 23°$ across all flap deflections tested.

The lift slope curves are perhaps the most illuminating in terms of the interplay between the LEV and TES. On the $\Lambda = 30°$ wing, flap deflection does not seem to affect the lift slope in the linear (low α) regime, as is typical for non-extending flaps. When the LEV forms, a clear vortex lift effect is observed through an increase in $dC_L/d\alpha$ at $\alpha = 12°$ for $\delta = 0°$ and similarly at $\alpha = 10°$ for $\delta = 15°$. However, the LEV does not seem to provide additional lift at higher flap deflections. This implies that the effect of the increased camber at the TE dominates.

Entirely different trends are observed for lift slope on the $\Lambda = 45°$ wing. In the linear regime, lift slope decreases slightly with δ. Vortex lift is significant at all flap angles, and the maximum $dC_L/d\alpha$ achieved remains relatively constant. Here, the effect of the LEV dominates.

The relative importance of TES and the LEV was a recurring theme throughout the analysis of baseline flows presented in this chapter. Upon systematic examination of

a wide geometric parameter space of Λ, A_R, and δ, complex interplays between these variables were shown to determine the over lift, drag, and stability characteristics of the wing as well as the α at which different phenomena occurred. However, unifying trends emerged to suggest that Λ was primarily responsible for the strength of the LEV while A_R and δ governed TES.

This lays the foundation for understanding AFC efficacy on swept wings and optimizing their distribution along the span in Chapter 4, but a few more important considerations must be addressed first. In Chapter 3, we revisit what it means to truly "optimize" AFC as an integrated system rather than an add-on feature. For now, we conclude this Chapter with a brief discussion of two key experimental factors that have hitherto been neglected—Reynolds number (i.e., freestream velocity) and the presence of tufts—and validate this decision.

2.4 Validation of *Re* and tufting effects

Results of subsonic wind tunnel experiments are influenced by a variety of factors, from measurement uncertainty to physical constraints such as force balance capacities and model blockage effects. These effects need to be carefully considered as the model geometry or free stream conditions change throughout the campaign. The purpose of this section is to establish quantitative confidence in the major conclusions presented in Part I of this thesis.

A detailed error propagation analysis was performed by (Graff, 2013) on the freestream Reynolds number measured by the integrated Lucas Wind Tunnel data acquisition system. The uncertainty is 2.3% at the lowest velocity tested of $u_\infty = 20$ m/s, and decreases as u_∞ is increased.

The presence of a solid body in the test section results in a slight acceleration of the flow due to decreased effective cross-sectional area. The blockage, or projected frontal area, reaches up to 17% at the highest A_R and α tested. Various solid- and wake-blockage corrections have been proposed (Barlow, Rae, and Pope, 1999).

Instead of re-analyzing the Re uncertainty or applying boundary corrections, however, we simply demonstrate Re independence of the reported dimensionless coefficients C_L, C_D, and C_{LM}. Figure 2.14 plots these three values for a fixed wing planform as a function of Re at different α and δ. For most cases, their values remain relatively constant for $Re \gtrsim 10^6$, corresponding to $u_\infty = 25$ m/s. To ensure even less dependence on Re, this wing is tested at $u_\infty = 40$ m/s.

For wings with highest A_R, however, u_∞ is limited by the rolling moment capacity

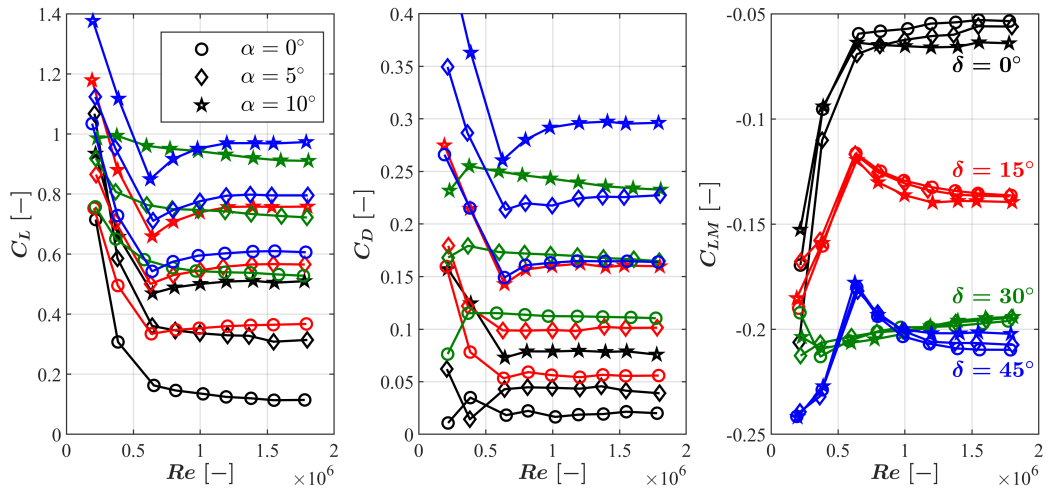

Figure 2.14: Re dependence of C_L, C_D, and C_{LM} for different α and δ on the $\Lambda = 30°$, $A_R = 1.3$ wing.

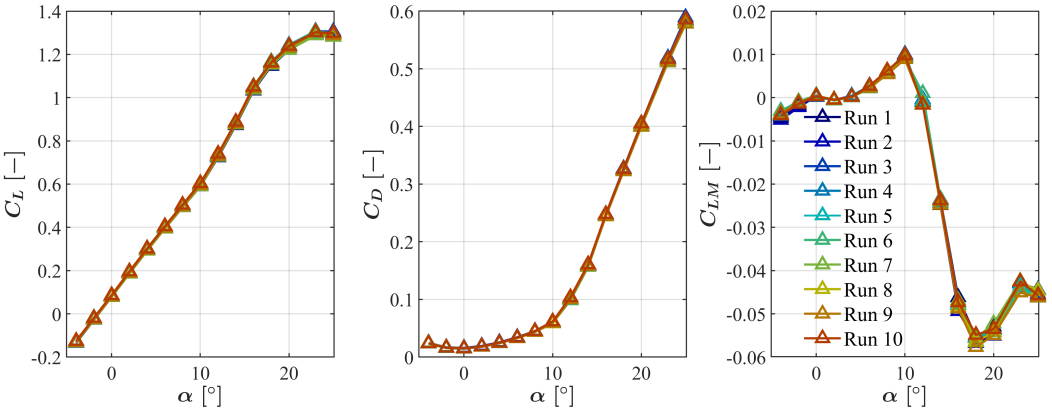

Figure 2.15: Repeatability of C_L, C_D, and C_{LM} measurements across ten trials on $\Lambda = 45°$, $A_R = 3.2$, $\delta = 0°$ at $Re = 1.0 \times 10^6$.

of the force balance especially at high α and δ. Under these extreme loads, physical interference is occasionally observed between the mounting base and fairing, rendering the balance measurements useless. In this case, Re is reduced to 1.0×10^6 but the repeatability of the results is confirmed. Figure 2.15 shows the consistency of C_L, C_D, and C_{LM} curves across ten independent trials. The uncertainty of each value, computed as the ratio of the standard deviation to the mean, is plotted in Figure 2.16. Except for large uncertainty in C_L observed at $\alpha = 2°$ due to division by a small number, the uncertainty is generally less than 3%, indicating that the experiments are very repeatable for a given configuration.

With Re independence at high Re and experiment repeatability established for

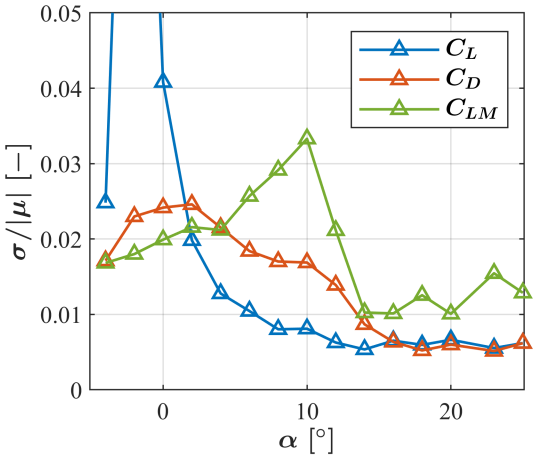

Figure 2.16: Uncertainty across the ten trials reported in Figure 2.15, computed as the ratio of standard deviation to the mean.

baseline flows, we investigate the effect of surface tufting. Tufting is an intrusive technique, meaning that physical objects (i.e., strings) introduced may potentially alter the flow we are trying to measure.

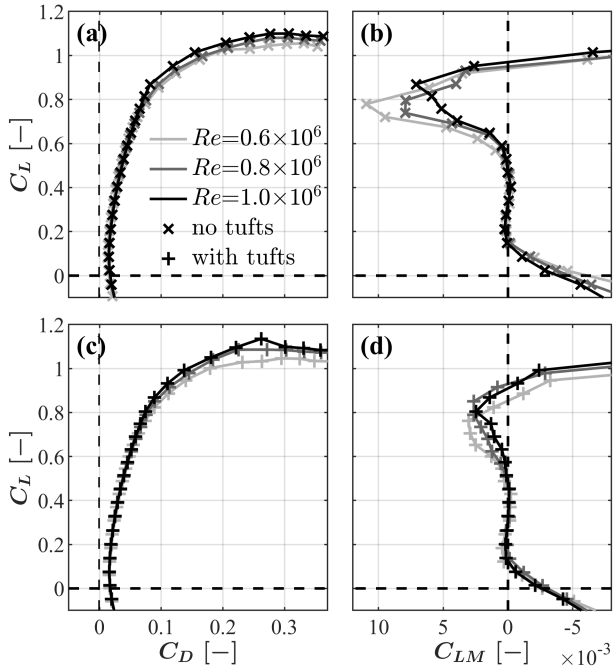

Figure 2.17: Effect of Re and tufts on the drag and pitching moment polars of the $\Lambda = 30°$, $A_R = 3.8$ wing.

Results for the $\Lambda = 30°$, $A_R = 3.8$ wing are shown with and without tufts at three (relatively low) Re in Figure 2.17. Both drag and pitching moment polar are largely

unaffected by either Re or the presence of tufts below $C_L = 0.6$ when the flow is fully attached. However, both factors become important at higher C_L when separation effects begin to dominate.

Without tufts in Figure 2.17(a), the upper portion of the drag polar is pushed upward with increasing Re. The wing produces more lift at a given α at higher Re because the flow is able to overcome the adverse pressure gradient and remain attached until further downstream. The effect on drag depends on the separation details, with drag decreasing for $C_L < 1$ and increasing for $C_L > 1$. With tufts in (c), the difference between $Re = 0.8$ and 1.0×10^6 seems to diminish over the entire range of α tested, except for the exact point of stall (e.g., maximum C_L). At this point, the flow is fully separated and the tufts are fluttering vigorously. Otherwise, the tufts most likely act as additional trip strips to further reduce the dependence on Re.

	Re (10^6)	x_{MRP}/c	$C_{LM,0}$
no tufts	0.6	0.758	-0.0547
	0.8	0.757	-0.0567
	1.0	0.755	-0.0582
with tufts	0.6	0.754	-0.0541
	0.8	0.754	-0.0548
	1.0	0.752	-0.0557

Table 2.3: Effect of Re and tufts on MRP location and required trim offset.

This is further corroborated by comparing pitching moment polars. Without tufts in (b), increasing Re noticeably decreases the maximum C_{LM} achieved during the unstable pitch departure. With tufts in (d), the maximum C_{LM} is decreased even further. However, its value remains constant at about 0.003 with increasing Re although the point of pitch departure is delayed slightly. Table 2.3 lists the location of the mean rotation point x_{MRP} and the trim offset C_{LM} applied to each case. The variance in these values with Re is reduced with tufts.

These results suggest that tufts generally reduce Re dependence, which is especially helpful for the larger wings which are limited to testing at lower Re. While the pressure distribution over the wing may be slightly affected, the overall longitudinal stability characteristics of the wing remains unchanged. This provides validation for all the baseline results presented in this chapter, which were taken with surface tufts and at the highest u_∞ allowable by the rolling moment limit at maximum flap deflection, summarized in Table 2.4.

Λ	A_R	u_∞ [m/s]	Re (10^6)
30°	1.3	40	1.6
	2.6	30	1.2
	3.8	20	0.8
45°	1.5	30	1.5
	2.3	25	1.2
	3.2	20	1.0

Table 2.4: Nominal free stream velocity and Re each wing was tested at.

The question remains, however, of whether the argument continues to hold in future chapters involving AFC. Figures 2.18 & 2.19 address this issue in turn for tufts and Re, respectively.

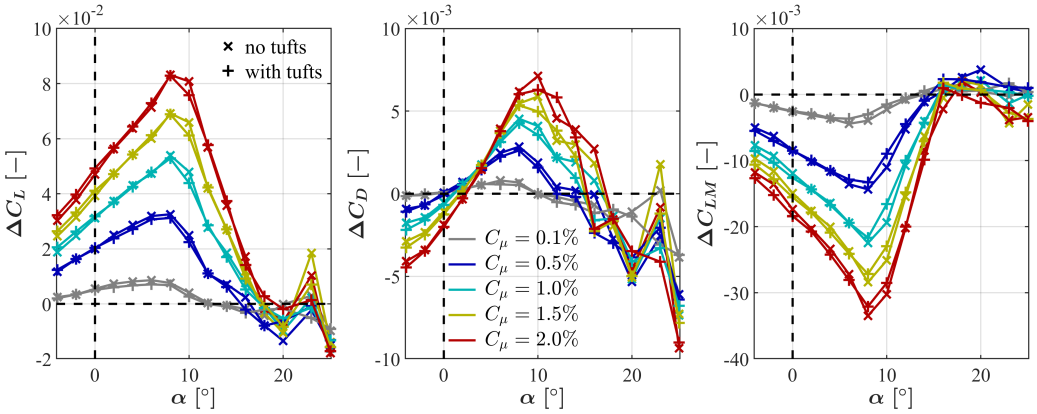

Figure 2.18: Effect of tufting on the changes effected by AFC on the $\Lambda = 45°$, $A_R = 3.2$, $\delta = 0°$ wing. All $n_j = 36$ actuators are active at five different levels of C_μ.

The AFC Δ's, or changes in the force and moment coefficients due to blowing for a fixed geometry and actuator distribution, are compared for the tufted and untufted cases at five different C_μ levels in Figure 2.18. On this wing, the LEV forms at $\alpha = 10°$ and stall occurs at $\alpha = 22°$. The effect of tufting on ΔC_L and ΔC_{LM} is negligible all the way up to stall, except at the point of LEV inception where AFC efficacy is slightly reduced by tufts at higher C_μ. This can again be explained by role of tufts in helping the boundary layer remain attached. The effect of tufting on ΔC_D is negligible up to LEV inception at all C_μ, and then for slightly higher α at low C_μ. However, differences become noticeable beyond $\alpha = 10°$ particularly for $C_\mu = 2.0\%$. At $\alpha = 16°$, AFC increases the drag on the wing without tufts but decreases the drag with tufts. While the effect of AFC on drag will be discussed in

Section 4.2, post-LEV behavior will not affect the major conclusions drawn. Thus, the presence of tufts is still justified for the AFC investigations.

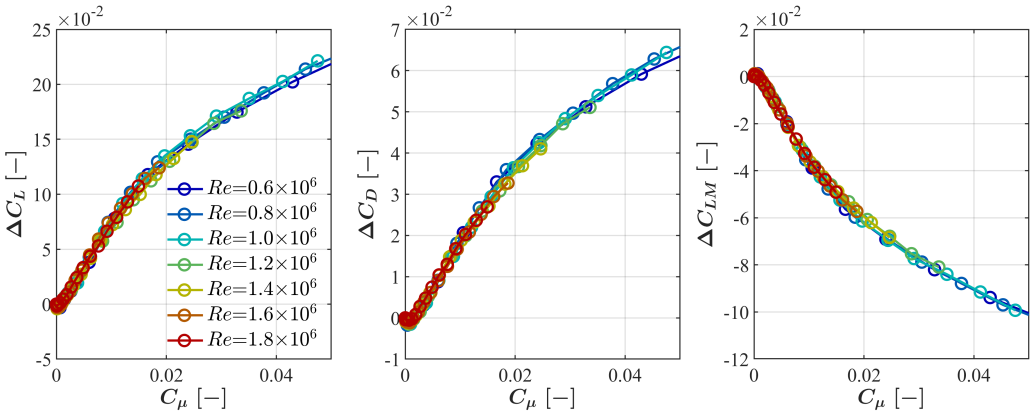

Figure 2.19: Effect of Re on the changes effected by AFC on the $\Lambda = 30°$, $A_R = 1.3$ wing oriented at $\alpha = 8°$, $\delta = 30°$.

Finally, the effect of Re on the AFC Δ's are investigated in Figure 2.19 on an untufted wing of fixed geometry. C_μ collapses the ΔC_L data onto a single curve across the entire range of Re tested. Note here that the ΔC_L is Re-independent even at the lower Re where the value of C_L itself depends on Re. The same applies to ΔC_D and ΔC_{LM}. Results presented in this thesis do not exceed $C_\mu = 2.0\%$, especially since the objective is to optimize and minimize the required input. However, this scaling can be helpful if future work involves consideration of higher C_μ, since mass flow rate through the SJA system is constrained by the available air supply pressure.

Chapter 3

FLUID POWER COEFFICIENTS AND SYSTEM DESIGN

The study of fluid mechanics, like many other branches of physics, is centered on describing and explaining the transport of mass, momentum, and energy. In principle, the set of partial differential equations that characterize the balance of these three quantities, combined with thermodynamic or material constraints on the fluid, provide a complete and accurate description of any flow field we might encounter. Thus, experimental aerodynamicists seek to measure these quantities, either directly or indirectly, to understand phenomena or drive design decisions.

For the past seven decades, the momentum coefficient C_μ has predominantly been used to study the flow physics and dynamics of blowing systems. The custom emerged from both practical and theoretical considerations and led to great strides in the field of flow control. However, the difficulty of measuring momentum flux, especially on complex actuation devices, resulted in non-uniform, inaccurate, or incomplete documentation across the literature. Furthermore, restrictions are often placed on flow rate or supply power rather than momentum when designing an actual vehicle, making it difficult for engineers to directly rely on the wealth of available quantitative data. This has motivated a push for recommended or standardized practices within the flow control community to report coefficients for all three fundamental quantities (Woszidlo and Little, 2021).

This chapter showcases the utility of the power coefficient C_π for blowing flow control. We revisit data from the earliest boundary layer control experiments on airfoils to demonstrate that C_π does just as well as C_μ in scaling the lift on steady 2D configurations. This conclusion is corroborated on a similar setup at the University of Arizona[1], and the analysis is extended to include the air supply system. The newly developed approach is applied to the swept wing with an array of sweeping jet actuators, which is a much more complex 3D system. Results highlight the importance of integrating AFC into the early conceptual design cycle of aircraft rather than optimizing it as an add-on feature to improve a frozen configuration.

[1]These experiments were performed by Johannes Reichert, but results were analyzed collaboratively.

3.1 Momentum vs power coefficients

Poisson-Quinton, who led the aeronautical research in France during the introduction of the jet engine to aviation, introduced the volume flow coefficient C_Q for suction BLC (Poisson-Quinton, 1948). The effect of slot suction on the flow was well understood and predicted by inviscid flow models that were generalized using electro-magnetic analogy (Malavard, 1961). Strong slot suction, represented mathematically by a sink in two-dimensional (2D) ideal flow, correctly predicted the additional lift generated and enabled optimization of slot location. However, the installation of a massive suction system for lift generation was not reduced to practice, although it was tested in conjunction with an ejector that augmented the thrust obtained by blowing (Poisson-Quinton and Lepage, 1961).

However, inviscid models could not be extended to blowing BLC because they excluded turbulent jet entrainment that contributes substantially to the lift when the blowing slot is located on the upper surface of a wing (Wygnanski and Newman, 1964). Thus, C_Q did not scale the data well for lift generated by steady blowing. Poisson-Quinton instead selected C_μ because it reasonably collapsed the lift generated across different slot widths onto a single representative curve. There was no theoretical backing for this choice other than the need to account for jet thrust, thus C_μ had to resemble thrust coefficient. The results that led Poisson-Quinton to consider C_μ as the leading parameter defining the effect of blowing over wings are digitized in Figure 3.1(a) & (b).

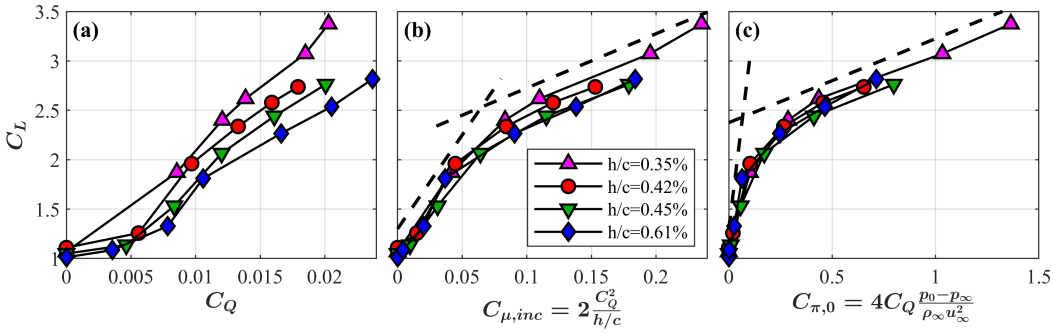

Figure 3.1: Variation of lift on a thick airfoil with (a) C_Q, (b), $C_{\mu,inc}$ and $C_{\pi,0}$. Data from (Poisson-Quinton, 1948), taken at $\delta = 45°$ and $Re = 0.9 \times 10^6$, was digitized and recast in terms of the plenum power coefficient.

In this article, we argue for the use of fluid power coefficients defined by the product of flow rate and pressure for blowing applications. In (c), Poisson-Quinton's data

was recast in terms of the actuator plenum power coefficient:

$$C_{\pi,0} = 4C_Q \frac{p_0 - p_\infty}{\rho_\infty u_\infty^2} \tag{3.1}$$

which collapsed the data just as well as C_μ onto a representative curve. Poisson-Quinton & LePage noticed that the measured lift exceeded the theoretical value determined by potential flow solution beyond some critical value $C_{\mu r}$. This corresponded approximately to a change in the slope of the $C_L - C_\mu$ curve (dashed lines in (b) & (c)), giving rise to a new flow regime called "super-circulation" where the additional C_μ beyond recovery of frictional losses altered the state of the flow to outdo inviscid performance limitations. The idea caught on and many inviscid "jet-flap" models (Spence, 1958a; Spence, 1958b) on wings of various shapes followed in an attempt to explain the phenomenon and the fact that much of the jet momentum was recovered as thrust irrespective of its injection angle relative to the free stream (Davidson, 1956).

In view of the accumulated evidence, one may take a more practical path by characterizing the fluidic power input to the actuators $C_{\pi,0}$ and to the entire system $C_{\pi,sys}$, as it is commonly done with electrical power when the actuators are electrically driven. An actuator plenum power coefficient$C_{\pi,0}$ defined by the product of plenum pressure and flow rate, both of which are easily measured in situ, scaled lift data for 2D steady BLC as well as the venerable C_μ. However, only on rare occasions are losses in the feeder system small, while the efficiency of a 2D nozzle is high. Having an additional total pressure measurement, p_t, at the system entrance enables us to similarly define a system power coefficient

$$C_{\pi,sys} = 4C_{\mathcal{M}} \frac{p_t - p_\infty}{\rho_\infty u_\infty^2} \tag{3.2}$$

where $C_{\mathcal{M}} = \dot{m}_j/(\rho_\infty u_\infty S)$ is the dimensionless mass flow coefficient. $C_{\pi,sys}$ provides information about the needs of the entire blowing system to enable the choice of a compressor, and the difference between these two power coefficients helps assess the relative losses of the air supply system. They provide a rationale for comparing various actuation configurations even if they do not describe the flow mechanisms contributing to the aerodynamic performance changes. Thus, the use of fluid power coefficients seamlessly integrates the design of the flow control device into higher-level system design.

To demonstrate this concept first on a simple 2D configuration, steady blowing through a rectangular slot on a thick elliptical airfoil with deflected flap was tested

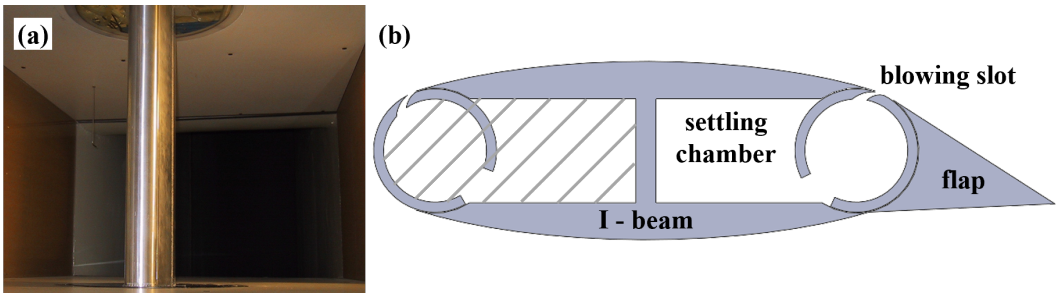

Figure 3.2: (a) Elliptical airfoil in the University of Arizona wind tunnel, and (b) a schematic drawing of its cross-section at $\alpha = 0°$ and $\delta = 15°$. Only TE blowing is used.

by Johannes Reichert at the University of Arizona. Tests were conducted in a 0.61 m $\times$ 1.04 m $\times$ 3.0 m test section of an open-loop cascade wind tunnel at low speeds that did not exceed $u_\infty = 15$ m/s, shown in Figure 3.2(a). The chord-based Re range tested was thus $1.7 \sim 3.4 \times 10^5$. Roughness strips were placed at mid-chord and the juncture between the LE cylinder and the main element on both suction and pressure sides to avoid boundary layer transitional effects. Lift is calculated from 52 static pressure measurements distributed around the airfoil.

The cross-sectional profile of the airfoil is shown in Figure 3.2(b). The main body approximates an ellipse with two circular arc segments at the LE and TE. With the flap attached, the airfoil has a chord of 34 cm and a thickness-to-chord ratio of 24%. An "I" beam divides the airfoil's interior volume into two independent settling chambers that can be either pressurized or evacuated, enabling blowing and suction at the LE and TE. The width and location of the slots can be adjusted by rotating the arcs and placing the appropriate shim stock into the slots before tightening the endplates. The large internal volume of the settling chamber allows the flow to stagnate in the interior of the wing.

Results presented in this thesis are limited to blowing over the flap shoulder (pressurized downstream chamber) for a fixed geometry of $\alpha = 0°$ and $\delta = 15°$. Readers interested in further studies of this elliptical airfoil should refer to (Chen, Seele, and Wygnanski, 2012; Chen, Seele, and Wygnanski, 2013).

In the first set of tests, air is supplied to the airfoil chamber using a centrifugal blower with maximum supply pressure of 9 kPa. To minimize pressure losses in the system, the blower is located as close to the airfoil as possible and connected to the settling chamber through short, large-diameter flexible hoses. The flow rate was controlled by the blower's RPM setting and measured by a float-type flow meter

limited to 0.020 m^3/s.

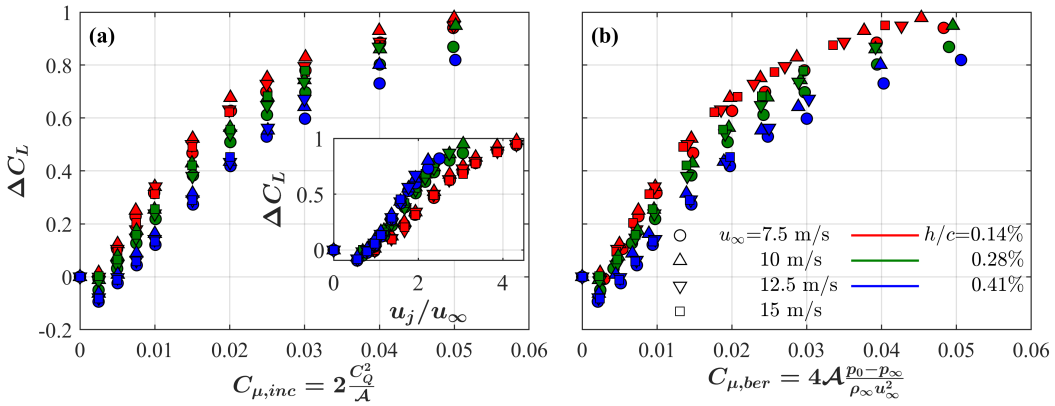

Figure 3.3: Lift increment ΔC_L due to steady blowing supplied by a centrifugal blower with minimal internal losses. The C_μ was estimated from (a) flow rate measurement and (b) Bernoulli's equation.

The freestream velocity, blowing slot width, and blower flow rate were varied. The achieved lift enhancement ΔC_L is plotted in Figure 3.3 as a function of C_μ computed (a) from the flow rate measurement assuming incompressible flow or (b) from the chamber pressure measurement applying Bernoulli's equation. The results are almost identical because the flow through the large supply hoses and convergent nozzle is indeed incompressible and frictional losses are negligible. However, neither form of the momentum coefficient is able to scale the data well onto a single representative curve. Both indicate a preference for thinner slots, suggesting that the jet velocity ratio may also be an important governing parameter (Attinello, 1961; Chen, Zakharin, and Wygnanski, 2008; Nagib et al., 2006). Replotting the results against u_j/u_∞ (inset in Figure 3.3(a) showed this effect clearly as the trend between slot widths reversed.

The jet is primarily a source of momentum when $u_j/u_\infty \gg 1$ but tends to become a source of mass flow when $u_j/u_\infty \sim O(1)$. A deleterious effect on lift is observed due to thickening of the boundary layer when the injected jet is slower than the free stream $u_j/u_\infty < 1$. To account for these different mechanisms, Attinello (Attinello, 1961) suggested a modification to the momentum coefficient

$$C_{\mu,mod} = C_\mu \left(1 - \frac{u_j}{u_\infty}\right) = C_\mu - 2C_Q \tag{3.3}$$

which collapses the data much better than C_μ, as shown in Figure 3.4(a).

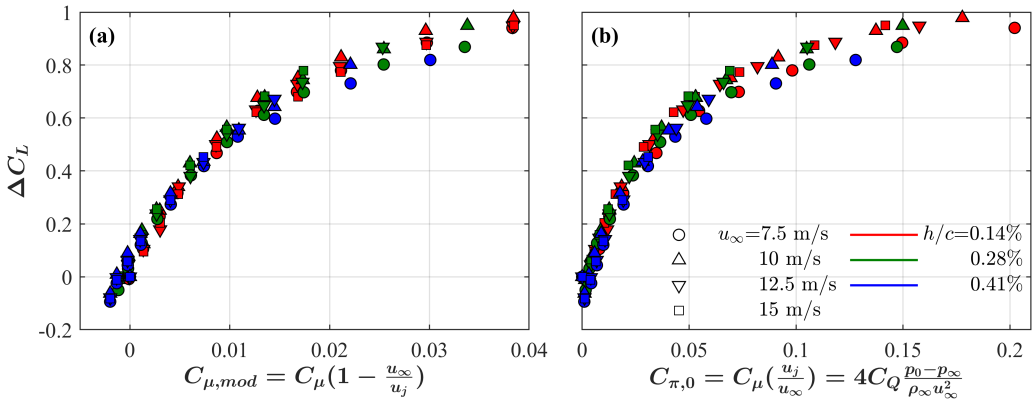

Figure 3.4: Dependence of ΔC_L on (a) $C_{\mu,mod}$ and (b) $C_{\pi,0}$ with the blower setup.

In Figure 3.4(b), we show that the plenum power coefficient $C_{\pi,0}$ scales the data just as well. This power coefficient is defined as the product of flow rate and supply pressure, but in the incompressible case can also be interpreted as another modification to C_μ by the jet velocity ratio:

$$C_{\pi,0} = 4C_Q\frac{p_0 - p_\infty}{\rho_\infty u_\infty^2} = C_\mu\left(\frac{u_j}{u_\infty}\right) \tag{3.4}$$

The added advantage to $C_\pi, 0$ is that it consists of quantities that are easily measured in situ, and naturally extends to design applications by enabling optimization of system configurations and prescribing the overall compressed air requirements.

We now ask how the system performance changes when the centrifugal blower is replaced by a high-pressure compressed air source (maximum 690 kPa) connected with longer and thinner tubing. The total supply pressure, and consequently the flow rate, is regulated and measured at an electronically-controlled valve plumbed to the settling chamber with a 91.4 cm long, 1.27 cm diameter hose in which non-negligible pressure losses are expected. The ΔC_L vs $C_{\pi,0}$ values obtained with this new setup are plotted in color in Figure 3.5(a), superposed on top of the data from the previous setup in light gray. The two datasets overlap, indicating, as expected, that the flow over the airfoil and its effect on lift are independent of the way the air is supplied to the settling chamber. The plenum power coefficient enables us to see that the exterior flow physics thus remain unchanged between these two tests.

To assess the total utility of the entire system, we consider $C_{\pi,sys}$ where the total pressure p_0 measured in the settling chamber is replaced by p_t measured at the control valve, as given in Equation 3.2. Note that mass flow rate $C_\mathcal{M}$ and volume flow rate C_Q are equivalent in incompressible flow. The results plotted in Figure

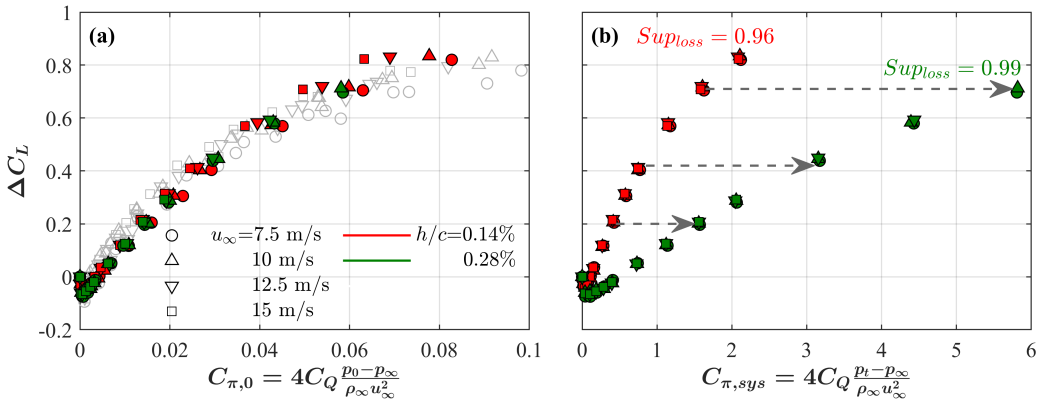

Figure 3.5: Dependence of ΔC_L on (a) $C_{\pi,0}$ and (b) $C_{\pi,sys}$ with the compressed air setup. Light gray points are from the blower setup (Figure 3.4(b)).

3.5(b) suggest that $C_{\pi,sys}$ still scales the data well with respect to changes in u_∞ for an entirely frozen design, but now reveals large differences in performance with respect to slot width. Since the plenum and system power coefficients were defined in the same form, the relative losses in the supply system can be quantified by

$$Sup_{loss} = \frac{C_{\pi,sys} - C_{\pi,0}}{C_{\pi,sys}} \tag{3.5}$$

Its value is 0.99 and 0.96, respectively, for the wider and thinner slots at the highest input tested. Thus, losses across the nozzle are negligible and most of the pressure loss is attributed to the supply chain leading up to the settling chamber which scales with the square of the average velocity through the plumbing components. By doubling the slot width from $h/c = 0.14\%$ to 0.28%, flow rate doubles and pressure loss quadruples. This is indeed the case throughout the entire range of $C_{\pi,sys}$ tested, as marked by gray arrows in the figure for a given ΔC_L. Smaller slot widths provide higher system efficiency because they increase the system's pressure while lowering the mass flow for a given power input on a given installation, reducing the plumbing losses that were the dominant factors in this test. In practice, engineering considerations such as the weight of the plumbing or safety factors also become important. The optimization procedure between the air supply chain and AFC actuation efficacy is strongly coupled, but its significance is lost when using only $C_{\mu,mod}$ which only accounts for the exterior effects of the jet on the flow.

For over 70 years, the momentum coefficient has been the leading parameter of choice reported in the blowing flow control literature because of its ability to scale data and because momentum shares the same dimensions as force. This made sense

in the context of fundamental studies of the flow dynamics, and many studies have gone to great lengths to characterize the jet exit velocity profile needed to accurately compute the momentum injected but often made difficult by its non-uniformity in both time and space. AFC technology has now matured into its own subdiscipline of aeronautical engineering, and the accumulated physical knowledge must be applied to system-level design of next-generation aircraft. However, this step cannot be made with measures of momentum, which decouples the exterior flow physics from the interior air supply chain. The proposed power coefficient approach may serve as the bridge without compromising the desirable data-scaling abilities C_μ provided for fundamental studies.

3.2 Measuring power coefficients on the swept wing

We now apply the systems approach developed in the previous section to a more complex, 3D configuration: an array of SJAs on a swept wing.

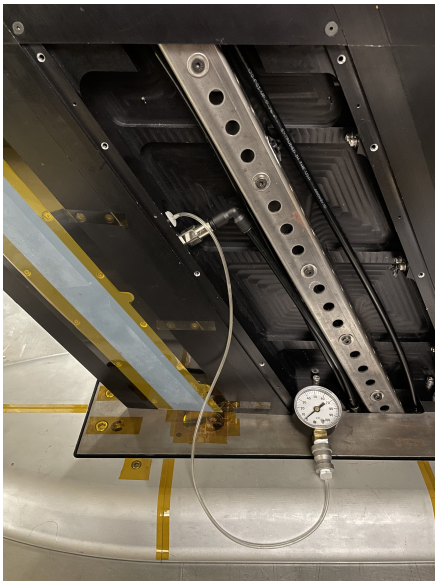

Figure 3.6: Ashcroft pressure gauge setup for calibrating plenum pressure on the swept wing model.

The plenum pressure p_0 is calibrated for different actuator configurations and inputs on a single wing element in the absence of a free stream using an Ashcroft gauge. The calibration setup is depicted in Figure 3.6, where the cover on the pressure side of the wing is removed to access the plenum. Refer back to Figure 1.5 for details on the plumbing configuration and the actuator array assembly. It should be noted that unlike the thick elliptical airfoil, p_0 inside a thin wing may not always represent stagnation conditions because of volume limitations.

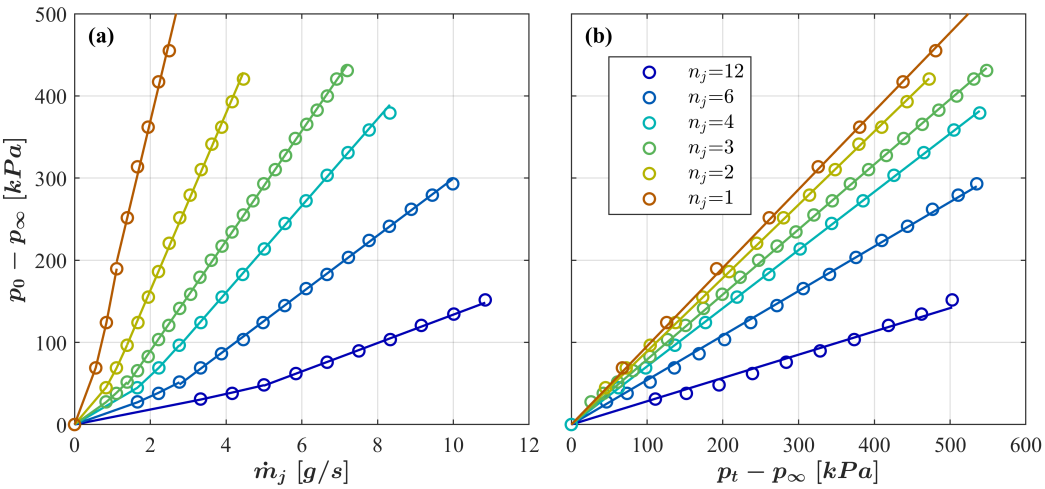

Figure 3.7: Calibration of plenum pressure p_0 against (a) flow rate $\dot{m}_j$ and (b) pressure p_t measured at the system inlet.

The plenum pressure is plotted as a function of mass flow rate in Figure 3.7(a) for different numbers of active actuators. A piecewise quadratic + linear curve is fitted to each, inspired by the findings of (D.G. Hirsch, 2017) that the relationship between jet momentum and flow rate switches from quadratic to linear when the flow chokes (i.e., becomes sonic at the nozzle). Each actuator can intuitively be thought of as a resistive element, so a higher plenum pressure is required to push a given $\dot{m}_j$ through fewer actuators and vice versa.

In Figure 3.7(b), the data is replotted in terms of the supply pressure p_t at the flow controller. Now, the trend is linear across the entire range, and the slope of the fitted line is an indicator for losses in the supply chain for a given configuration. Specifically, Equation 3.5 can be re-written in terms of the slope as

$$Sup_{loss} = 1 - \frac{p_0 - p_\infty}{p_t - p_\infty} \tag{3.6}$$

Frictional losses are approximately proportional to the average dynamic pressure through the plumbing components. Configurations with fewer actuators, which operate at lower flow rates, therefore experience lower pressure losses. When $n_j = 1$, $Sup_{loss} = 0.046$ so losses in the supply chain are much smaller than those across the actuator even with the extensive plumbing length. On the other hand, activating all 12 actuators increases Sup_{loss} to 0.716.

Figure 3.8 considers the same quantities on a "per actuator" basis. In (a), the distribution sparsity of the actuator array is again varied between $n_j = 1$ and 12. All data collapses onto a single representative curve, suggesting that the plenum is

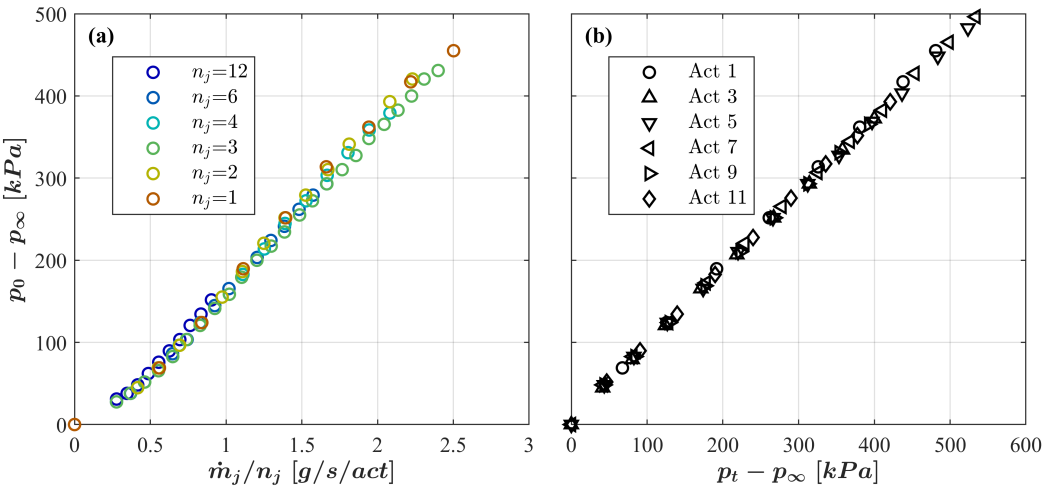

Figure 3.8: Plenum calibration data plotted on a per-actuator basis to validate the uniformity assumption. (a) The x-values of Figure 3.7(a) have been divided by the respective n_j, and (b) different actuators in the array are tested individually (Act 1 is closest to the wing root).

sufficiently large for the range of cases considered in this study and the actuators in the array may be assumed to behave uniformly. To further corroborate uniformity across actuators, six actuators in the array are activated individually, and supply vs plenum pressure is plotted in (b). This data also collapses onto a single curve.

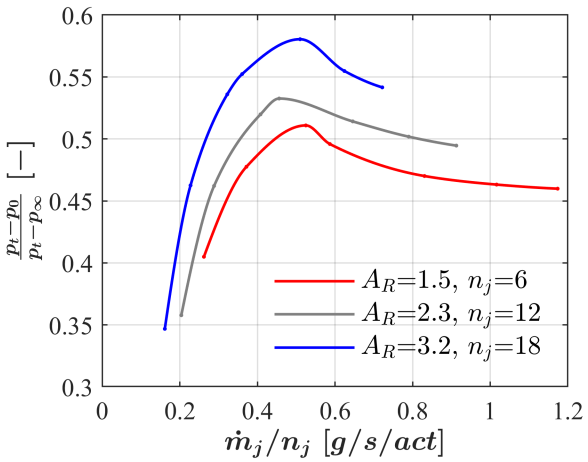

Figure 3.9: Relative pressure losses in the supply chain as a function of mass flow rate per actuator on the $\Lambda = 45°$ wing at different A_R for a fixed actuator spacing ξ_s.

The swept wing model used in this study can have up to three such arrays of twelve actuators, one for each wing element. Figure 3.9 shows the fractional pressure drop across the air supply chain (i.e., Sup_{loss}) as a function of the mass flow rate per

actuator for the $\Lambda = 45°$ wing at three different A_R. The actuator spacing is fixed at $\xi_s = 7.6$ cm so the number of actuators n_j increases proportionally with A_R. The peak of all three curves occurs at around 0.5 g/s/actuator, which may be related to choking conditions for this actuator geometry. However, the relative losses in the supply chain increase with n_j because all the air passes through a single tube upstream of the valve, and higher flow rates incur larger losses.

The AFC system was characterized by calibrating p_0 measured at the actuator inlet against p_t and $\dot{m}_j$ measured at the flow controller. These quantities enable computation of power coefficients $C_{\pi,0}$ and $C_{\pi,sys}$ to assess AFC efficacy when the wing is tested in the presence of a free stream. Optimization of the air supply configuration becomes increasingly critical as more actuators are deployed on a vehicle, which should drive high-level design decisions on how the entire AFC system is integrated.

3.3 Integration of AFC into systems design

The efficacy of a blowing system depends significantly on the baseline flow that it is trying to alter. Thus the design and operational geometries of the wing are important independent variables to consider in the conceptual design of AFC.

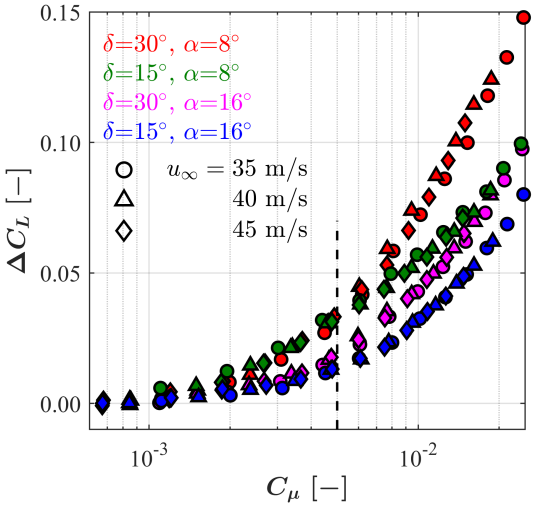

Figure 3.10: Effect of operational geometry (α, δ) for a fixed wing planform geometry ($\Lambda = 30°$, $A_R = 1.3$) and actuator distribution $n_j = 12$.

Consider first the effect of airfoil orientation (α, δ) while the wing planform and actuator distribution remain fixed. Lift increment is plotted against C_μ in Figure 3.10 for the ($\Lambda = 30°$, $A_R = 1.3$) wing with all twelve actuators active. Colors

and markers correspond to airfoil orientation and freestream velocity, respectively. C_μ, $C_{\pi,0}$, and $C_{\pi,sys}$ all displayed similar trends because the AFC configuration was completely frozen. Compare the rightmost point of each curve at $C_\mu = 0.025$. For $\alpha = 8°$ and $\delta = 15°$ (green), ΔC_L is 0.10, but by further deflecting the flap to $\delta = 30°$ (red), ΔC_L increases to 0.15. This suggests that the baseline flow at $\delta = 30°$ consisting of strong crossflow over the flap is more amenable to AFC, whereas $\delta = 15°$ does not enable full exploitation of AFC. Now, we increase α to 16° (magenta) and AFC loses some control authority as ΔC_L falls back down to 0.10. AFC is least effective across the entire C_μ range tested when the airfoil is at high α and low δ (blue). We also observe a behavioral threshold at $C_\mu = 0.005$, demarcated by a dashed line. The lift increment is dominated by α below this threshold and by δ above.

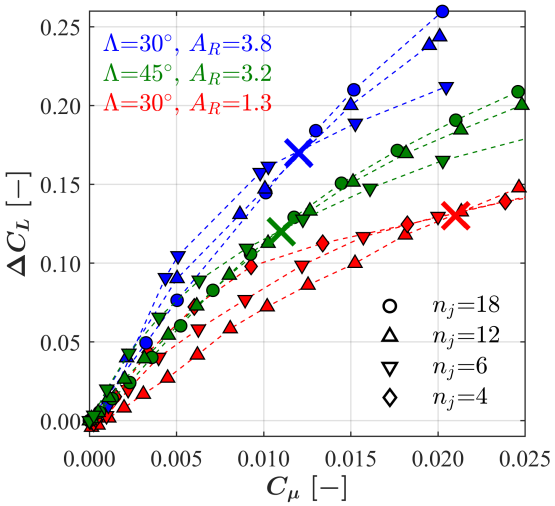

Figure 3.11: Effect of wing planform geometry (Λ, A_R) and actuator distribution sparsity on ΔC_L for a fixed operational geometry ($\alpha = 8°$, $\delta = 30°$).

We next investigate AFC efficacy with respect to wing planform (Λ, A_R) and actuator distribution density (ξ_s, or equivalently n_j). In Figure 3.11, lift increment is plotted against C_μ when the wing orientation is fixed at ($\alpha = 8°$, $\delta = 30°$). Freestream velocity is also fixed for each planform shape since we have observed that results are generally independent of Re. For each planform, a "cross-over" threshold is observed and marked by an X of the corresponding color. Sparser distributions generate more lift for a given input below this threshold, and denser distributions perform better above it. Physically, this illustrates the trade-off between jet velocity and region of influence. Using fewer actuators enables high jet speeds at low flow

rates but limits the area over which separated flow can be re-attached to the flap surface. For ($\Lambda = 30°$, $A_R = 1.3$), the cross-over occurs at $C_\mu = 0.021$. As A_R is increased to 3.8, the cross-over point decreases to 0.012 and general AFC efficacy increases. When sweep back is then increased to $\Lambda = 45°$ (A_R slightly decreases), AFC efficacy is reduced and the cross-over point is somewhat reduced. A remarkably similar behavior was observed on the 757 vertical tail model (Seele et al., 2013) although it was tapered and had a very different airfoil section.

Wing planform (Λ, A_R), which is fixed once the plane takes off, and airfoil orientation (α, δ), which changes throughout the flight, both had significant impacts on AFC lift enhancing efficacy. These results point to the importance of designing the AFC system and wing together in an iterative process that also considers the intended mission profile.

In 3D flow configurations, AFC efficacy also depends significantly on spanwise actuation location. Suppose we now completely freeze the wing geometry at ($\Lambda = 45°$, $A_R = 3.2$, $\alpha = 8°$, $\delta = 30°$) and vary the actuator distribution while holding $\mathcal{A}$ (i.e., the total number of actuators) constant. The effect of four different distributions of twelve actuators is shown in Figure 3.12 to illustrate the full complexity of a 3D AFC system optimization.

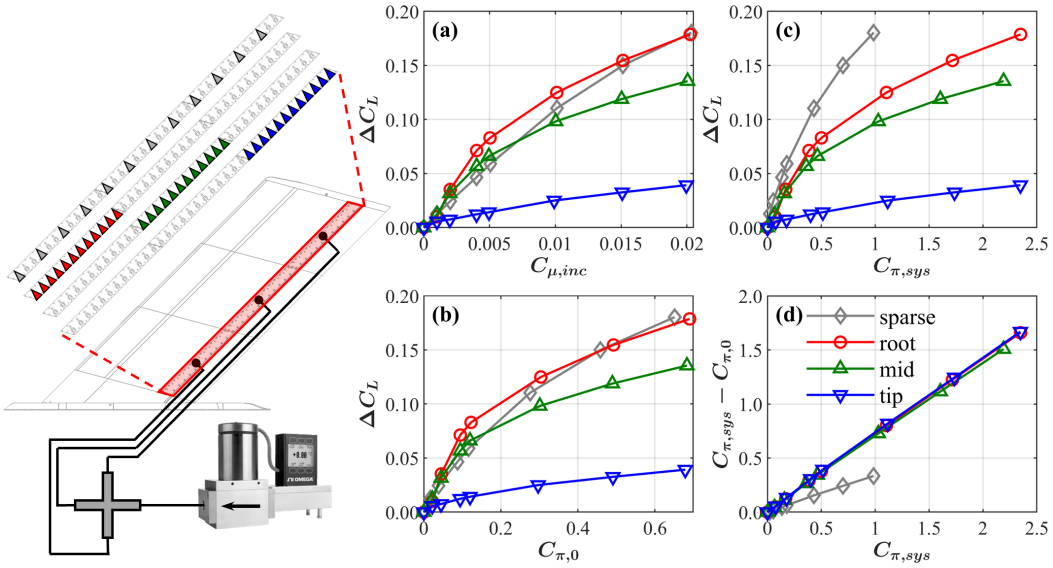

Figure 3.12: Dependence of ΔC_L on (a) $C_{\mu,inc}$, (b) $C_{\pi,0}$, and (c) $C_{\pi,sys}$ for different actuator distributions (left schematic) for fixed $n_j = 12$ and wing geometry $\Lambda = 45°$, $A_R = 3.2$, $\alpha = 8°$, $\delta = 30°$. (d) Fluid power losses incurred in the supply chain as a function of total system input power.

Densely distributed actuators among each of the three wing elements provided very different results due to the various interaction mechanisms occurring along the span. Most of the lift enhancement effect comes from redirecting and reattaching the flow over the deflected flap, which has a strong outboard velocity component as was shown in previous tuft visualizations. Thus, it makes sense that root actuation (red circles) targeting the source of this spanwise flow is most effective, and efficacy decreases slightly as actuation moves outboard (green triangles). Actuation at the tip (blue triangles) may also include interactions with the wingtip vortex.

Losses through the actuators for these three cases are expected to be identical since the same supply system configuration and number of actuators was used. Thus, we see very similar trends between (a) $C_{\mu,inc}$ based on mass flow only, (b) $C_{\pi,0}$ that considers the pressure loss across the actuators, and (c) $C_{\pi,sys}$ that also considers losses in the supply chain. In reality, losses through the supply chain may increase slightly as the actuators are moved outboard due to the increased length of plumbing required. The difference is negligible in this setup given the total length of plumbing in the rest of the supply chain, but would need to be considered during the optimization process of a real vehicle. In fact, trade-offs might even be made between installing a single central compressor at the expense of extensive plumbing (as in our setup), or a multitude of smaller compressors located near each actuator.

Plotting $C_{\pi,sys} - C_{\pi,0}$ in (d) shows that losses in the supply chain vary linearly with increasing $C_{\pi,sys}$, and they are independent of the actuation location. For densely distributed actuators, the losses in the supply chain are dominant since the slope of the curve, corresponding to Sup_{loss}, is 0.70. However, by distributing the 12 actuators evenly over the entire wing (grey diamonds), Sup_{loss} decreases to 0.34 which made this configuration appear to be much more effective than it really is under $C_{\pi,sys}$ in (c). In this case, the increase in system efficacy is entirely attributed to the improvement in the supply chain. Frictional losses downstream of the valve are reduced since the effective cross-sectional area of the plumbing was tripled. This interplay would not have been recognized by only assessing $C_{\mu,inc}$ or $C_{\pi,0}$, which both show similar trends. Using $C_{\pi,0}$ and $C_{\pi,sys}$ in tandem provides a framework for high-level optimizations, and enables understanding of the coupling between physics of 3D flow control over the wing and the plumbing losses associated with the blowing system installation.

The examples presented in this section only scratch the surface of the complexities that emerge when designing an AFC-enabled wing or aircraft. Since AFC is most

effective when it leverages instabilities in the existing turbulent shear flow, a truly integrated approach needs to consider the wing geometry (that generates the flow instabilities) alongside the AFC configuration (which targets these instabilities) during the early conceptual stages while keeping in mind the power and plumbing constraints. This forces us to reconsider the past practice of using C_μ as the primary independent variable defining AFC, along with the philosophy of designing AFC systems as simple add-on features to improve existing (frozen) designs.

Furthermore, a more comprehensive analysis would be required if we were to employ AFC for the various flow conditions and control objectives encountered in flight. Would actuators used for lift enhancement during takeoff also work to reduce drag during cruise? Provide maneuvering or stabilizing moments? The next chapter dives deeper into the flow interaction mechanisms involved in these different situations with an eye toward painting a qualitative picture of the optimal solution that can guide future conceptual design.

Chapter 4

UNDERSTANDING AND OPTIMIZATION OF AFC

With a solid grasp of the underlying interactions between the LEV and TES developed in Chapter 2 and the optimization approaches developed in Chapter 3, we are now ready to explore optimal actuation locations with respect to specific control objectives. Lift enhancement, drag reduction, and pitch stabilization are considered in this study. Each of these objectives is shown to have a different optimum actuation location along the span of the wing, which has interesting implications on design.

For most results presented in this chapter, spanwise actuation location is varied but the air supply chain is not, so C_μ (incompressible), $C_{\pi,0}$, and $C_{\pi,sys}$ are equivalent comparison platforms. Thus, the inputs are reported in terms of C_μ for convenience.

4.1 Interactions at the leading and trailing edges for lift enhancement

Increasing the lifting capabilities of a wing is important especially during takeoff and landing. The MOBLE wing has interchangeable flap components that deflect at 80% chord and is equipped with a spanwise array of sweeping jet actuators at the flap shoulder. We experimentally investigate the interplay between the LEV and trailing-edge actuation by examining lift C_L, lift slope $\partial C_L/\partial\alpha$, lift increment ΔC_L, and tuft visualizations.

The effect of Λ and δ on AFC lift-enhancing capabilities is demonstrated in Figure 4.1, which plots lift (solid lines) and lift slope (dashed lines) on the three-element wings at different C_μ levels. Each plot presents a different combination (Λ, δ), where columns correspond to $\Lambda = 30°$ and 45° and rows correspond to $\delta = 0°$ and 30°. The same actuator configuration of 18 sparsely distributed actuators along the entire wingspan is used in all four cases. Recall that the LEV forms at $\alpha = 12°$ for $\Lambda = 30°$ and $\alpha = 10°$ for $\Lambda = 45°$ when the flap is undeflected. We analyze the changing balance between LEV formation, contribution of vortex lift, and separation leading to stall with wing geometry and AFC input.

A universal trend observed across all four configurations is that AFC tends to smooth out the effect of vortex lift. With no actuation, lift slope is relatively constant until LEV formation, at which point there is a rise in the curve due to the generation of vortex lift. As α is further increased, lift slope begins to decrease again due

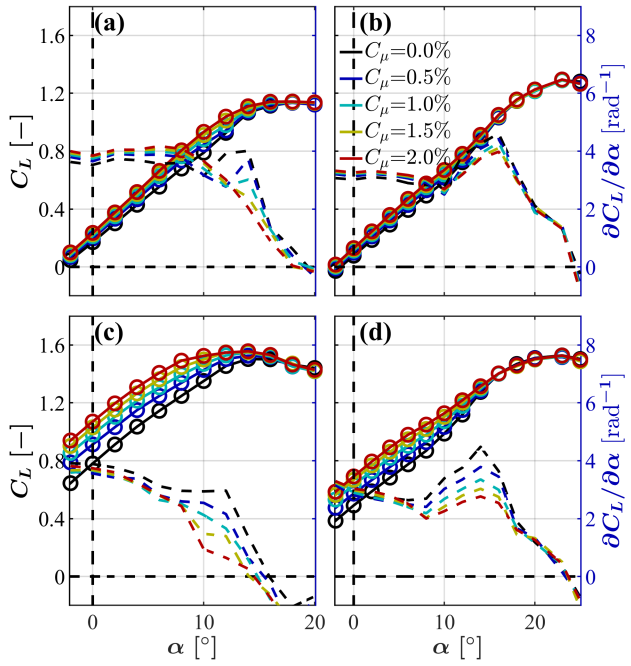

Figure 4.1: Comparison of lift (solid lines) and lift slope (dashed lines) when $n_j = 18$ SJAs are uniformly distributed across the three-element wing. (a) $\Lambda = 30°$, $\delta = 0°$, (b) $\Lambda = 45°$, $\delta = 0°$, (c) $\Lambda = 30°$, $\delta = 30°$, (d) $\Lambda = 45°$, $\delta = 30°$.

to separation effects and becomes negative at the stalling point as maximum lift is reached. Looking at the dashed black lines, this "bump" in $\partial C_L/\partial\alpha$ occurs over $10° \leq \alpha \leq 16°$ in (a) and $8° \leq \alpha \leq 18°$ in (d). As C_μ is increased, the bump is reduced and the lift slope curve becomes smoother. This effect can be seen in all four plots, although the degree to which it occurs and the quantitative details vary significantly. Very little difference is observed in (b), the effect of vortex lift is eliminated at $C_\mu = 1.5\%$ in (a) and 1.0% in (c), and the direction of the kink is reversed at high C_μ in (c). These differences can be explained by the dominant flow mechanism.

The lift enhancement effect due to AFC dominates at lower sweep, but vortex lift dominates at higher sweep. This is consistent with the competition between TES and LEV observed in the baseline analysis. AFC dominates and overcomes the vortex lift at $\Lambda = 30°$, entirely smoothing out the lift slope curve and increasing the value of $C_{L,max}$ (note this does not mean that the LEV is suppressed or destroyed). In contrast, vortex lift is too strong at $\Lambda = 45°$, and $C_\mu = 2.0\%$ is not enough to augment lift beyond $\alpha = 18°$.

AFC authority significantly increases when the flap is deflected because it taps into

a shear flow instability. Comparing (a) with (c) for $\Lambda = 30°$ and (b) with (d) for $\Lambda = 45°$, AFC clearly has a larger effect in the $\delta = 30°$ cases in terms of lift increment in the attached flow regime and lift slope smoothing in the vortex lift regime. This is because the primary mechanism of AFC shifts from enhancing circulation by energizing the boundary layer at $\delta = 0°$ to re-attaching the separated shear layer at $\delta = 30°$. The superiority of oscillatory jets for separation control has been previously demonstrated on a NACA 0012 (Seifert et al., 1993). Even at $\Lambda = 45°$ when the vortex lift effect is strong, $C_\mu = 2.0\%$ overcomes most of it, but at $\Lambda = 30°$ AFC dominates and even reverses the direction of the bump in $\partial C_L/\partial\alpha$.

The separation caused by flap deflection also changed the dynamics before LEV formation, creating interesting dependencies of $\partial C_L/\partial\alpha$ on α and C_μ. In (a) and (b) where $\delta = 0°$, $\partial C_L/\partial\alpha$ is constant with α and increases with C_μ. In (c) and (d) when the flap is deflected, $\partial C_L/\partial\alpha$ decreases with α for $\alpha = 8°$ and there is no clear trend with C_μ. Also note that the vortex lift region begins at a slightly lower α when the flap is deflected.

By comparing the lift and its derivative with respect to α across different wing shapes and C_μ values, we see the interplay between the LEV, TES, and oscillatory blowing. To summarize the flow interaction mechanisms that can be understood from Figure 4.1, AFC enhances lift primarily by increasing circulation when the flap is undeflected and by re-attaching the separated shear layer when the flap is deflected to 30°, and its effect is stronger over the deflected flap. In both cases, AFC also mitigates the strong spanwise flow component. Competing with AFC is the vortex lift increment due to the LEV, which is stronger at higher sweep back. The vortex lift effect dominates for $(\Lambda = 45°, \delta = 0°)$ and AFC has a very small impact on $\partial C_L/\partial\alpha$ on α and $C_{L,max}$, whereas the AFC effect dominates for $(\Lambda = 30°, \delta = 30°)$ and increases lift all the way up to stall. These results suggest that the efficacy of the SJAs to augment lift is closely coupled with the formation of the LEV.

We showed earlier that the onset of LEV is most clearly indicated by drag measurements. In Figure 4.2, the drag slope $\partial C_D/\partial\alpha$ on α is plotted against α in dashed lines for the same four configurations as Figure 4.1. There is a spike in the drag slope curve across all geometries and C_μ values, indicating a sudden increase in drag caused by the low-pressure bubble associated with the LEV. When the flap is undeflected (a,b), trailing edge AFC has almost no effect on drag, except for slightly delaying the LEV formation at $\Lambda = 30°$ which manifests as a shift in spike location. Larger effects on drag are observed when $\delta = 30°$ (c,d) due to flow re-attachment

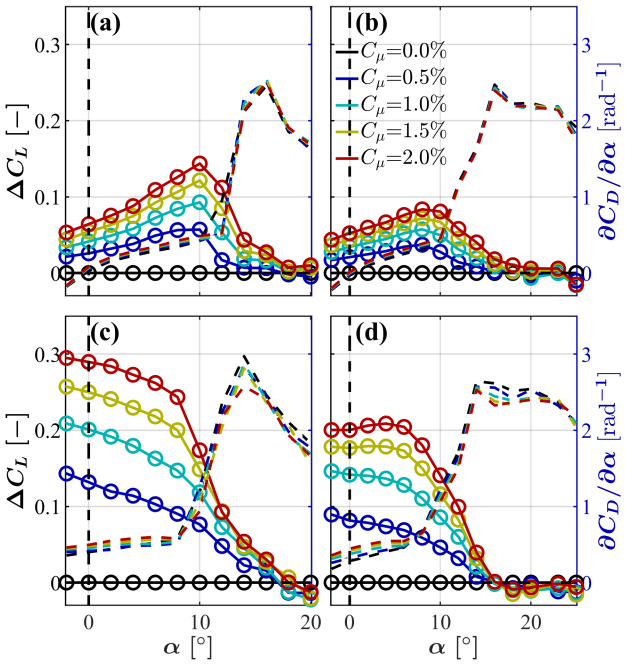

Figure 4.2: Comparison of lift increment (solid lines) and drag slope (dashed lines) for the same configurations as Figure 4.1. (a) $\Lambda = 30°$, $\delta = 0°$, (b) $\Lambda = 45°$, $\delta = 0°$, (c) $\Lambda = 30°$, $\delta = 30°$, (d) $\Lambda = 45°$, $\delta = 30°$.

and mitigation of outboard flow.

The relationship between trailing edge AFC and LEV formation becomes clear when the lift increment ΔC_L is superposed on the drag slope. For each configuration, the formation of LEV coincides with the decay of ΔC_L until it reaches zero near or before stall. Thus, the onset of the LEV can be thought of as an efficacy threshold for lift enhancement capabilities due to circulation control via trailing-edge blowing. This threshold is common across all cases, pointing to the importance of understanding LEV behavior in design and the universality of its interaction mechanisms with blowing at the TE.

Since wings with moderate sweep mainly operate in the attached flow regime, it is also worthwhile looking at AFC performance at α prior to LEV formation. When the flap is undeflected (a,b), the baseline flow is fully attached and the lift increment due to AFC increases with α. When the flap is deflected to 30°, ΔC_L is constant with α at $\Lambda = 45°$ but decreases with α at $\Lambda = 30°$. The magnitude of ΔC_L is generally larger when the flap is deflected and lower at $\Lambda = 45°$, reaching as high as 0.3 (20% of $C_{L,max}$) in (c) with $C_\mu = 2.0\%$. These trends again imply that different mechanisms are at play. With no flap deflection, blowing at the trailing

edge increases circulation for moderate gains in lift. AFC authority significantly increases when the flap is deflected, as separated flow is re-attached and directed downward for increased lift.

So far, we have analyzed the effect of geometric parameters on AFC efficacy while keeping the actuator distribution fixed. Given the highly three-dimensional nature of the flow over swept wings, however, we expect ΔC_L to depend on blowing location. Next, we investigate how different actuator distributions interact with the attached flow and vortex lift regimes.

4.2 Drag reduction and cruise efficiency

The ΔC_L measured on the $\Lambda = 45°$, $A_R = 2.3$ wing with various sectional distributions of six actuators at $C_\mu = 2.0\%$ are shown in Figure 4.3(a). We observe familiar trends: actuation near the root generates more lift than near the tip, and peaks of the ΔC_L curves mostly coincide with LEV formation at $\alpha = 10°$. However, note the interesting exception for Jets 1-6. The lift-enhancing performance of this distribution is relatively constant over $6 < \alpha < 18°$ and does not begin to deteriorate until $\alpha = 18°$, which is significantly beyond the inception of the LEV. The reason for this becomes clear when looking at a tuft visualization (c) of the wing at $\alpha = 16°$ with no actuation (orange) and root actuation at $C_\mu = 2.0\%$ (dark blue). Although the LEV has propagated significantly inboard, it has not yet reached the region of influence of the sweeping jet actuators, as outlined in black. The actuators are positioned to avoid interaction with the LEV and thus can retain their flow control authority at the trailing edge.

Unfortunately, root actuation at high α is accompanied by a cost of increased drag, as shown in (b). On the other hand, tip actuation can reduce drag at all α by mitigating the tip vortex footprint. These competing mechanisms further motivate the integration of AFC into the early design loop so that actuation distributions can be optimized with respect to various control objectives and changed on-demand throughout the flight.

Thus far, we have analyzed how LEV instigation and propagation affects actuator performance downstream. Specifically, we showed that lift enhancement authority can be retained by positioning the actuators near the wing root and out of the path of the LEV. In some cases, a reciprocal effect of the actuator distribution on LEV dynamics was also observed. Figure 4.4 shows tuft visualizations over the $\Lambda = 45°$, $A_R = 3.2$ wing with 30° flap deflection. At $\alpha = 8°$, the LEV has just begun to form in

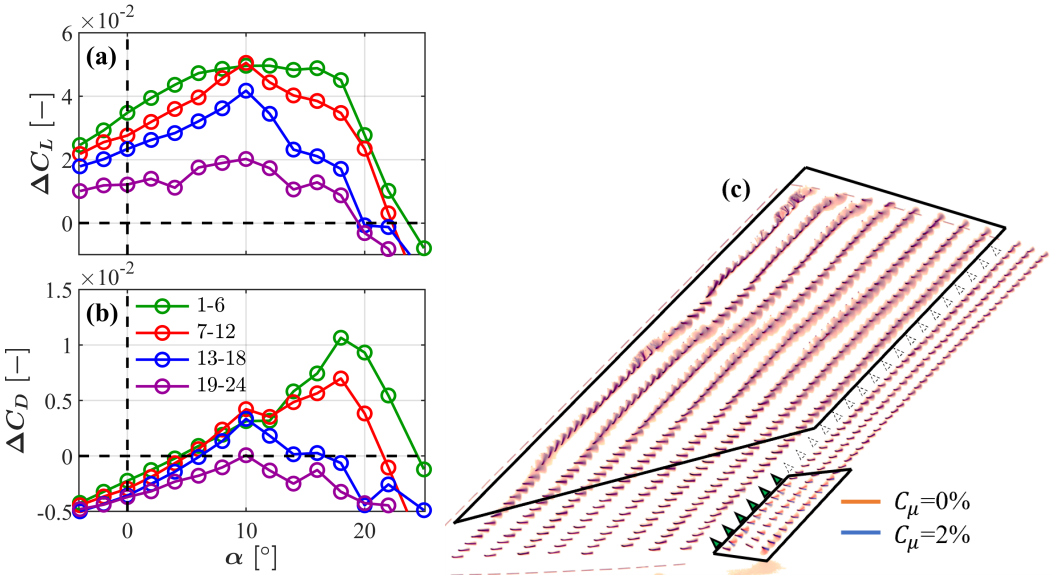

Figure 4.3: Effect of different spanwise actuation locations at C_μ = 2.0% on (a) lift and (b) drag of the $\Lambda = 45°$, $A_R = 2.3$, $\delta = 0°$ wing, and (c) tuft visualization of root actuation at $\alpha = 16°$.

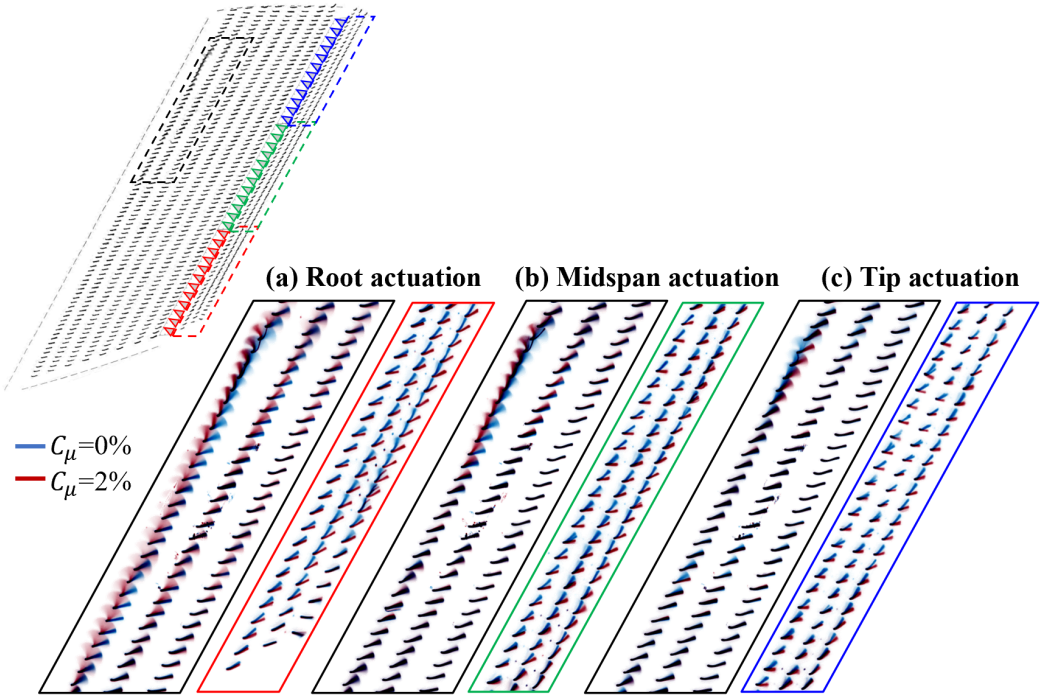

Figure 4.4: Tuft visualizations of the changes in LEV behavior with spanwise actuation location on the $\Lambda = 45°$, $A_R = 3.2$, $\alpha = 8°$, $\delta = 30°$ wing.

the region marked by dashed black lines in the top left diagram. In each sub-figure, zoomed-in views of superposed tuft images are shown when twelve actuators are

activated at $C_\mu = 2.0\%$ (a) the wing root, (b) mid-span, and (c) the wing tip. Tuft images over the corresponding region on the flap are also shown, marked by red, green, and blue dashed lines, respectively. Consistent with previous observations, each actuator distribution has a localized region of influence on the flap over which separated flow is re-attached to the flap surface and the spanwise velocity component is significantly mitigated.

However, altering the nature of the flow over the trailing edge in this way can also lead to global changes in pressure and circulation distribution over the wing. Large differences in the upstream LEV dynamics are observed between the three cases. The size of the vortex grows significantly with root actuation, grows slightly with midspan actuation, and shrinks with tip actuation. The change in size of the LEV also correlates with the effected increase in lift. These general trends are similar to those observed in Figure 4.3, even though A_R and δ were different.

This example not only demonstrates an important coupling between separation behaviors at the leading and trailing edges, but also highlights the potential for localized blowing to create global changes in the flow field. Future work should further investigate these interactions and explore the feasibility of simultaneous actuation at the leading and trailing edges.

4.3 Pitch control and stabilization

Another application of AFC is moment control, which can reduce the area of or all together eliminate tails and stabilizers on aircraft. In this section, we primarily focus on the control of pitching moment, specifically the elimination of unstable pitch departure on highly swept wings.

The effect of TE actuation on the pitching characteristics of the $\Lambda = 45°$, $A_R = 2.3$ wing is shown in Figure 4.5(a). The black curve plots C_L vs C_{LM} for the baseline case, and each subsequent colored curve corresponds to a fixed value of C_μ with all 24 available actuators active. We see that the curve shifts to the right as C_μ is increased, which means that AFC induces a negative (nose down) pitching moment on the wing. This is because blowing results in reduction of pressure due to entrainment. When this occurs on the suction side behind the MRP, the net effect pushes the nose down. Thus, this method of AFC can counteract the unstable pitch departure to maintain trimmed conditions across a wide range of C_L.

For a given wing geometry and actuator configuration, C_μ can be optimized such that C_{LM} remains zero as α is varied. Figure 4.5(b) shows such an optimization, where

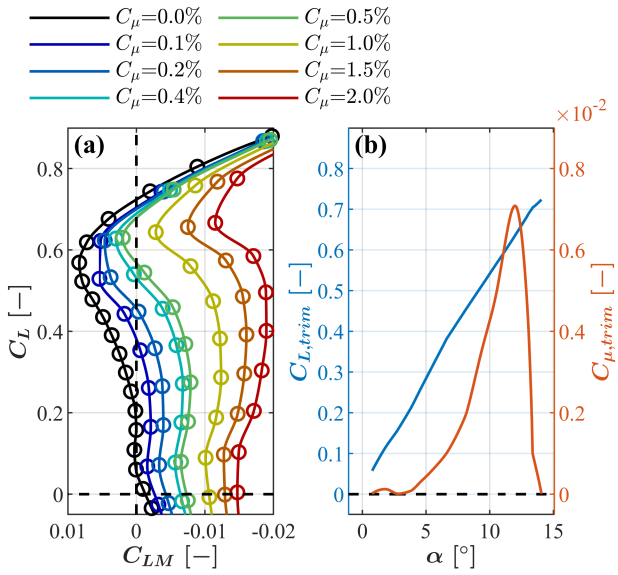

Figure 4.5: (a) Pitching moment curves of the $\Lambda = 45°$, $A_R = 2.3$ wing at different C_μ with all $n_j = 24$ actuators. (b) C_μ required at every α to maintain trim ($C_{LM} = 0$) and the resulting C_L.

$C_{\mu,trim}$ is the momentum input level required for trim and $C_{L,trim}$ is the resulting lift coefficient. The wing is naturally trimmed between $0.07 < C_L < 0.2$ because the MRP and AC coincide, so no AFC is required and $C_{\mu,trim} = 0$. Beyond $C_L = 0.2$, the wing undergoes pitch departure and $C_{\mu,trim}$ also increases accordingly. At the point of maximum instability which occurs at $\alpha = 11°$ ($C_L = 0.57$), $C_{\mu,trim} = 0.5\%$. At this point, the LEV forms and also begins to push the nose down. However, $C_{\mu,trim}$ continues to rise because the actuators' control authority is diminished by interacting with the LEV. Thus, the peak of the $C_{\mu,trim}$ curve is slightly shifted from that of the C_{LM} curve. Eventually, the effect of the LEV dominates and $C_{\mu,trim}$ falls sharply until AFC is no longer required. This is a powerful control method that increases the maximum achievable C_L from 0.2 to 0.73 without deflecting any control surfaces.

Since lift enhancement performance varied greatly by actuation location, we would expect the same for pitch control. The procedure for optimizing $C_{\mu,trim}$ is repeated for the same distributions of six actuators used in Figure 4.3, and the results are presented in Figure 4.6(a). Indeed, we see stark differences in the C_μ levels required to maintain trim over the same C_L range: root actuation requires up to $C_{\mu,trim} = 0.9\%$ but actuation near the midspan (Jets 7-12) can accomplish the same feat in less than 0.4%. Jets 13-18 slightly outperform Jets 7-12 over $8° < \alpha < 11°$.

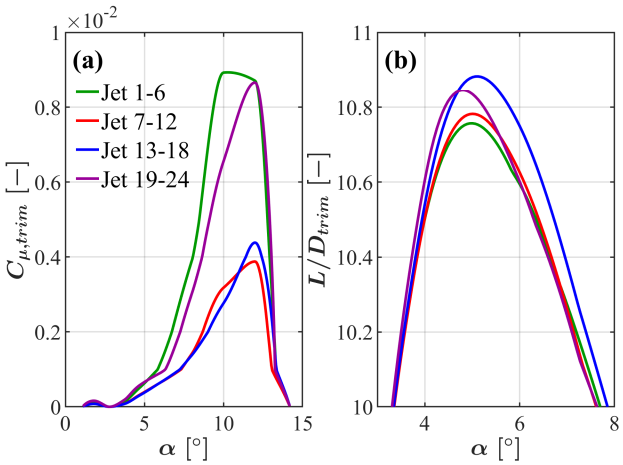

Figure 4.6: (a) $C_{\mu,trim}$ for different actuator distributions on the $\Lambda = 45°$, $A_R = 2.3$ wing, and (b) the resulting L/D at trim.

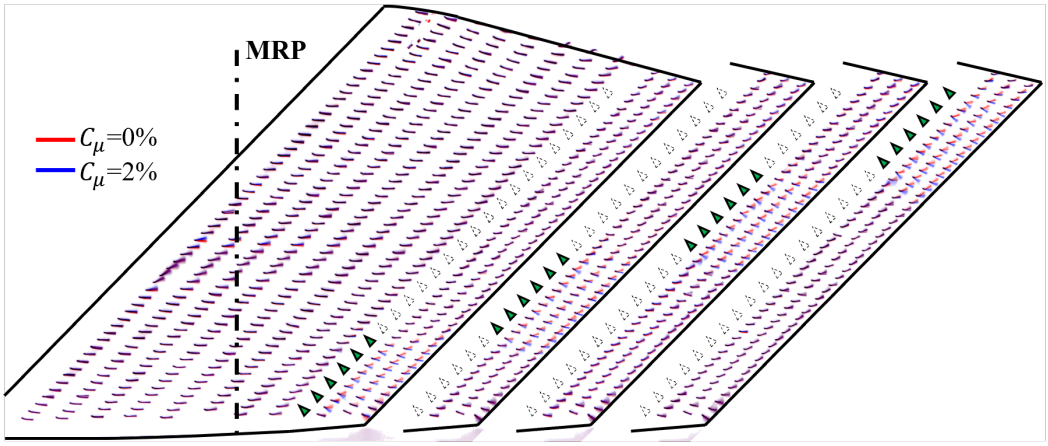

Figure 4.7: Tuft visualizations show the region of influence of each actuator distribution over the flow at the trailing edge. The MRP is indicated as a dashed black line.

Tuft visualizations at the trailing edge can provide some physical insight into this result. Figure 4.7 shows how the flow over the trailing edge is altered by $C_\mu = 2\%$ with the different sectional actuator distributions considered. Each set of actuators has a localized region of influence immediately downstream, where the outboard velocity component is suppressed. The size of these regions is approximately the same for all four distributions, but recall from Figure 4.3 that there is significant variance in the resulting magnitude of lift increment induced.

The fact that root actuation is least efficient in pitch control despite generating the largest increase in overall lift suggests that the lever arm is small. Indeed, the region

of influence of root actuation is closest to the MRP, whose location is indicated by a vertical dashed line.Another interesting observation is that the $C_{\mu,trim}$ for root actuation peaks at $\alpha = 10°$ as opposed to 12° for the other distributions. This may be due to the extra momentum needed to overcome the strong separation at the wing-wall juncture. On the other hand, tip actuation is also not very efficient for the opposite reason. Its region of influence has a large lever arm but the induced change in lift is much smaller. Quantitatively, the distance from the MRP is about three times larger than the root but interaction with the tip vortex reduces ΔC_L by more than half.

Concentrating the actuators near the middle of the wingspan strikes a good balance between the competing effects of lever arm and ΔC_L. Both Jets 7-12 and 13-18 require significantly less C_μ to maintain trimmed conditions. Jets 13-18 slightly outperform Jets 7-12 over $8° < \alpha < 11°$, and vice versa over $11° < \alpha < 14°$. The crossover in $C_{\mu,trim}$ that occurs at 11° may be due to interaction losses with the LEV. Jets 13-18 benefit from the slightly longer lever arm but are located directly in the path of the LEV at its inception.

Control of pitching moment is a complex balance between various flow interaction mechanisms that induce changes in lift and drag, as well as the lever arm with respect to the wing MRP. One way to account for all these effects is to look at the lift-to-drag ratio under trimmed conditions, as shown in Figure 4.6(b). Focusing on the low-α range near the peak of the L/D curve, Jets 13-18 emerge as the clear winner, requiring the least C_μ input for trim while simultaneously generating the highest L/D. Tip actuation (Jets 19-24) also provides high L/D due to its outstanding drag reduction capabilities, but it requires a much higher $C_{\mu,trim}$.

This optimization example truly showcases the beauty and necessity of considering AFC possibilities together with the wing design, as different control objectives call for different actuator distributions. This idea can be extended even further to the design of the entire aircraft system. Knowing that TE AFC can effectively counteract unstable pitch breaks, tails and stabilizers can be reduced in size or entirely removed. The wing can be intentionally designed to be highly unstable instead of opting for stability, for example by shifting the location of the aircraft center of gravity or inducing the LEV closer to the wing root. In doing so, even higher values of $C_{L,trim}$ can be attained.

Consider four different choices for MRP location on the same wing. The corresponding baseline pitching moment curves are shown in Figure 4.8(a). The black

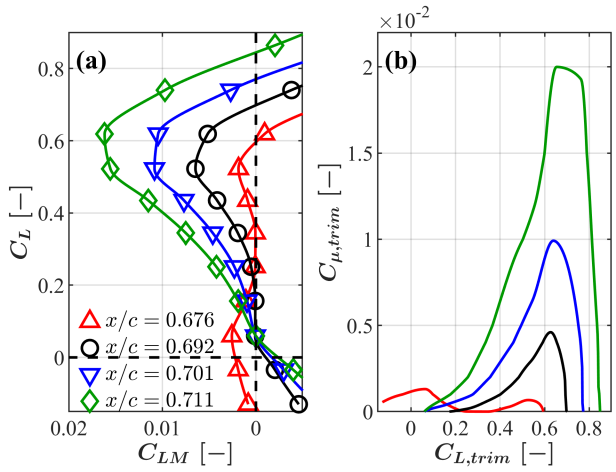

Figure 4.8: (a) Baseline pitching moment curve of the $\Lambda = 45°$, $A_R = 2.3$ wing as MRP is varied. (b) C_μ required to maintain trim using Jets 13-18 at the desired C_L. Values are provided in Table 4.1.

curve corresponds to the previously studied configurations in this section, in which the MRP is at $x/c = 0.692$ and the wing is naturally trimmed over $0 < C_L < 0.2$. To obtain the red curve, the MRP is shifted slightly upstream such that natural trim now occurs over $0.2 < C_L < 0.4$. This case was examined in Chapter 2. For the blue and green curves, the MRP is shifted downstream leading to highly unstable pitch behavior with no trimmed range. Note that these MRPs span only 3.5% of the chord, between $x/c = 0.676$ to 0.711 as given in Table 4.1, indicating that longitudinal behavior is highly sensitive to MRP location.

	x_{MRP}/c	$C_{LM,0}$	$C_{L,trim}$	$C_{\mu,trim}$ [%]
△	0.676	-0.0326	(-0.13,0.59)	0.13
○	0.692	-0.0292	(0.17,0.70)	0.46
▽	0.701	-0.0286	(0.06,0.77)	0.99
◇	0.711	-0.0279	(0.06,0.85)	2.00

Table 4.1: MRP location and trim offset applied to obtain each of the C_{LM} curves in Figure 4.8. Then, the C_L range over which the wing is trimmed and the maximum C_μ required to achieve trim are provided.

Now, activate Jets 13-18, which were demonstrated to be optimal for maintaining trim. The $C_{\mu,trim}$ required is plotted against the trimmed lift in Figure 4.8(b). Qualitatively, the shapes of these curves correlate well with those of (a) where $C_{LM} > 0$ because a larger C_{LM} generally requires more C_μ to counteract. For the red case, trim is maintained up to $C_L = 0.6$ using a maximum of only $C_\mu = 0.13\%$

and extends down to negative C_L values. If higher AFC flow rates are available, higher trimmed lift values can be achieved. With C_μ of 1% and 2%, C_L can be increased up to 0.77 and 0.85 respectively.

Having AFC on-demand can thus increase aircraft tolerance to shifts in its center of gravity. In-flight shifts may be small for large transport and passenger aircraft, but can become significant for smaller combat aircraft as it uses fuel or deploys weapons. This opens up new design trade-offs between various factors including but not limited to maneuverability, takeoff and landing speed, and payload capacity. An approach that integrates AFC into system-level design and is informed by physical understanding of the various flow interaction mechanisms can surpass previous design limitations.

We have successfully demonstrated that the longitudinal instability of a wing may be controlled with SJAs at $x/c = 0.8$ to significantly extend the C_L range over which trim may be maintained without control surface deflections. In fact, this range could be further extended by intentionally choosing a more unstable MRP, if the blowing resources are available. These investigations used many actuators ($n_j = 24$ for Figure 4.5 and $n_j = 6$ for Figures 4.6 & 4.8) for consistency with previous analyses for lift increment. These promising results beg the question: but what if on-board resources are limited? What is the absolute minimum input that is required to trim a wing with unstable pitch departure?

Figure 4.9(a) plots the effect of a single actuator at very low input of $C_\mu = 0.1\%$ on the pitching moment polar of the unstable ($\Lambda = 30^\circ$, $A_R = 3.8$) wing. The color of the curve corresponds to spanwise actuation location, with blue being closest to the wing root. The shaded gray region shows the uncertainty bound for the baseline curve ($C_\mu = 0\%$), corresponding to the maximum and minimum C_{LM} observed at every C_L across all the trials. In (b), the ΔC_{LM} curves are plotted.

The major conclusion is that with the right actuator placement, only $C_\mu = 0.1\%$ is needed to trim the wing all the way up to $C_L = 1.0$. With this choice of MRP, the wing is naturally trimmed over $0.2 \leq C_L \leq 0.4$ and requires no control, although the actuators at $\xi_s/b = 0.58$ and 0.60 generate the largest ΔC_{LM}. Between $0.4 \leq C_L \leq 0.8$, which is when C_{LM} is increasing, these actuators stabilize the wing most efficiently. However, as the baseline C_{LM} decreases over $0.8 \leq C_L \leq 0.95$, the optimum actuator location moves inboard to $\xi_s/b = 0.33$. This is because the initial actuators interact with the LEV upon its inception and therefore lose some control authority, as was visualized in Figure 4.3. Beyond $C_L = 0.95$, C_{LM} rapidly

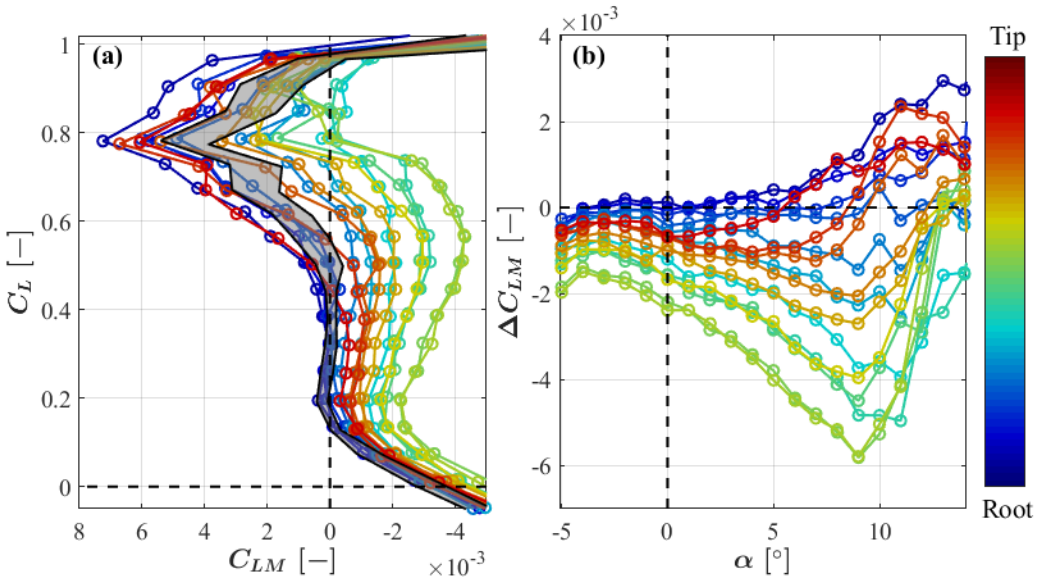

Figure 4.9: Effect of a single actuator activated at $C_\mu = 0.1\%$ at different spanwise locations on (a) pitching moment polar and (b) lift increment of the unstable $\Lambda = 30°$, $A_R = 3.8$ wing. The gray region corresponds to the uncertainty in the baseline curve across all tests.

decreases due to the growth of the LEV. However, some actuators near the root and tip of the wing are able to counteract this with a positive pitching moment over a small α range: a behavior that was not observed previously with 6 or more actuators. The actuator closest to the root ($\xi_s/b = 0.01$) induces a positive moment for $\alpha > 2°$, and the actuator closest to the tip ($\xi_s/b = 0.96$) for $\alpha > 5°$.

Could these actuators at the edges of the wing be used, then, to extend the trimmed range of a wing that undergoes stable pitch departure? The single-actuator experiment is repeated on the ($\Lambda = 30°$, $A_R = 2.6$) wing and the results are plotted in Figure 4.10. Similar to the other wing, there is an optimum location near the mid-span that most efficiently induces negative moment, although that is not the objective anymore. Note that this actuator, located at $\xi_s/b = 0.38$, is most efficient across the entire range plotted because the LEV does not form until much later. The root actuator ($\xi_s/b = 0.02$) and the tip actuator ($\xi_s/b = 0.94$) both induce $\Delta C_{LM} > 0$ at α above 8° and 5°, respectively. However, the TES is so strong that the effect is unfortunately not sufficient to restore trimmed conditions. Higher C_μ up to 2.0% were also tested (results not shown), which slightly increased the magnitude of ΔC_{LM} but still was not enough.

Perhaps the feat may be feasible if the actuators were shifted slightly upstream or

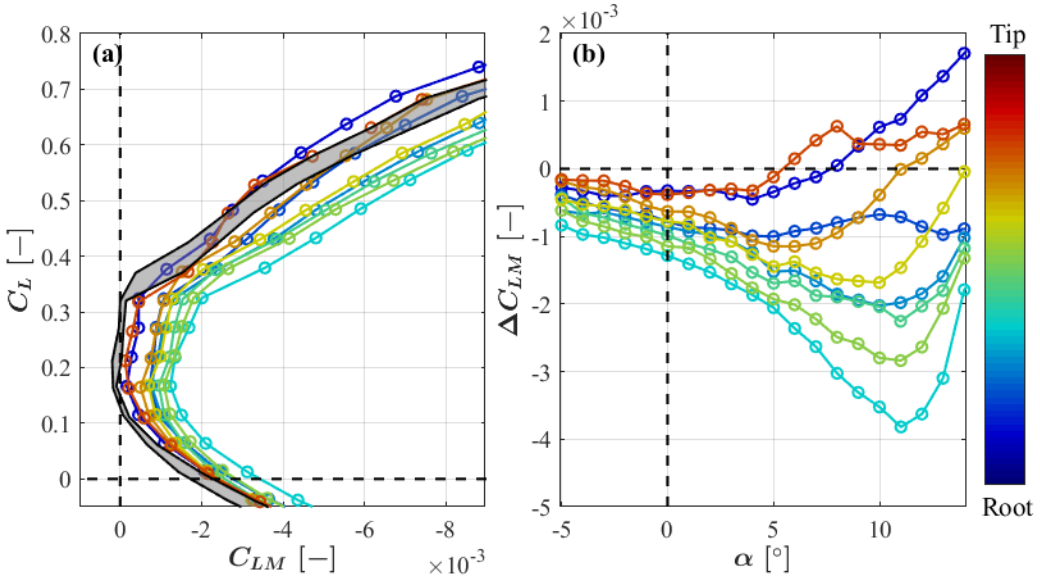

Figure 4.10: Effect of a single actuator activated at $C_\mu = 0.1\%$ at different spanwise locations on (a) pitching moment polar and (b) lift increment of the stable $\Lambda = 30°$, $A_R = 2.6$ wing. The gray region corresponds to the uncertainty in the baseline curve across all tests.

oriented at a different angle with respect to the flow. Further quantitative diagnostics are necessary to identify the exact interaction mechanisms occurring at the root and tip, and how the flow may be better altered to suit our control objectives.

Chapter 5

CONCLUDING REMARKS & FUTURE WORK

Sweeping jet actuators are considered the "rising stars" of active flow control and have received considerable attention recently from researchers in academia, industry, and government. The high sweeping angle of the jet enables efficient and effective flow control with just a few sparsely and strategically placed actuators. The spatial oscillation is fully self-initiated and sustained with a steady supply of pressurized air, and the absence of moving parts contributes to the technology's reliability and ease of installation on a vehicle.

A comprehensive subsonic wind tunnel testing campaign was performed on a swept wing model, covering a wide design space of wing shapes and spanwise actuator distributions. The aerodynamic performance changes effected by AFC were shown to be an intricate function of many independent variables, motivating reconsideration of the traditional approach which emphasizes the momentum coefficient C_μ. A new approach based on fluid power coefficients was developed, which offers data scaling abilities comparable to C_μ for 2D steady blowing configurations and seamless integration of AFC into the system design process for complex 3D configurations. Optimum actuation location was revealed to depend significantly on the control objective: blowing at the wing root proved effective for lift enhancement, mid-span for pitch stabilization, and tip for drag reduction. These results call for AFC to be considered in the high-level conceptual design of vehicles rather than an add-on feature to improve an existing design. For example, the AFC system on the recent *Boeing ecoDemonstrator* was retrofitted and thus relied on bleed air from an existing engine that needed to be cooled (Whalen, Spoor, et al., 2016). If the number of required actuators is small, installing separate compressors near each actuator may turn out to be more power-efficient and robust. An aircraft that is carefully optimized in conjunction with a suite of SJAs that can be activated as necessary during flight may lead to novel aircraft configurations.

Despite the diverse set of effects observed across the parameter space tested, unifying trends and mechanisms underlying the flow interactions were illuminated with the help of surface tuft visualizations. Wing sweep dictated the physics of the LEV, such as C_L of its inception, its strength relative to TES, and its relevance as a target for

flow control. These were all independent of aspect ratio. Lift increment due to SJAs was shown to consistently compete with that due to vortex lift, and the dominant effect varied with wing geometry. This interaction was summarized by a universal correlation between the spike in $\partial C_D/\partial\alpha$ due to LEV inception and decay in AFC lift enhancement ΔC_L. In pitching moment control, location of the SJA with respect to the wing's MRP (i.e., the lever arm) proved to be just as important as the magnitude of local changes in pressure distribution caused by blowing. Although much more about the 3D wing-AFC interactions remains to be understood, the fundamental flow physics insights accumulated in this study may provide some conceptual guidance for future aircraft designers.

A natural extension of this study is to implement actuators at the LE for direct and targeted control of the LEV. Although the model was designed so that blowing may occur simultaneously at $x/c = 0.01$, 0.1, and 0.8, Hirsch did not observe any combinatory effects between them and could not achieve significant lift augmentation using LE actuation (D.G. Hirsch, 2017). However, Figure 4.4 suggests a strong coupling between the LEV and TE blowing that warrants further investigation. The present study revealed the competing effects of lift enhancement due to AFC and vortex lift. Could the LEV propagation path be re-directed to avoid interfering with TE actuators? How would this affect the pitch characteristics of the wing? Drastic changes in drag were also observed before and after LEV inception. Can asymmetric treatment of the LEV across the two wings of an aircraft provide sufficient drag differences for yaw control, further eliminating the need for deflected control surfaces? Physical understanding of these flow interactions may then be extended to other wing shapes such as Delta and Lambda wings, which exhibit similar flow features.

Advanced quantitative diagnostics can be implemented on select configurations to dig deeper into the details of the flow field. A combination of balance measurements and tuft visualizations in this study enabled efficient coverage of a broad parameter space while still providing key insights about the underlying flow mechanisms. Techniques like particle image velocimetry or pressure-sensitive paint may not be feasible to implement for every case as they require extensive calibration and processing, but a few cases of interest can be identified. Comparing the size and circulation of the LEV on $\Lambda = 45°$ wings of different A_R (Figure 2.3) could reveal important requirement differences for actuator sizing. Knowledge of the surface pressure distribution during the vortex peel-off of unstable pitch departure (Figure

2.9(d)) could help optimize actuator placement and orientation.

Yet another avenue for future research is a simple extension of the geometric parameter space. This thesis covered an informative but limited set of Λ and A_R which are representative of existing transport and combat platforms that do not include AFC in the design loop. When AFC is considered from the outset, its behavior and performance on even more longitudinally unstable configurations or unconventional planform shapes would be interesting to explore. The effect of twist or taper along the wingspan, as well as the airfoil profile (e.g., camber and LE curvature) should be analyzed as they have been shown to impact LEV dynamics.

The concept of "on-demand" flow control is attractive and promising. A data-driven and physics-informed approach with AFC integrated into the early conceptual stages of design will be crucial in designing future aircraft where wings, control surfaces, and actuators operate in unison to exceed current aerodynamic performance limitations. Such a concept presents a complex optimization problem and a large departure from traditional design processes. This thesis represents a step toward that future by demonstrating an integrated power-based system analysis and illuminating some of the key flow interaction mechanisms on a simple swept wing.

Part II

Propellers with co-rotating shrouds

Chapter 6

INTRODUCTION

The propeller is the engineer's main tool for creating propulsive forces from continuous rotational motion. From airplane engines to the cooling fan at your home, they appear in many applications and with diverse geometric designs to optimize for specific performance requirements or operating Reynolds numbers. The concept can be traced back to screws in 4th century B.C. Greece, and became widely used first in marine applications in the 1800s and then for aircraft in the 1900s (Kasula, 2019). The *Wright Flyer*, which made the first sustained flight by a manned airplane in 1903, used a pair of counter-rotating propellers for forward propulsion. The *Vought-Sikorsky 300*, the world's first practical helicopter whose design used a single main rotor and smaller tail rotor, took flight in 1939. Since then, many advances have been made to the design and manufacturing methods to make propellers more efficient and lightweight.

Modifying the blade geometry, such as its airfoil profile, twist, taper, or diameter, is one means of improving the aerodynamic performance of a propeller. An alternative approach is to explore different configurations altogether—the ducted or shrouded propeller[1] is one such example. The propeller is surrounded by a stationary cylindrical "ring-wing" whose cross-section resembles an airfoil. The configuration was first investigated by (Stipa, 1932), whose airplane design consisted of a fuselage in the shape of a Venturi tube (Figure 6.1), and many more followed thereafter. Early works for these larger-scale aircraft are reviewed in (Sacks and Burnell, 1962) and more recent works in (Pereira, 2008; Zhang and Barakos, 2020).

Significant gains in aerodynamic performance compared to the unshrouded propeller have been demonstrated. The primary benefits are improved thrust and reduced power consumption during hover, but the shroud may also behave as an annular wing (Fletcher, 1957) to augment lift in forward flight. In addition, shrouds can help mitigate the noise footprint often associated with blade-vortex interactions (Chekab et al., 2013; Malgoezar et al., 2019) or increase the operational safety of the propeller. The enclosure prevents injury of ground personnel from the sharp blades.

[1]The terms "duct" and "shroud" are often used interchangeably in the literature. One arbitrary convention that is sometimes adopted differentiates the two based on whether its chord is longer than the blade chord, but in this thesis, we stick to "shroud".

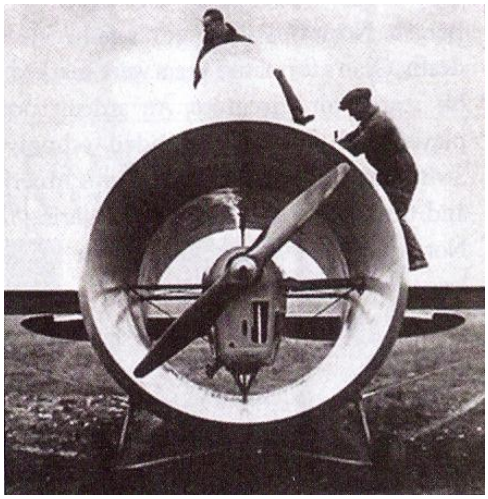

Figure 6.1: The Stipa-Caproni aircraft whose fuselage was an “intubed propeller” (Aviation History, 1932).

Propeller performance is also extremely sensitive to the balance and symmetry of the blades, so seemingly small damages due to debris can result in major accidents. When tail rotor failures constituted over 20% of mishaps in U.S. Army helicopter operations, a shrouded design was incorporated to improve overall aircraft safety (Clemmons, 1992).

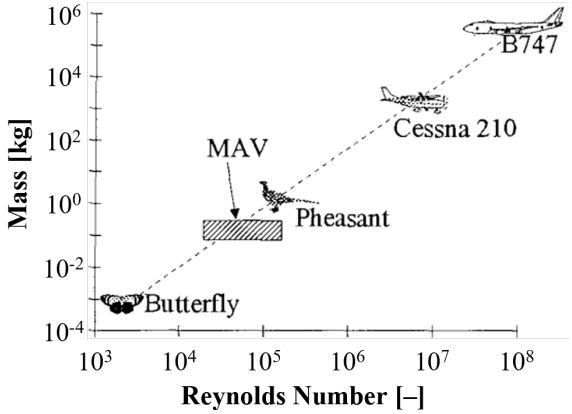

Figure 6.2: Reynolds number range for various flight vehicles, adapted from (Mueller, 1999).

The abovementioned benefits of a shrouded configuration are particularly desirable for micro-scale aerial vehicle (MAV) applications. The use of these aircraft continues to increase over a wide range of applications including recreation, surveillance, payload transport, and academic research, with some projections predicting up to

one billion units deployed around the world by 2030 (InsideRobotics, 2017). MAVs are often utilized in densely populated urban environments or covert surveillance missions that require quiet operation. They typically spend a significant portion of their mission in low-speed or hovering flight, which are inherently inefficient and power-hungry. This is further aggravated by the low operational Re due to their smaller scale. Since the Re regime lies in between that of insects and birds (Figure 6.2), many studies have looked into non-conventional airfoil shapes found in biological flyers (Tang, Viieru, and Shyy, 2007; Levy and Seifert, 2009). However, the lift-to-drag ratio of these airfoils is still substantially reduced compared to their high Re counterparts due to earlier separation and higher viscous effects.

Thus, the shrouded propeller configuration has emerged as a popular choice for many MAV applications with vertical take-off and landing (VTOL) capabilities (Hrishikeshavan, Black, and Chopra, 2014). However, their installation requires additional support structures and tight tolerances between the moving and stationary components. These drawbacks may be mitigated by attaching the shroud directly to the blade tips, using the blades themselves as the support structure. This creates a co-rotating "prop-shroud" system. The concept may not make sense at larger scales due to the high power input required to rotate the shroud, but may be feasible for MAVS especially when manufactured from lightweight materials.

6.1 Objectives

In Part II of this thesis, the performance of propellers with and without shrouds is investigated. The feasibility of a propeller concept with co-rotating shroud is explored through thrust and torque measurements in air, and the underlying flow physics is analyzed through particle visualization techniques in water. The objectives are to:

- demonstrate the potential of the "prop-shroud" concept to outperform off-the-shelf unshrouded drone propellers,
- understand the effect of the shroud on the time-averaged velocity and vorticity distributions during steady state, and
- develop a model of the propeller starting vortex based on vortex ring formation time.

The next section of this Introduction chapter describes the integrated test stand and water tank setups. Then, Chapter 7 corroborates the feasibility of this technology by systematically comparing its hover efficiency to the shroudless and stationary shroud configurations. Rather than undertaking a comprehensive optimization however (like the approach taken in Part I with AFC), the emphasis is then shifted to quantitative flow field characterization and fundamental understanding. Chapter 8 analyzes the effect of the rotating shroud on time- and phase-averaged flow features during steady-state propeller operation, and Chapter 9 tackles the unsteady vortex dynamics of propeller start-up. Implications on broader MAV design considerations such as acoustic noise and rotor-rotor interactions are discussed, and directions for future work are proposed in Chapter 10.

6.2 Experimental Setup

The "prop-shroud" geometry is shown in Figure 6.3, along with definitions of some important geometrical parameters that were varied in this study. The overall geometry was kept simple so that the focus of the study is placed on the understanding of flow physics rather than the optimization of performance. The isometric view in (a) shows clearly that the tip of each blade directly attaches to the inside surface of the shroud, unlike conventional shrouds that require a small blade tip clearance to allow the blade to rotate with respect to the stationary shroud. In practice, the juncture may be filleted or smoothed. The front view in (b) shows three blades spaced evenly (i.e., 120° apart). The chord length of the blade is constant at $c = 15$ mm except the inner 20 mm near the root where it tapers linearly to accommodate for the diameter of the hub. In (c), a cross-sectional slice through the rotational axis shows that the blade is untwisted (constant α along its span). Both the blade and the shroud use standard four-digit NACA airfoil profiles. Their trailing edges are slightly rounded due to resolution limitations on the 3D printer. The pitch angle α of the blade is defined with respect to the plane of rotation, and the angle β of the shroud is defined with respect to the axis of rotation. Blade diameter is held constant at $D_p = 101.6$ mm for the results presented.

A *T-Motor F-80* 2200kV brushless DC motor is used to spin the propellers. The motor is powered by a constant voltage of 14.8 V, which corresponds to four LiPo battery cells commonly used in small-scale drone applications. Pulse-width modulation (PWM) signals are sent from an Arduino to an electronic speed controller (ESC) to operate the motor.

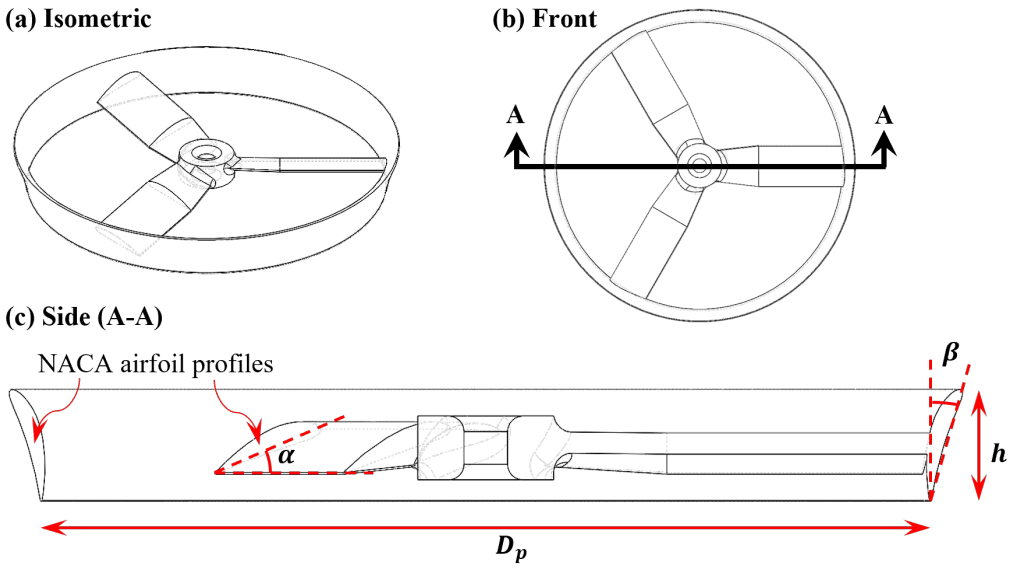

Figure 6.3: (a) Isometric, (b) front, and (c) cross-sectional views of the "prop-shroud" geometry.

In air, the *Series 1580* integrated test stand from *RC Benchmark* (now *Tyto Robotics*) records the thrust and torque generated, as well as the rotation rate and electrical power consumption of the motor. This experimental setup is shown in Figure 6.4. The prop-shroud is mounted to the motor, which in turn is secured to a vertical plate. The propeller is oriented to blow away from the test stand so that its wake is undisturbed. Blockage effects at the intake are assumed to be small.

A stationary shroud is also designed to attach to the mounting plate, to be tested with an unshrouded "baseline" propeller. Different views of the design are shown in Figure 6.5. Four struts, evenly spaced 90° apart, are used to hold the shroud concentrically to the motor. The width of these struts are kept to a minimum without jeopardizing structural integrity to reduce its aerodynamic footprint. A blade tip clearance of approximately 1mm, visible in (b) and (c), enables the propeller to rotate freely even in the presence of small vibrations from the motor and the test stand. The stationary shroud is 3D-printed in a single part using the same procedures as the prop-shroud, which will be explained in further detail in Chapter 7. Note that any aerodynamic forces or moments on the shroud would be included in the measured thrust and torque.

An entirely different test rig is designed and assembled for experiments in water. A 0.91 m × 0.91 m × 2.13 m tank of water, shown in Figure 6.6(a), is seeded with neutrally buoyant silver-coated glass particles of 90-106 μm diameter. A 532 nm

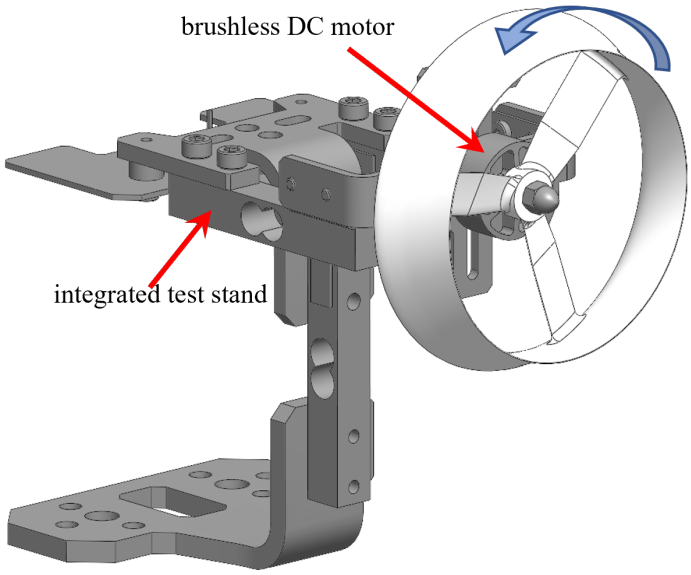

Figure 6.4: Experimental setup in air showing the prop-shroud mounted to the integrated *RC Benchmark* test stand.

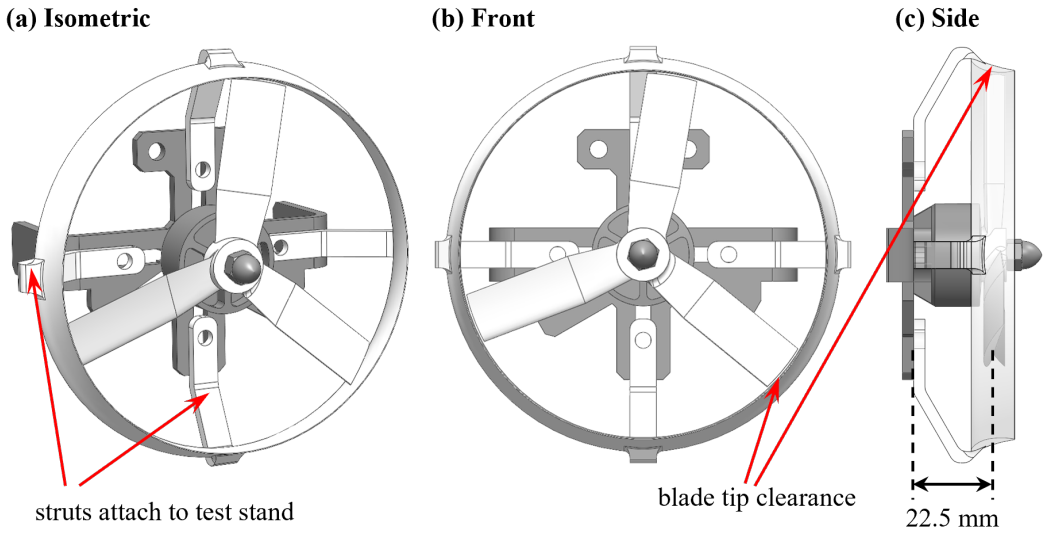

Figure 6.5: (a) Isometric, (b) front, and (c) transparent side views of the stationary shroud mounted to the test stand.

(green) continuous 4 W laser with beam diameter of 2.5 mm is split into a sheet to illuminate a plane from below. An IDT XSM-3520 high-speed camera is used to capture a field of view of up to 54 cm × 30 cm (shown by dashed red rectangle) at 1000 frames per second. A propeller test rig assembly is inserted into the water from above, as shown in zoomed-in view (b). A single-axis load cell, which remains above the water surface, measures the thrust produced. An *Emax 2213* motor with 935 kV

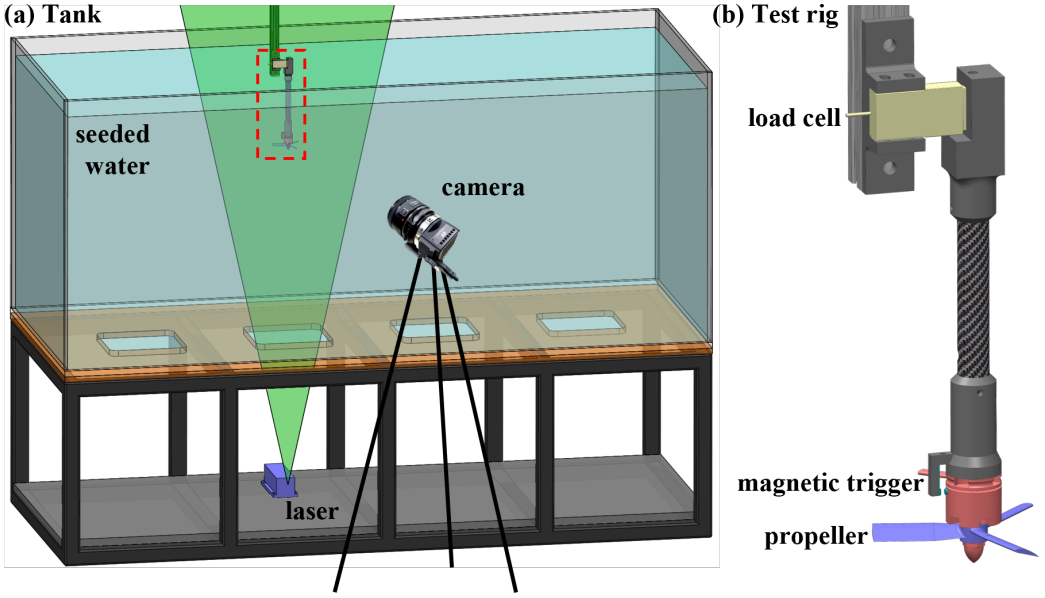

Figure 6.6: Experimental setup in water showing (a) the flow visualization components and (b) a zoomed-in view of the propeller test rig.

rating replaces the motor used in air because it has a smaller diameter footprint and produces higher torques. The motor is mounted at the end of a cylindrical cantilever comprised of a 16 mm diameter carbon-fiber tube and 3D-printed attachment parts. The streamlined design minimizes interference with the intake flow. A Hall effect sensor detects a small magnet placed on the motor to trigger the camera and capture phase-locked images.

Chapter 7

COMPARISONS OF HOVER PERFORMANCE IN AIR

Aircraft wings can be largely classified into three categories based on the lift-generation mechanism: fixed, flapping, and rotating. Fixed wings are most commonly seen in long-range aircraft with high payloads, such as commercial airliners or military bombers, since conventional airfoils used in these applications can achieve high L/D at high Re. However, they require a separate engine for forward propulsion and a long runway for takeoff, since lift is only generated through the passage of flow over the wing which is fixed with respect to the main body. Thus, fixed-wing configurations are unable to hover in a single position, but can only loiter at low speeds in large open spaces. Flapping wings are commonly encountered in natural flight, such as that of birds and insects. High-frequency flapping enables efficient hovering with high precision and stability at small length scales (Taha et al., 2020), but are not scalable to carry large payloads over long distances. Complex mechanical actuation systems required to produce the flapping motion are costly to implement and therefore difficult to justify in most practical applications.

Rotating wings currently provide the most efficient hovering and low-speed maneuvering capabilities for aircraft, and also enable vertical takeoff and landing from restricted or congested areas. However, these flight states, which comprise a significant proportion of typical MAV missions, have inherently high power consumption. While battery technology is continuously evolving to have higher energy density, faster charging, and longer life cycles (Yang et al., 2021), range and payload are still limited. Thus, the discovery of new rotating wing designs and concepts that can hover efficiently is of high interest to the MAV community.

An aircraft is in hover when its body remains in one place in the air, with no translational or rotational motion. In actual flight, this implies that the net external forces and torques are zero: the weight of the vehicle is balanced by the vertical thrust produced, torques from rotation components are canceled (e.g., through a tail rotor on a helicopter or counter-rotating propellers on a multicopter), and any other factors such as wind conditions and ground effects are accounted for. In a laboratory setting, the problem is simplified to a rotating propeller fixed in place and tested in quiescent fluid. Typically, a propeller design is initially placed far away from other

objects to isolate its performance from other effects, but may also be tested in the vicinity of obstacles to better simulate congested urban environments.

This chapter compares the hover performance in air of isolated propellers with stationary and co-rotating shrouds of various sizes and cross-sectional profiles. Measures of efficiency commonly found in the literature based on measured thrust, torque, and rotation rate are used. The main objective is to demonstrate the feasibility and promise of the "prop-shroud" configuration, without performing an extensive parameter sweep or optimization.

7.1 Validation of prototyping methodology

Additive manufacturing (i.e., 3D printing) technology is leveraged to rapidly prototype and test different geometries. After some trial and error, it was found that using the Rigid 10K resin material on the *Formlabs Form 3* printer worked best. Prototypes made using other material/printer combinations were too flexible, deformed significantly during the curing process, did not produce the desired surface finish, or fractured at high rotation rates. A protocol was ultimately developed for printing, washing, curing, and surface polishing to maintain consistency between different prototypes. Figure 7.1 shows an off-the-shelf propeller for miniature drones and a 3D-printed propeller with a NACA 6416 cross-sectional blade profile, both with the same diameter of $D_p = 101.6$ mm.

The exact geometry of the commercial propeller is not available, but is typically optimized to maintain constant efficiency metrics across a wide operational range. Thus, the blade has a non-constant twist and taper along its span. It is made from a lightweight plastic and utilizes a much thinner airfoil with sharp trailing edge for its blade section profile (maximum thickness 1.8 mm, chord 16.2 mm). The 3D-printed propellers, on the other hand, require a thicker airfoil due to printing resolution and tensile strength for testing at higher Ω.

To characterize the hover performance of a propeller in air, thrust $\mathcal{T}$ and torque Q are measured as a function of rotation rate Ω on the integrated test stand setup. These can then be reported as dimensionless thrust and torque coefficients:

$$k_{\mathcal{T}} = \frac{\mathcal{T}}{\rho_\infty \Omega^2 D_p^4} \tag{7.1}$$

$$k_Q = \frac{Q}{\rho_\infty \Omega^2 D_p^5} \tag{7.2}$$

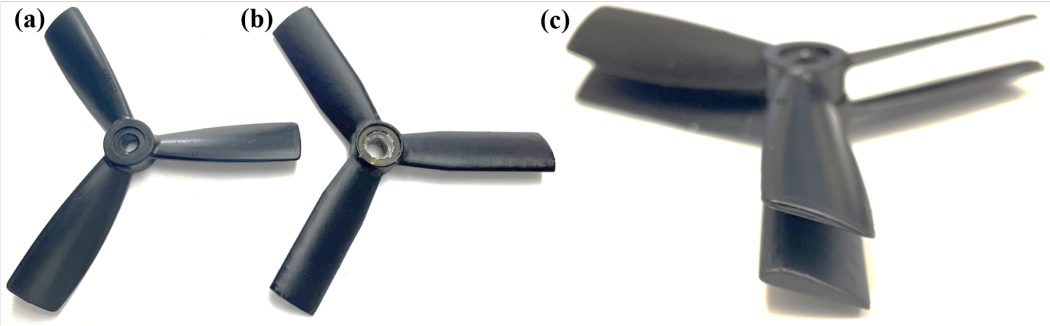

Figure 7.1: (a) Commercially available propeller for small-scale multicopters and (b) 3D-printed propeller with the same diameter. Their airfoil thicknesses are compared in (c).

computed pointwise for each measurement or as a single aggregate value using a quadratic curve fit. Metrics of hover efficiency are also often reported in the literature. The efficiency $\eta = k_{\mathcal{T}}/k_Q$ is the simple ratio of thrust produced per power input. The figure of merit FM is the ratio of the ideal power generated to the actual power input. Ideal power is the product of thrust and induced velocity computed from actuator disk momentum theory (Johnson, 1980), whereas actual power is the product of torque and rotation rate. Algebraic manipulation yields

$$FM = \frac{P_{ideal}}{P_{actual}} = \frac{\mathcal{T} v_i}{Q\Omega} = \sqrt{\frac{2}{\pi}} \frac{k_{\mathcal{T}}^{3/2}}{k_Q} \tag{7.3}$$

The first step is to validate the prototyping process by demonstrating that the performance of 3D-printed propellers is comparable to commercially available ones. The thrust and torque curves of three propeller designs are compared in Figure 7.2(a) & (b), averaged over five trials. The propeller corresponding to the red curve has a NACA 6416 profile with pitch angle $\alpha = 20°$, and the propeller corresponding to the blue curve has a NACA 9416 profile (slightly more camber) with $\alpha = 15°$. A quadratic curve $y = ax^2 + bx + c$ forced to have zero y-intercept and slope ($b = c = 0$) is fit to each dataset, plotted as dashed lines. The quadratic coefficient a is then related to the aggregate $k_{\mathcal{T}}$ and k_Q, reported in Table 7.1. Efficiency and figure of merit are also reported in (c), (d), and Table 7.1.

All three propellers exhibit a nice quadratic increase in $\mathcal{T}$ and Q with Ω. For a given Ω, the 3D-printed propellers produce less thrust than the commercial propeller but also require less torque. Thus, the 3D-printed propeller with the NACA 6416 profile actually has a higher $k_{\mathcal{T}}/k_Q$ ratio over the entire range tested. The propeller with NACA 9416 profile also outperforms the commercial propeller at $\mathcal{T} > 1$ N. The

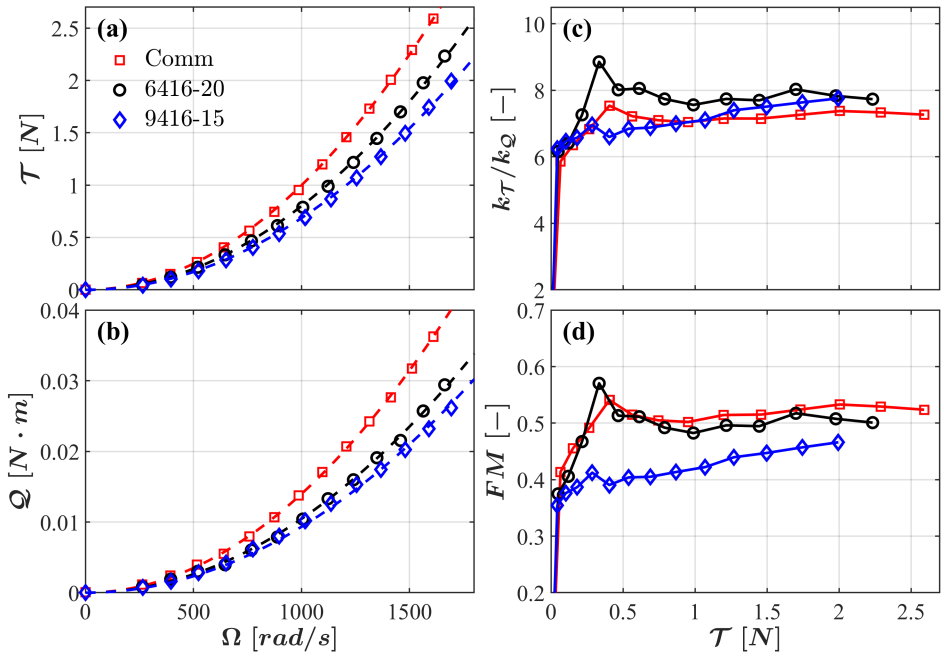

Figure 7.2: Hover performance of two 3D-printed propellers compared with an off-the-shelf propeller of the same diameter. (a) Thrust, (b) torque, (c) efficiency, and (d) figure of merit.

	$k_\mathcal{T}(10^{-3})$	$k_\mathcal{Q}(10^{-3})$	$k_\mathcal{T}/k_\mathcal{Q}$	FM
Comm	8.150	1.122	7.263	0.523
6416-20	6.525	0.839	7.782	0.502
9416-15	5.591	0.749	7.465	0.445

Table 7.1: Aggregate performance metrics of the propellers tested in Figure 7.2 based on a quadratic fit of the thrust and torque data.

figure of merit in (d), however, shows a slightly different trend. Under this metric, the commercial propeller is most efficient at hover, although the performance of the NACA 6416 propeller is very comparable, with their aggregate FM value differing only by 4%.

Based on these results, we conclude that the performance of the 3D-printed propellers with simple blade geometries are comparable to off-the-shelf propellers for small-scale drone applications, and thus validate the prototyping process.

7.2 Shroud geometry comparisons

With the prototyping methodology validated, we proceed to a systematic parametric study of the shroud geometry. The "baseline" blade geometry is fixed for all further

tests, and is selected to be NACA 6416 profile, $\alpha = 20°$, $c = 12.7$ mm, and $D_p = 101.6$ mm. We first ask how the hover performance changes in the presence of stationary and co-rotating shrouds. In Figure 7.3, shrouds sharing the same NACA 9415 profile at $\beta = 15°$ are tested at different h. The baseline (unshrouded) propeller is shown in black. The same hover performance metrics as those in Figure 7.2 are used.

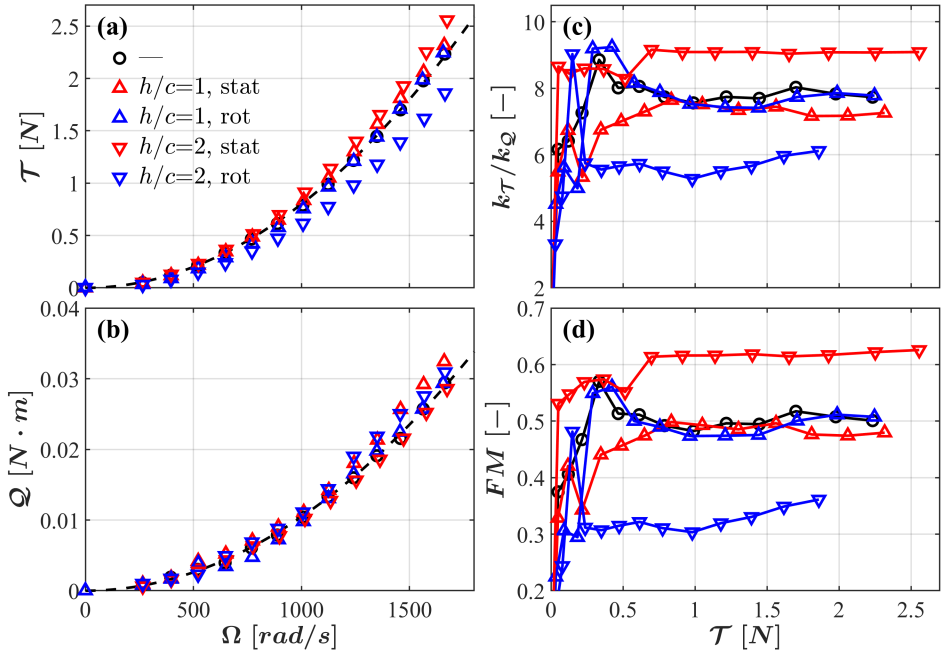

Figure 7.3: Comparisons of stationary and rotating shrouds for different shroud lengths h. The same hover performance metrics as those in Figure 7.2 are used.

With a conventional stationary shroud of $h/c = 2$, the thrust generated increases while torque required decreases for a given Ω. This significantly increases both $k_\mathcal{T}/k_\mathcal{Q}$ and FM, confirming the aerodynamic benefits of shrouding a propeller. On the other hand, when this large shroud is now made to co-rotate with the propeller, the opposite effect occurs. The thrust decreases while the torque increases, resulting in large penalties on the efficiency. Not only does it cost extra energy input to rotate an object with such high moment of inertia, but it seems that the shroud introduces strong undesired swirl to the flow, reducing the axial momentum and therefore the thrust generated. In this case, any small deviations in the axisymmetry of the shroud may exacerbate the effect. The sudden break in the torque curve (blue $\triangle$) observed around $\Omega = 1200$ rad/s may be due to this, although further experiments would be required to confirm.

When h/c is reduced to 1, the effect on performance is less noticeable. With the stationary shroud (red ∇), thrust increases slightly but torque is also increased, ultimately causing a slight decrease in $k_{\mathcal{T}}/k_{\mathcal{Q}}$ and FM from the baseline case. The increase in torque may be due to the blade-tip clearance being too large or the shroud being too short for vortex suppression. The rotating shroud performs almost identically, within experimental error, to the baseline propeller. This is interesting because the additional rotational inertia due to the shroud did not increase the required torque at given Ω, but the thrust

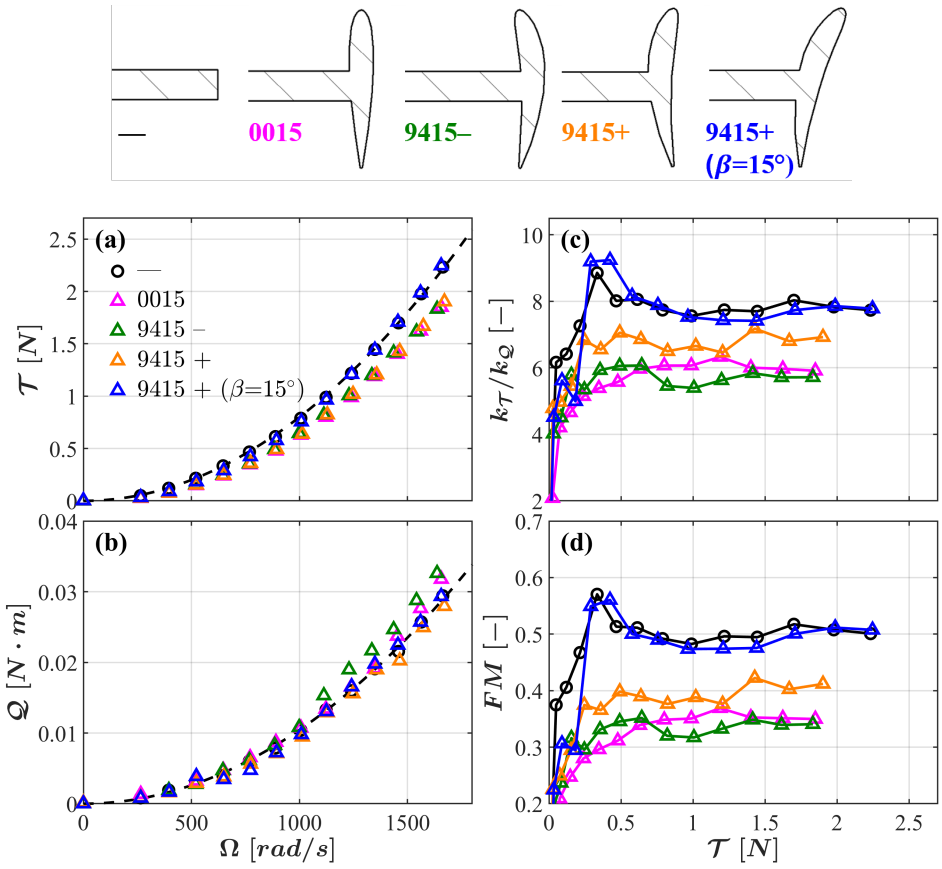

Figure 7.4: Comparison of different rotating shroud profiles for $h/c = 1$, using the same hover performance metrics as those in Figure 7.2.

We proceed to explore the effect of shroud profile shape. Four profiles, shown at the top of Figure 7.4, were tested. The last two digits of a four-digit NACA airfoil series specify the thickness-to-chord ratio (AirfoilTools, 2022), so all tested profiles share the same $t/c = 0.15$. The 0015 profile is symmetric, and the others are different orientations of the 9415 cambered profile. The NACA 9415 profile at $\beta = 15°$, shown previously, performed the best. All other designs had a detrimental effect on

the thrust produced.

The hover performance tests presented in this section proved that the prop-shroud concept is promising for MAV applications, especially with proper optimization of its geometry and material. The required power can be reduced by using more lightweight material with better manufacturing methods, and improvements to thrust and torque performance can be expected with further understanding of the underlying fluid dynamics. This thesis will focus on the latter, rather than performing a comprehensive parameter sweep and preparing an optimized application-ready product. In the next chapter, we employ qualitative and quantitative flow visualization techniques to dive deeper into the flow details of three select configurations: the "baseline" (unshrouded) propeller, propeller with "symmetric shroud" (NACA 0015, $h/c = 1$, $\beta = 0°$), and propeller with "cambered shroud" (NACA 9415, $h/c = 1$, $\beta = 15°$).

Chapter 8

EFFECT ON THE STEADY-STATE WAKE

Having analyzed the hover performance of various prop-shroud geometries in air to prove concept feasibility, we proceed to further understand and characterize the effect of the rotating shroud on the flow field. This chapter focuses on time- or phase-averaged features of the jet that is produced during steady-state operation of the propeller in a large quiescent tank of water.

As experiments are transferred from air to water, care is taken to match the Reynolds number range tested. The tip Reynolds number,

$$Re = \frac{u_{tip}c}{\nu} = \frac{\Omega D_p c}{2\nu} \tag{8.1}$$

in the hover tests were up to 8×10^5. Using the same set of 3D-printed propellers with $D_p = 101.6$ mm, lower Ω accounted for the decrease in kinematic viscosity ν. Visualizations in the water tank were performed at up to $Re = 5{\times}10^5$. Unfortunately, compressibility effects are highly reduced in water and the Mach number cannot simultaneously be matched to achieve complete dynamic similarity. Nevertheless, reduced flow speeds and availability of highly reflective tracer particles enable flow visualization at improved spatial and temporal resolution.

DPIV analysis shows that the presence of the rotating shroud increases the induced intake velocity in both the streamwise and radial directions. It also mitigates flow contraction and blade tip vortices in the near wake. The inner jet core is distinguished clearly from the outer tip vortex region by sign of vorticity, which will aid in the analysis of unsteady dynamics in the subsequent chapter.

8.1 Time-averaged velocity and vorticity fields

Digital particle image velocimetry (DPIV) is performed in a water tank to obtain a 2D streamwise slice of the velocity field through the axis of rotation. Neutrally buoyant, silver-coated glass particles of 93-106 μm diameter are used as tracer particles. The particles, illuminated by a green laser sheet, are imaged at 1000 frames per second ($\Delta t = 1$ ms) by a high-speed camera at 2560 px $\times$ 1440 px resolution. A Nikon lens with 50 mm fixed focal length is used to achieve the proper magnifications for the working distances allowable by the water tank facility. The

field of view (FOV) is adjusted and re-calibrated for each application to maximize the resolution of the flow features of interest.

Cross-correlation analysis is performed on consecutive image pairs in PIVlab (Stamhuis and Videler, 1995), an open-source platform in Matlab for PIV. For each trial, a mask is generated from the average-intensity image of all frames in the trial, which blurs out the particles and leaves only the outline of the solid boundaries. Some pre-processing of images, such as histogram equalization, high-pass filtering, and contrast stretching are applied to enhance correlation performance. The main algorithm is based on FFT window deformation and interrogates sub-windows of the image in two passes, fitting a Gaussian to provide sub-pixel estimates of the particle displacements. The first pass considers sub-windows with 64 px side length at a step size of 32 px, and the second pass considers sub-windows with 32 px side length at a step size of 16 px, resulting in a final flow field with 159 x 89 velocity measurements. Calibrations are applied to convert velocity units from px/frame to m/s. Results for each trial are averaged over 500 image pairs.

Figure 8.1(a) depicts the velocity field surrounding the baseline propeller at Ω = 53 rad/s. x and y are plotted on the same scale and normalized by the propeller diameter D_p. The origin lies at the center of the propeller. Arrows indicate the direction and magnitude of the local velocity vector at a coarse resolution to outline the overall flow pattern, and the heatmap presents the velocity magnitude at higher resolution. The gray region represents the mask, corresponding to the motor-propeller assembly mounted at the end of a cantilever. The velocity inside this region is set to be zero.

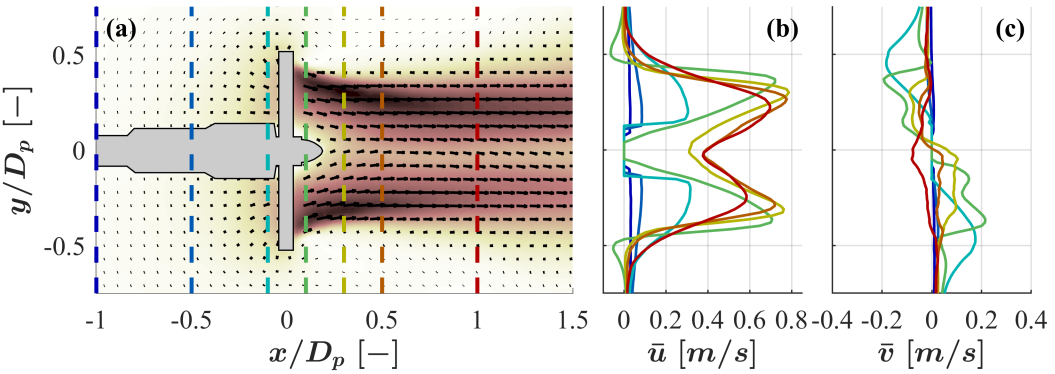

Figure 8.1: Time-averaged velocity field around the baseline propeller at Ω = 53 rad/s. (a) 2D velocity field showing both magnitude and direction, and (b,c) profiles of horizontal & vertical velocity component at select streamwise locations corresponding to the color of the dashed line in (a).

Profiles of the horizontal component profile $\bar{u}(y)$ and vertical component profile $\bar{v}(y)$ at seven select streamwise locations are plotted in Figure 8.1(b) & (c), respectively. Each streamwise station is indicated by a dashed line in (a) whose color corresponds to the profile curves; e.g., the dark blue and dark red curves correspond to profiles at $x/D_p = -1$ and 1, respectively. Overall, the time-averaged flow looks quite symmetric about the centerline, although some asymmetry becomes apparent beyond $x/D_p > 1$ most likely due to both experimental error and 3D effects.

Sufficiently far upstream of the propeller at $x/D_p = -1$, a slow and relatively uniform flow of about 0.03 m/s is induced. The flow is smoothly accelerated, and by $x/D_p = -0.5$, the inner region contained within the propeller's disk area ($-0.5 < y/D_p < 0.5$) has an observably higher velocity than the outer region. This difference is magnified as we move further downstream, and at the intake $x/D_p = -0.1$, a maximum $\bar{u}$ of 0.3 m/s is reached toward the center which rapidly decreases to zero as we move radially outward. At this point, there is also a significant vertical velocity component $\bar{v}$ that implies flow entrainment from the outer region as well.

Immediately downstream of the propeller at $x/D_p = 0.1$, the maximum $\bar{u}$ reaches 0.7 m/s, indicating a rapid acceleration of the flow as it passes through the propeller. This peak in the profile occurs at $y/D_p = 0.36$, slightly inboard of the blade tip. As we move further down the wake to $x/D_p = 0.3$ and 0.5, maximum $\bar{u}$ increases and moves inward. The jet thus contracts and continues to accelerate. The "void" along the centerline is somewhat filled in due to this contraction, as $\bar{u}$ rises to 0.4 m/s. By $x/D_p = 1$, the jet shows some decay most likely due to dissipation.

The same analysis is performed on a propeller with co-rotating symmetric shroud, shown in Figure 8.2. The addition of this shroud causes significant changes to the flow field, both quantitatively and qualitatively. The overall velocity field in (a) shows much higher intake speeds, reduced contraction in the near wake, and faster decay in the wake.

Let us look more closely at the $\bar{u}$ and $\bar{v}$ profiles at different streamwise stations. Far upstream at $x/D_p = -1$, the incoming flow is still relatively uniform. The shroud causes the flow to accelerate to higher speeds, reach a maximum $\bar{u}$ of 0.42 m/s at the inlet, which is 36% higher than the baseline case. The $\bar{v}$ component at the inlet also rises to 0.4 m/s near the blade tip, suggesting a much stronger radial entrainment from the outer region. Although the maximum $\bar{u}$ reached at $x/D_p = 0.1$ is approximately the same, the jet neither contracts nor accelerates in

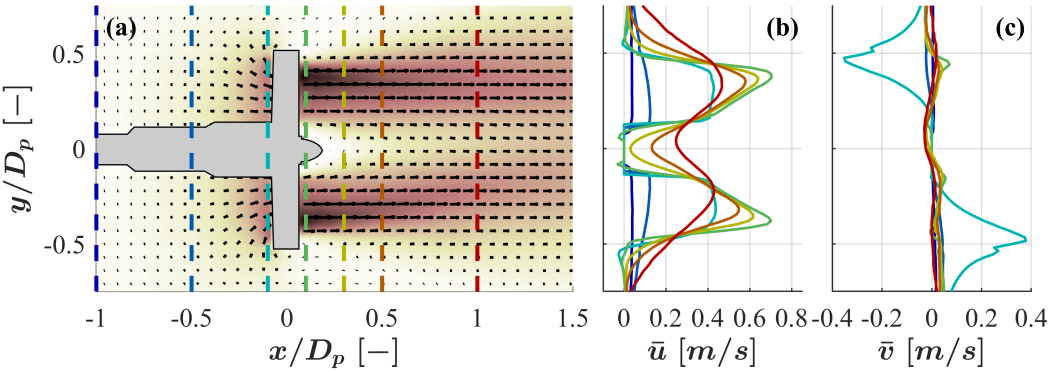

Figure 8.2: Time-averaged velocity field around the propeller with symmetric shroud at $\Omega = 53$ rad/s.

the wake. Thus, as we move to $x/D_p = 0.3$ and 0.5, the peak does not shift inward and steadily decreases. Consequently, the void region along the centerline remains as well, which is evident from the low value of the trough. Thus, the near-wake jet profile produced by a shrouded propeller more closely resembles an annulus.

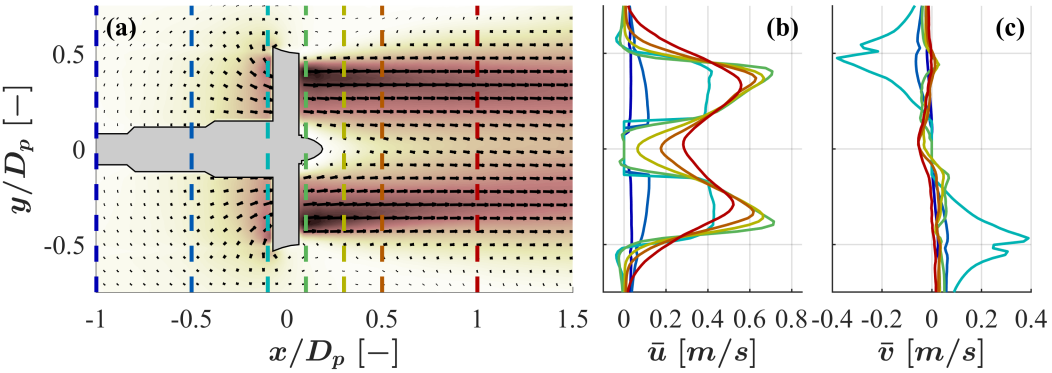

Figure 8.3: Time-averaged velocity field around the propeller with cambered shroud at $\Omega = 53$ rad/s.

Finally, the case with cambered shroud is presented in Figure 8.3. The profiles exhibit similar trends to the symmetric shroud, with the most notable difference being the slower decay of the jet in the wake. At $x/D_p = 1$, the peaks in $\bar{u}$ are higher for the cambered shroud than for the symmetric shroud. There are also slight differences in the $\bar{v}$ profile at the inlet near the tip ($x/D_p = -0.1$, $y/D_p = 0.5$) due to the change in shroud profile. The increased camber and β slightly increase the radial entrainment.

We wish to model the thrust generated by the propeller from the measured velocity profile. Assuming incompressible axisymmetric flow, the streamwise velocity

component $u = u(r;x)$ is integrated in cylindrical coordinates to obtain the jet momentum at different streamwise locations:

$$\begin{aligned} J(x) &= \int_{A(x)} \rho u^2(r;x)\ dA \\ &= \rho \int_0^\infty u^2(r;x)(2\pi r\ dr) \\ &= 2\pi\rho \int_0^\infty r u^2(r;x) dr \\ &\approx \pi\rho \sum_{-R<r<R} (r u^2 \Delta r) \end{aligned} \tag{8.2}$$

The discretization Δr corresponds to the spatial resolution (i.e., subwindow size) of the DPIV analysis and the limit R for the radial coordinate is determined by the field of view. Although $u \neq 0$ at $r = R$, it is sufficiently small such that u^2 does not contribute much to the computed value of J. Also note that while DPIV cannot capture motions out of the imaging plane, this velocity component does not contribute to the streamwise momentum.

The variation of J with streamwise distance for the three tested propellers at $\Omega = 40$ rad/s is plotted in Figure 8.4. The momentum of the flow is zero for all three cases more than one diameter upstream of the propeller. At the intake, the flow is accelerated to a much higher speed in the presence of a rotating shroud. $J/\mathcal{T}$ of only 0.24 is achieved at the intake of the baseline propeller, whereas $J/\mathcal{T} = 0.75$ in the presence of a rotating shroud. At the exit, $J/\mathcal{T} = 1$ for all three cases. The momentum remains relatively constant in the wake of the baseline propeller, whereas a large overshoot and gradual decay is observed for the shrouded cases.

Actuator disk theory seems to apply well to the baseline propeller, in which the propeller can be modeled as a thin actuator disk that causes a jump in flow properties. The jet momentum is conserved in the wake over $0 < x/D_p < 1$, and the value of the momentum matches closely with the measured thrust. Thus, a momentum analysis on a control volume around the propeller would be valid.

The simple 2D model does not seem to apply, however, in the presence of a co-rotating shroud. The streamwise jet momentum is not conserved in the wake, as it overshoots the measured thrust by over 20% immediately downstream of the shroud and rapidly decays. For the symmetric shroud, J decreases to $0.6\mathcal{T}$ by $x/D_p = 1$.

Propeller rotation rate is now varied to explore the effect of Re. The integrated momentum $J(x)$ is plotted as solid lines in Figure 8.5 for five different Ω, and the

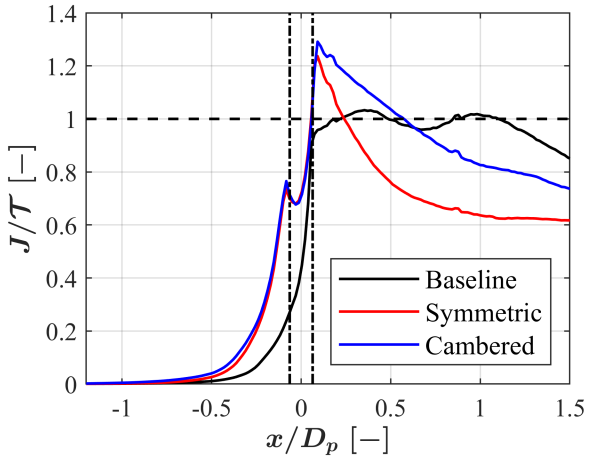

Figure 8.4: Jet momentum produced by the three tested propellers as a function of streamwise distance.

averaged thrust $\mathcal{T}$ measured by a load cell is depicted as horizontal dashed lines. The position of the propeller (i.e., PIV analysis mask) is denoted by vertical black dashed lines for reference.

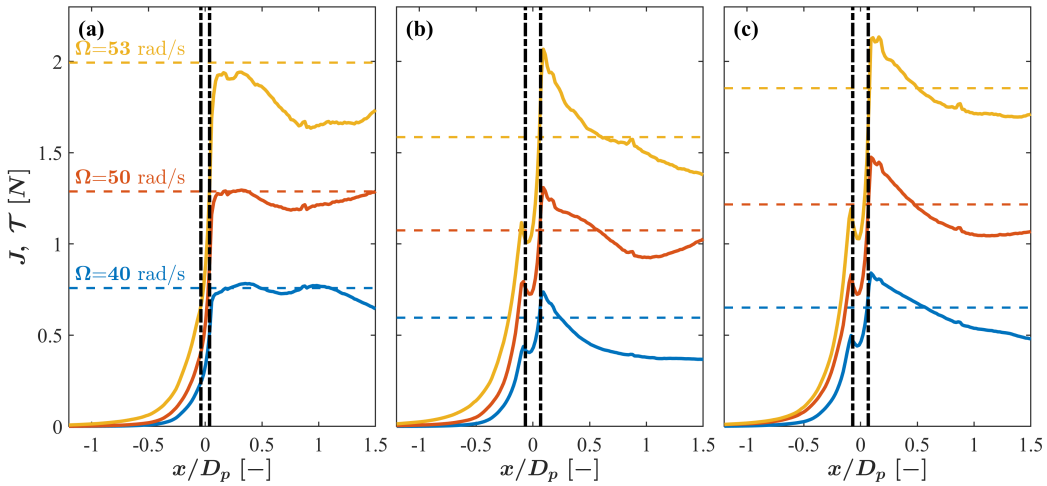

Figure 8.5: Jet momentum as a function of streamwise distance for different rotation rates of the (a) baseline propeller, (b) propeller with symmetric shroud, and (c) propeller with cambered shroud. Dashed lines represent the mean thrust produced at each Ω.

Similar trends are observed on the shrouded propellers, where the momentum overshoots the measured thrust by 20 to 30% at the outlet and then rapidly decays. For the unshrouded propeller, momentum seems to be also conserved at Ω = 50 rad/s, but curiously, it drops rapidly after $x/D_p = 0.5$ at Ω = 53 rad/s.

The absence of streamwise momentum conservation in the near wake implies some 3D or turbulent effects that are not accounted for in this 2D axisymmetric analysis. We expect that a rotating shroud introduces additional swirl to the flow field, making some of the product terms that contribute to streamwise momentum no longer negligible. Further quantitative investigations that capture the out-of-plane velocity component are in order for future work, to understand this interesting phenomenon.

8.2 Vorticity distribution

Time-averaged velocity fields analyzed in the previous section showed changes in the behavior of the intake flow and jet wake, and how these relate to the thrust produced by the propeller. This section analyzes time- and phase-averaged vorticity fields, given by spatial differentiation of the velocity field:

$$\omega = \frac{\partial v}{\partial x} - \frac{\partial u}{\partial y} \tag{8.3}$$

Vorticity provides insights into the shear flow, transitional behaviors of the jet, and tip vortices.

Figure 8.6 compares the time-averaged vorticity fields of the same flows investigated in Figures 8.1 to 8.3. In all cases, the outer region characterized by the blade tip vortex is clearly distinguished from the inner jet core by the sign of ω. Almost no vorticity is generated in the upstream intake region where flow is entrained from, as well as in the wake outside the jet. For the shrouded cases, there seems to be lines of weak vorticity stemming from the leading edge of the shroud profile; these are symptoms of the shadow caused by the lighting and are not real effects of the flow. Its magnitude is highest right at the outlet of the propeller near the blade tip, tracing out the propagation path of the tip vortices.

For the baseline case in Figure 8.6(a), the contraction of the jet which was observed in the velocity analysis is much more evident. The core jet region of the shrouded propellers (b,c) also seems to contract but to a lesser extent, and we know from velocity analysis that the slight contraction is not accompanied by acceleration of the flow. Using $\omega = 0$ as the boundary of the jet core, the contraction can be quantified and compared. The diameter d of this core is indicated by a black arrow at $x/D_p = 0.5$. For the shrouded propellers, d decreases linearly with x in the entire domain investigated, and the symmetric shroud has a slightly higher rate. The baseline propeller follows more of a quadratic curve in the near wake and has a relatively constant diameter over $1.0 < x/D_p < 1.5$.

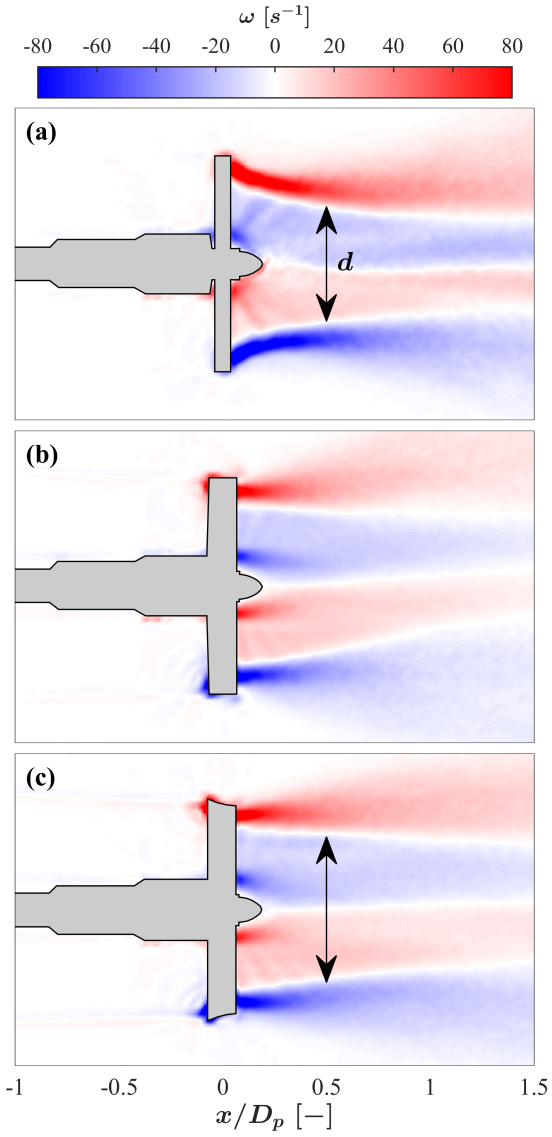

Figure 8.6: Time-averaged vorticity field of the three propeller designs at Ω = 53 rad/s.

The effect of the shroud near the rotational axis can also be observed in the near wake flow, even though the blade geometry is unchanged. At $y/D_p = \pm 0.15$, a small pocket of high vorticity forms, indicating large velocity gradients. This is a direct manifestation of the increased annularity in the jet that was observed in the velocity fields. The velocity magnitude around the streamlined part of the hub is particularly low and does not get "filled in" until further downstream due to the slow contraction. The effect persists slightly further downstream for the symmetric shroud.

In the outer tip vortex region, which has an opposite vorticity sign from the inner jet core region, the presence of the shroud significantly weakens the magnitude of the tip vortex and its propagation downstream. In this time-averaged plot, however, the tip vortices are "smeared out" over its path. Further insight can be gained through phase-locked analysis such that averaging is performed over images captured at constant angular position of the blade.

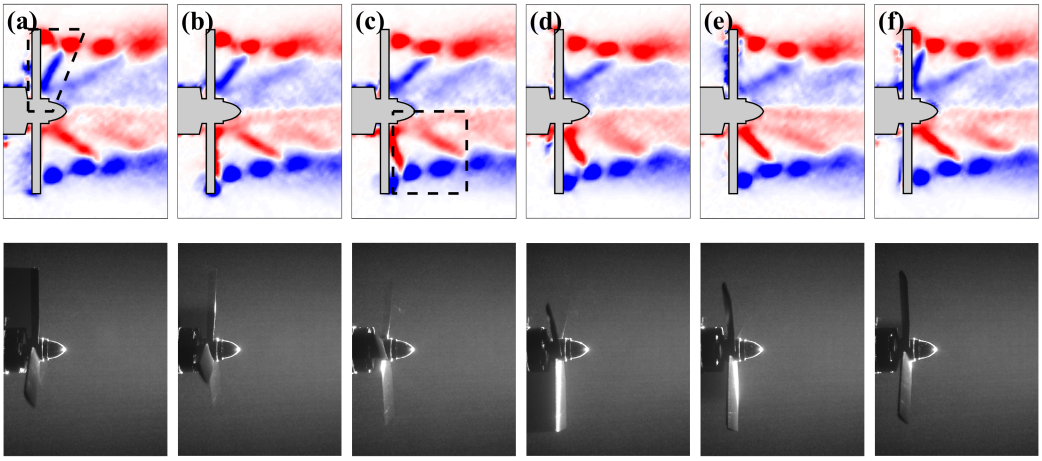

Figure 8.7: Phase-averaged vorticity fields of the baseline propeller at Ω = 62 rad/s, spaced 20° apart in angular position.

A small magnet attached to the motor was detected by a Hall effect sensor, which sent trigger signals which enable phase-locked imaging, as was shown in Figure 6.6. A delay could be specified by sending the signal through an Arduino first. Six equally spaced angular positions of the propeller were considered between the passage of two consecutive blades, as shown in Figure 8.7 for Ω = 62 rad/s. Since the propeller has three blades (120° spacing), this corresponded to angular positions that were 20° apart. As with the time-averaged trials, image pairs had Δt = 1 ms.

The helical structure of the tip vortex is now visible in this 2D slice as discrete circular blobs of high vorticity that are generated as the blade passes through the imaging plane. In the top half of the image in (a), a blade has just passed through the imaging plane, creating a blob of positive vorticity (red) at the blade tip and a line of negative vorticity (blue) over the inner part of the blade (hidden by the mask). The blob-line pair from the previous phase can still be seen clearly, as outlined by dashed lines. The line of negative vorticity points at an angle from the root of the blade to the tip vortex, corroborating the variation in induced velocity with radial distance from the rotation axis. In (b) (d), the tip vortex slowly propagates downstream and

the slant of the line in the inner region increases. The relative motion of the inner and outer regions is perhaps most clear in the bottom half of (c), again outlined by dashed lines. Two tip vortex blobs are contained between adjacent inner lines, demonstrating that the inner jet core moves much faster than the outer tip vortex structure. The two regions seem to "slip" relative to each other and can be analyzed separately based on the sign of vorticity, which will prove helpful for unsteady flows studied in the next chapter.

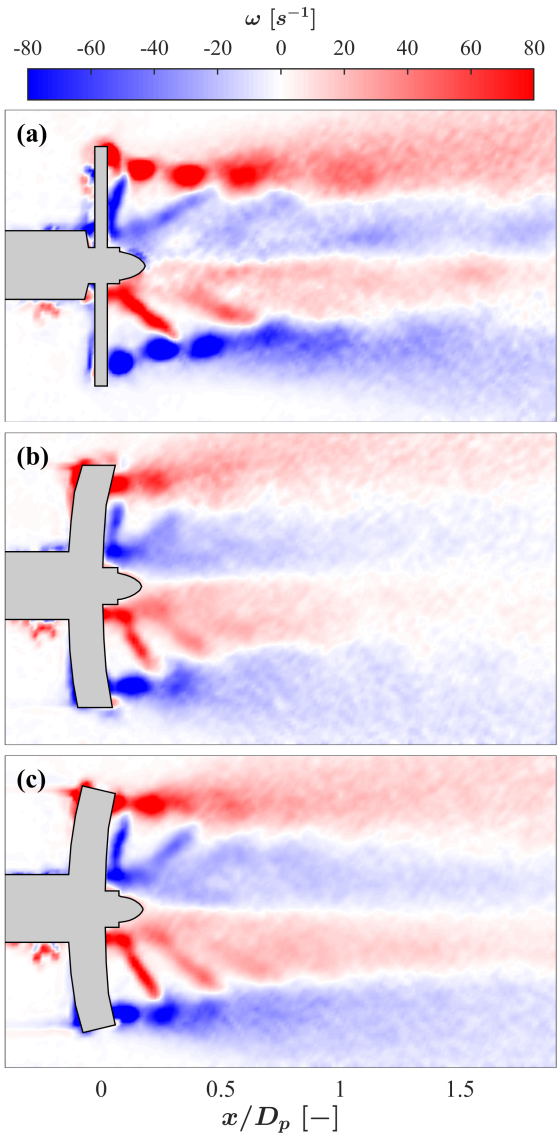

Figure 8.8: Phase-averaged vorticity field of the three propeller designs at Ω = 62 rad/s.

Figure 8.8 compares the phase-averaged vorticity fields for the three tested propeller

configurations at the same phase and Ω. In the baseline case (a), a coherent tip vortex structure persists to $x/D_p \approx 0.8$ before dissipating, corresponding to about 3.5 rotations. With the symmetric and cambered shrouds (b,c), the coherent structure only persists for about half of that distance, as the blobs are fully dissipated by $x/D_p \approx 0.4$ and 0.5, respectively. Blade-vortex interactions are often associated with drone noise that humans find most irritating, and conventional stationary shrouds have been shown to reduce this noise both for near and far observers. Similar improvements can be expected for the proposed rotating shroud based on the significant reduction in tip vortex footprint.

In the inner jet core region, passage of the blade through the imaging plane similarly produces a line of high vorticity with opposite sign from the tip vortex. In the near wake, large pockets of $\omega \approx 0$ exist between these lines which smear out further downstream. While the coherence of these inner structures seems to persist up to the same x/D_p as the tip vortex, their propagation speeds differ significantly. The acceleration of the core jet in the baseline case (a) causes the lines on the upper half in this snapshot to span two tip vortex blobs. The spacing between these lines decreases in the shrouded cases, but the relative motion of the outer and inner regions still exists.

Ultimately, however, MAV applications require high maneuverability and agility as they spend a significant portion of their mission profile in unsteady and turbulent flow conditions. As a step toward better understanding of the unsteady effects of the co-rotating prop-shroud system, the next chapter explores the physics of the propeller start-up phenomenon.

Chapter 9

UNSTEADY DYNAMICS OF THE STARTING VORTEX RING

How and why does an airfoil generate lift? Different aerodynamicists will provide various (correct and incorrect) answers to the question, as the lift mechanism is neither intuitive nor fully understood. A mixture of viscid and inviscid flow models have been employed to understand this ubiquitous yet perplexing mechanism in nature and engineered systems alike.

Lift is generally accepted as an inviscid phenomenon. One of the simplest explanations invoke Newton's 2nd and 3rd laws of motion. As the airfoil redirects the flow momentum downward through its camber or angle of attack (or both), it exerts a downward force on the fluid. In reaction, the fluid must exert and equal upward force on the airfoil which corresponds to lift. Although this doesn't fully capture the ability of the flow over the upper (suction) surface of an airfoil to remain attached and also deflect downward, the phenomenon doesn't depend on shear forces or viscosity.

Thus, potential flow theory combined with some conformal mapping (e.g., Joukowsky transformation (Joukowsky, 1910)) is often used to predict the flow around an airfoil. However, predicting the lift requires an additional step, which is the introduction of a jump in potential representing circulation Γ. Out of the infinitely many values of Γ that can be prescribed, the physically reasonable choice is determined by imposing the Kutta condition at the sharp trailing edge. This results in the famous Kutta-Joukowsky theorem which states that lift is directly proportional to the circulation:

$$F_L = \rho U \Gamma \tag{9.1}$$

This model is a good approximation for many real flows at high Re where inertial effects dominate viscous effects, but begs many questions about the role of viscosity. What happens if the trailing edge isn't sharp (Gonzalez and Taha, 2022), and where does the circulation come from?

The development of circulation on an airfoil is explained through Kelvin's circulation theorem and the starting vortex. When an airfoil is impulsively started from rest, a vortex rolls off the trailing edge whose circulation must be equal and opposite to that around the airfoil. The mechanism is summarized well in (Carlton, 2007) and

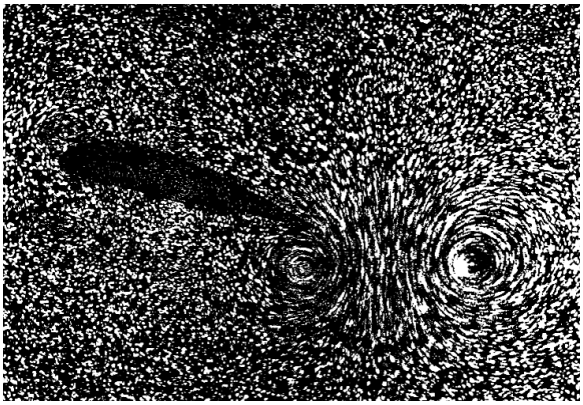

Figure 9.1: Visualization of vortices that form as an airfoil is impulsively started and stopped. Adapted from Figure 55 of (Prandtl and Tietjens, 1934).

was visualized by (Prandtl and Tietjens, 1934; Prandtl, 1936) (Figure 9.1) and many others thereafter. Some of these early visualizations were analyzed using modern particle velocimetry techniques (Willert et al., 2019). The unsteady vortex dynamics of a starting airfoil and its contributions to lift can be much more complex (Chang, Hsiau, and Chu, 1993) especially if we consider longer time scales that transition into steady state.

A propeller, or rotating airfoil, also produces a starting vortex as it is accelerated from rest. The properties of this vortex, then, are expected to provide important insights into the propulsive capabilities of the propeller which may aid in its design and optimization. This chapter begins with a largely qualitative exploration of the phenomenon through pathline visualizations. Then, quantitative tools are developed to characterize its motion and growth. The unshrouded propeller is compared to the propeller with cambered shroud.

9.1 Overview of the phenomenon

We begin by providing an overview of the salient features of the starting vortex phenomenon. Figure 9.2 depicts pathline visualizations at select times after the baseline propeller begins accelerating from rest at $t = 0$, reaching a steady rotation rate of $\Omega_0 = 55.1$ rad/s in $t_0 = 20$ ms. Each image is constructed by color-coding and overlaying 25 consecutive grayscale particle images captured with a high-speed camera at 1000 Hz, creating a time-lapse effect with an exposure of 25 ms that reveals particle pathlines. Note that these visualizations only capture a 2D slice through the propeller's axis of rotation, while the flow structures are 3D and highly turbulent in nature.

At t = 0.1 s, vortices begin to form near the blade tip. It resembles a closed, axisymmetric vortex ring, although the phenomenon is helical in nature because the tip speed of the propeller is much faster than the translational speed of the vortex ring structure. By t = 0.3 s, the starting vortex has grown and propagated slightly downstream. The core jet produced by the propeller also becomes visible. The vortex continues to propagate downstream and is clearly interacting with the jet at t = 0.7 s. It seems to be pulling the jet outward and away from the centerline while entraining fluid from it. In this regime, it is difficult to distinguish the jet from the vortex ring. By t = 1.0 s, though, the vortex begins to pinch-off from the jet. The vortex does not seem to have grown much in size from the previous image and the jet exhibits stronger streamwise momentum. The lower half of the vortex also seems to be deforming and dissipating. The jet has fully penetrated the vortex ring at t = 1.5 s, and while interactions continue to occur between the two, the vortex ring is no longer entraining fluid from the jet. The vortex gradually decays, and a linearly expanding turbulent jet is observed in the final frame of the sequence corresponding to the "steady" state that was analyzed earlier in the chapter.

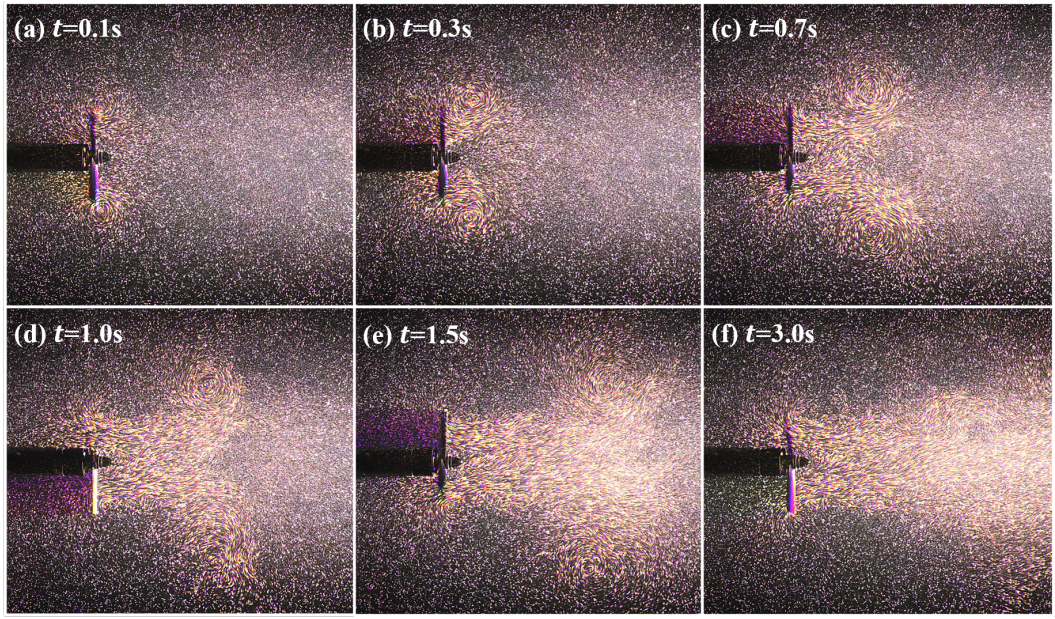

Figure 9.2: Pathlines (exposure = 25 ms) visualizing the development and propagation of the starting vortex as the baseline propeller is accelerated from rest.

Thus, the starting vortex phenomenon can be roughly divided into four steps: inception (a), growth via jet entrainment (b,c), pinch-off and jet penetration (d,e), and decay (f). Ultimately, only the core jet remains.

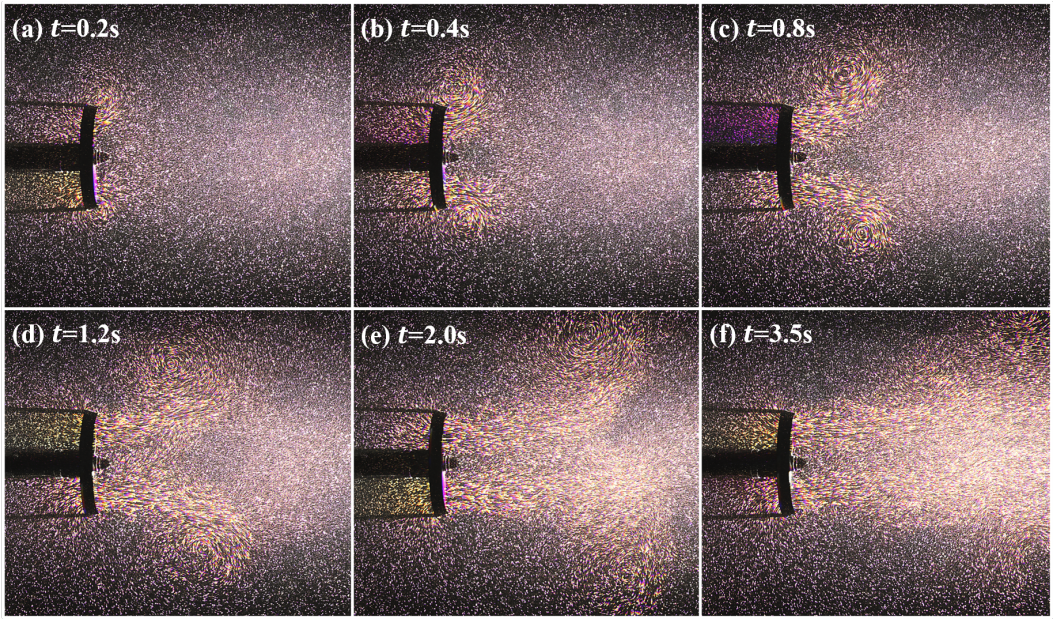

Figure 9.3: Pathlines (exposure = 25 ms) visualizing the development and propagation of the starting vortex as the propeller with cambered shroud is accelerated from rest.

Similar overall trends are observed on a propeller with a positively cambered shroud. The sequence of images is shown in Figure 9.3 for the same Ω_0 as the baseline propeller but with a slightly different selection of timestamps. The presence of the shroud mitigates tip vortices, resulting in a slower and weaker inception. Thus, the vortex pathlines only start to become visible around $t = 0.2$ s. Then, the vortex undergoes a similar roll-up process during which it grows by entraining fluid from the jet. The vortex seems to be pushed further out from the centerline compared to the baseline case because the jet contraction is mitigated by the presence of the shroud, as was shown in the time-averaged analysis. Eventually, the vortex pinches off and the jet penetrates through, again producing a linearly expanding turbulent jet.

A natural question that arises is how the starting vortex and its interactions with the jet affect the thrust produced by the propeller. The thrust measured by a single-axis load cell during the first 0.5 s of each propeller's startup is plotted in Figure 9.4. The raw data sampled at 1 kHz is plotted in gray and a low-pass filter of 40 Hz is applied to obtain the red curve. The baseline propeller in (a) experiences a fast initial ramp-up associated with a large overshoot, reaching its maximum value around $t = 0.05$ s. In contrast, the shrouded propeller in (b) has slower ramp up

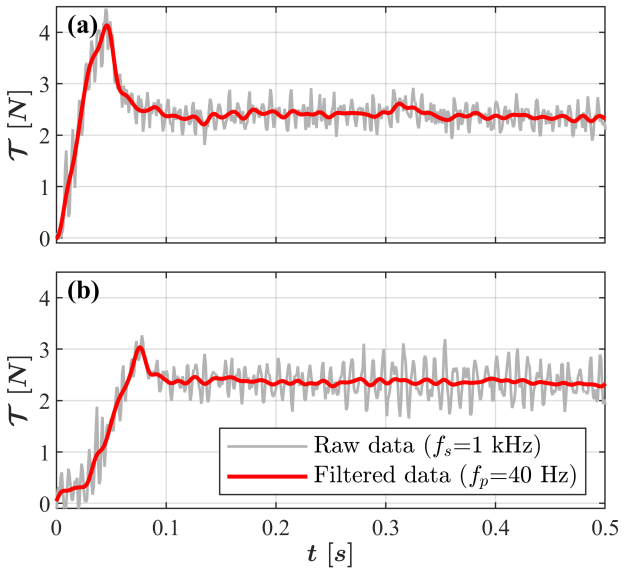

Figure 9.4: Raw and filtered thrust signals during startup of the (a) baseline propeller and (b) propeller with cambered shroud.

and small overshoot. The overshoot may be related to the strength of the blade tip vortex generated, since the circulation of the starting vortex is an indicator of lift for 2D airfoils. This provides another piece of evidence that the co-rotating shroud mitigates tip vortices.

9.2 Vortex propagation and growth

Based on the time-averaged investigations of the steady-state jet in the previous chapter and pathline visualizations of the starting vortex, the flow may be approximated as axisymmetric. In subsequent quantitative analyses, we therefore focus only on a single side of the rotational axis, increasing the spatial resolution of the acquired flow field. The new FOV is $x/D_p \in [-0.25, 2.25]$ and $y/D_p \in [0, 1.4]$, as can be seen in e.g. Figure 9.8. Other image acquisition settings as well as DPIV analysis settings remain the same.

In each trial, a step function signal is given to the motor at $t = 0$ s to rotate at $\Omega_0 = 57$ rad/s and then the signal is turned off at some stopping time $t = t_s$. For each of the two tested propellers (baseline and cambered shroud), the total circulation Γ in the FOV is plotted as a function of time in Figure 9.5(a) & (b) for three different stopping times, differentiated by the darkness of the line color. Mathematically,

there are two equivalent methods for calculating Γ:

$$\Gamma = \oint_C \vec{u} \cdot d\vec{l} = \oint_S \vec{\omega} \cdot \hat{n}\, dA \tag{9.2}$$

We choose the method that uses vorticity rather than velocity.

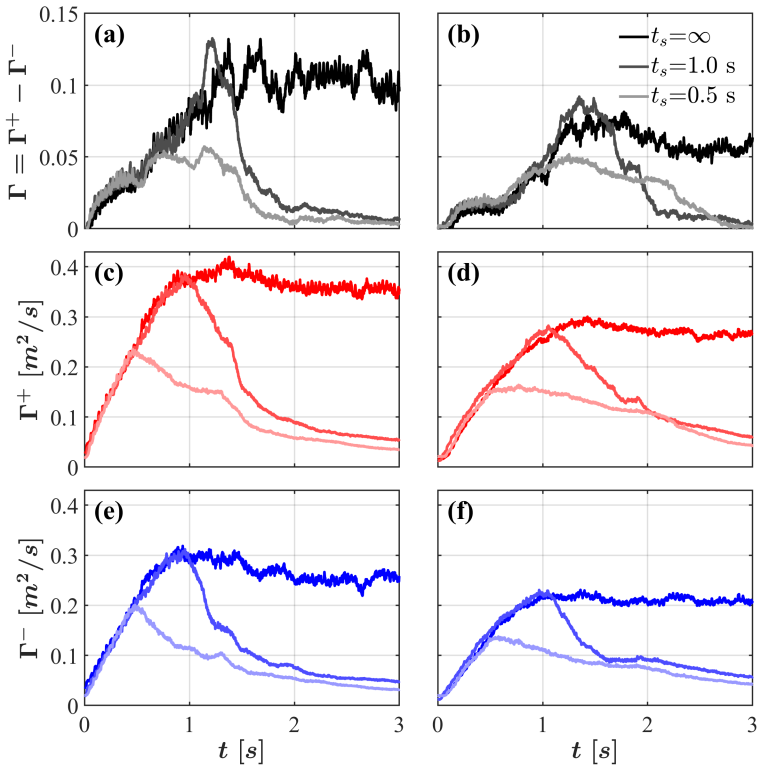

Figure 9.5: Total circulation in the FOV for the (a) baseline and (b) shrouded propellers, as well as the (c,d) positive and (e,f) negative decomposition. Three cases of propeller stopping time t_s are shown.

In Chapter 8 it was observed that the inner jet core could be distinguished from the outer tip vortex structure by the sign of ω. Thus, the total circulation is decomposed into its positive and negative contributions and plotted in shades of red and blue, respectively. These plots (c-f) have significantly less noise than the total Γ, enabling visual identification of peaks and transition points.

Looking at the baseline propeller results in the left column, both Γ^+ and Γ^- grow linearly at early times $t < 1.0$ s. For the $t_s = 0.5$ s and 1.0 s cases, they peak at the moment the propeller is stopped and rapidly begins to decay. The decay is mostly exponential, with some deviation while the starting vortex is exiting the FOV. If the propeller is never stopped ($t_s = \infty$), vorticity does not decay but the maximum vorticity in the FOV also does not continue to increase beyond the peak

of the $t_s = 1.0$ s case. By around $t = 2.0$ s, the steady state jet is achieved and both Γ^+ and Γ^- values stabilize. The overall Γ is positive.

The shrouded propeller in the right column exhibits similar linear growth in Γ^+ and Γ^- until the propeller is stopped. The decay, however, occurs much more slowly. In the $t_s = 0.5$ s, Γ^+ remains relatively constant until $t = 1.0$ s and then decays linearly rather than exponentially all the way up to $t = 3.0$ s. The peaks are lower than those of the baseline propeller, suggesting again that the shroud is suppressing the positive vorticity at the tip but also the negative vorticity in the jet.

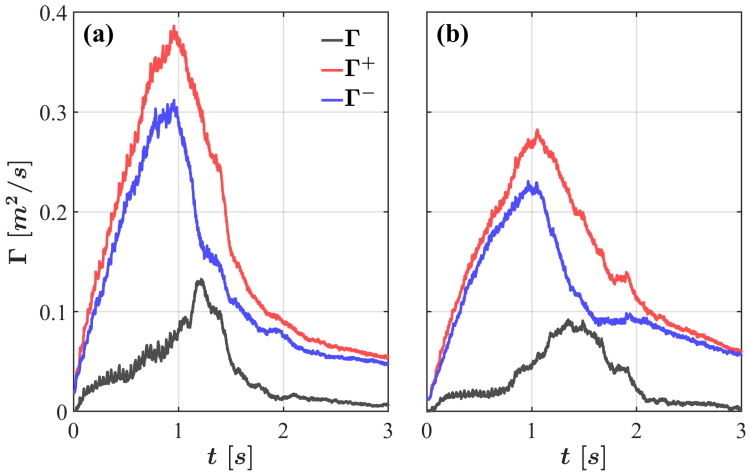

Figure 9.6: Positive, negative, and total circulation in the FOV for the $t_s = 1.0$ s cases of (a) the baseline propeller and (b) shrouded propeller.

The positive, negative, and total circulations for the $t_s = 1.0$ s are replotted in Figure 9.6 to enable a more direct and detailed comparison of the trends described above. Note that for both propellers, the peaks of Γ^+ and Γ^- occur at t_s, but the peak of Γ is slightly delayed. This suggests that the jet (Γ^-) decays slightly faster than the starting vortex (Γ^+).

Now that we have an idea of how the starting vortex and jet contribute to the development of the vorticity field with time, we wish to analyze its motion, size, and strength. The translational speed of a vortex ring with ring radius a and cross-sectional radius $R_v \gg a$ is given analytically by (Fetter, 1974)

$$u_v = \frac{\Gamma_v}{4\pi a}\left[\ln\left(8\frac{a}{R_v}\right) + k\right] \tag{9.3}$$

where Γ_v is the circulation and k is a constant. Although the propeller starting vortex under study does not satisfy some of the idealized assumptions required in

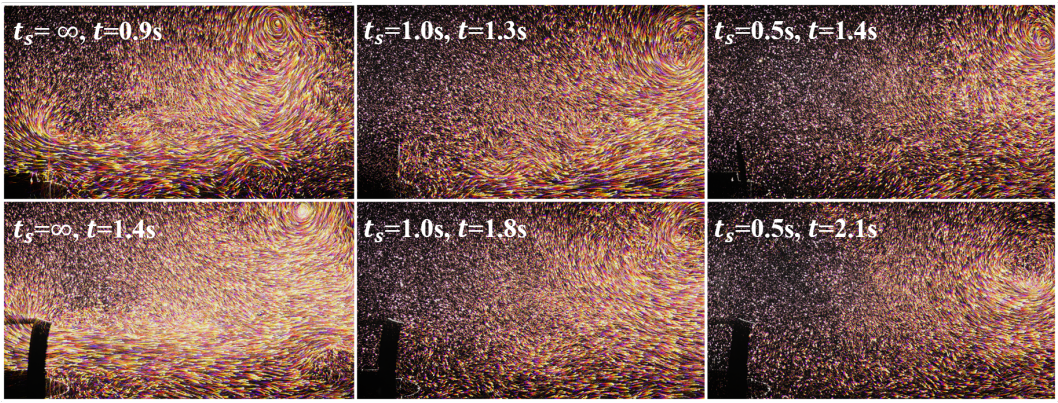

Figure 9.7: Pathline visualizations (exposure = 50 ms) of the six cases presented in Figure 9.5 as the starting vortex reaches the edge of the FOV.

the derivation of Equation 9.3, we observe that circulation is still related to speed. Figure 9.7 compares pathline visualizations of the six cases studied in Figure 9.5 when the core of the starting vortex reaches the edge of the FOV. Broadly speaking, the longer it takes to reach the edge, the slower its average speed. Thus, the starting vortex of the shrouded propeller is slower than that of the baseline propeller for a given t_s, and the speed decreases as t_s is decreased. Both trends suggest that lower Γ^+ results in slower starting vortices.

We analyze the path of the vortex more quantitatively for the $t_s = \infty$ cases. Three manual methods for locating the vortex core (center of the cross-section, not the ring) were compared, visualized in Figure 9.8 for the baseline propeller and 9.9 for the shrouded propeller at a particular instant in time. In the "pathline" method (b), a pathline visualization with 20 ms exposure centered at the time of interest is created, i.e., by using 10 frames before and after the instant. The pixel coordinates of the eye of the vortex are recorded. The centroid of the positive vorticity blob is used in (c), and the centroid of the vortex discriminant is used in (d). The vortex discriminant (Stamhuis and Videler, 1995) is computed as

$$\mathcal{D} = \left(\frac{\partial u}{\partial x} + \frac{\partial v}{\partial y}\right)^2 - 4\left(\frac{\partial u}{\partial x}\frac{\partial v}{\partial y} - \frac{\partial u}{\partial y}\frac{\partial v}{\partial x}\right) \tag{9.4}$$

The discriminant method seemed to be most reliable and consistent across all snapshots, although all three methods gave similar results. The average deviation of the pathline and vorticity centroid methods from the discriminant method was 0.014 and 0.008 in dimensionless length units, respectively.

Positions of the starting vortex center computed using the discriminant method are

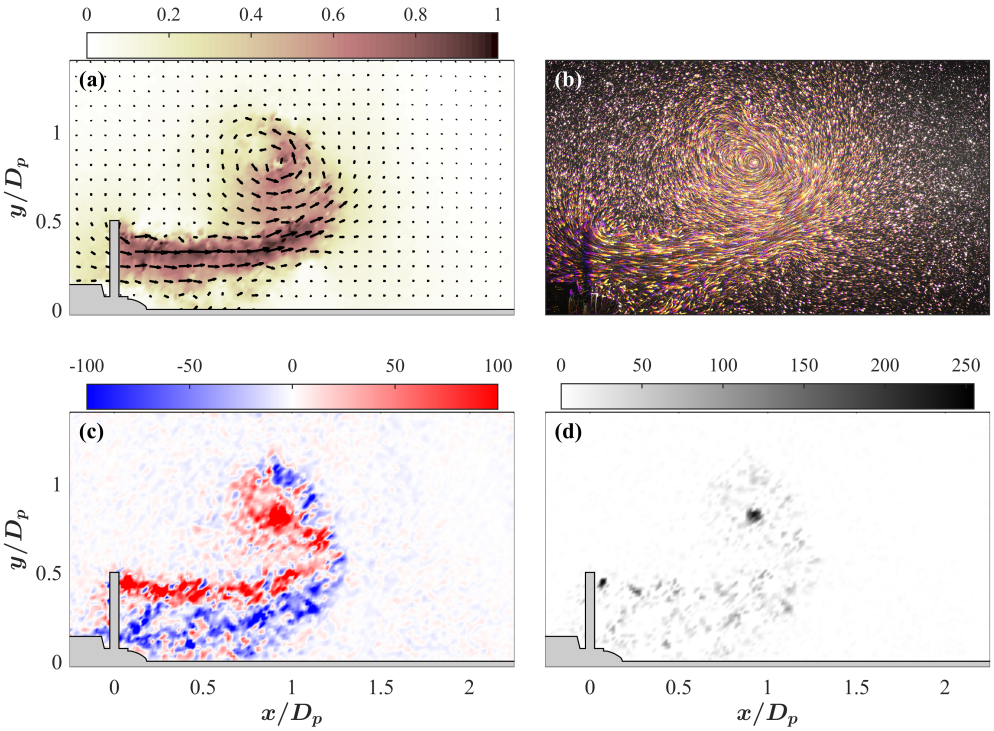

Figure 9.8: Different methods used to locate the vortex center at $t = 0.5$ s on the baseline propeller. (a) Velocity field and magnitude, (b) pathlines with 20 ms exposure, (c) vorticity, and (d) vortex discriminant.

plotted in Figure 9.10 every 50 ms. The circles represent the vortex path of the baseline propeller and the triangles represent that of the shrouded propeller, each color-coded by t. Dashed lines show a linear fit of the data up to $x/D_p = 1.6$, and a pathline image of the baseline propeller at $t = 0.5$ s is shown in the background for reference.

The baseline propeller's vortex travels closer to the jet and in a relatively straight line until $t = 0.75$ s, when it pinches off from the jet and suddenly obtains a significant vertical velocity. Its average translational velocity during this period, during which it is entraining fluid from the jet core, is 0.21 m/s. The shrouded propeller's vortex also travels in a straight line for the first 0.75 s, but more radially outward and with a slower translational velocity of 0.18 m/s. At this point, the vortex has not pinched off yet and turns slightly inward as if being pulled by the jet. Pinch off occurs at $t = 1.05$ s, where the vortex suddenly begins to move vertically like in the baseline case. Beyond $t = 1.2$ s, the vortex decays and its translational speed is reduced significantly.

Having analyzed the development of the vorticity field and the motion of the starting

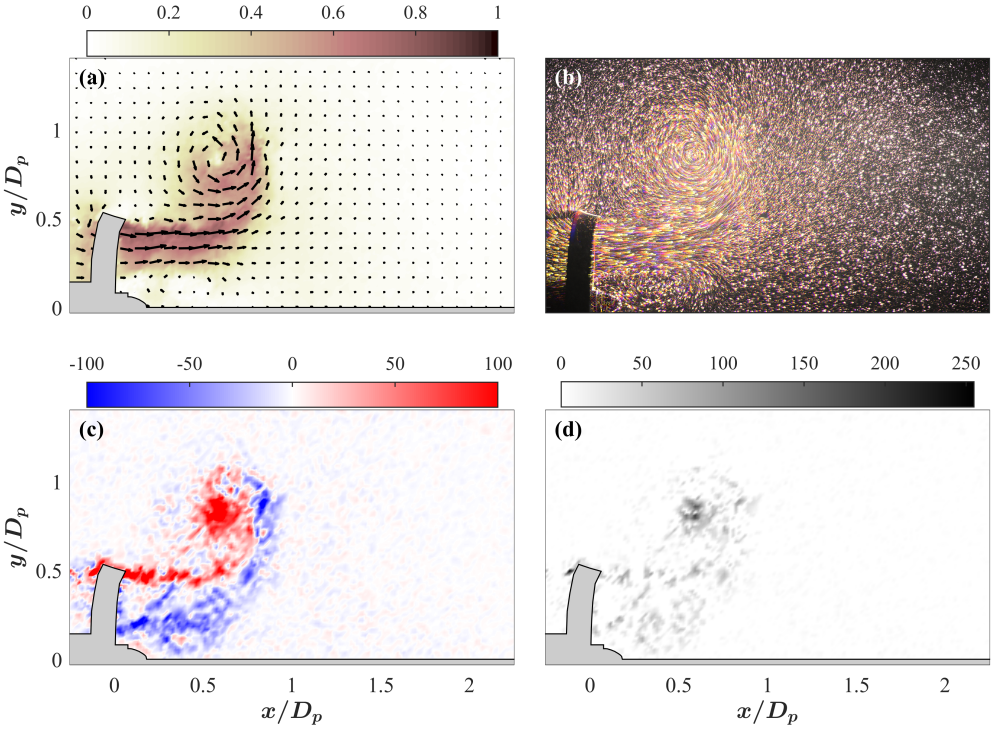

Figure 9.9: Different methods used to locate the vortex center at t = 0.5 s on the propeller with cambered shroud. (a) Velocity field and magnitude, (b) pathlines with 20 ms exposure, (c) vorticity, and (d) vortex discriminant.

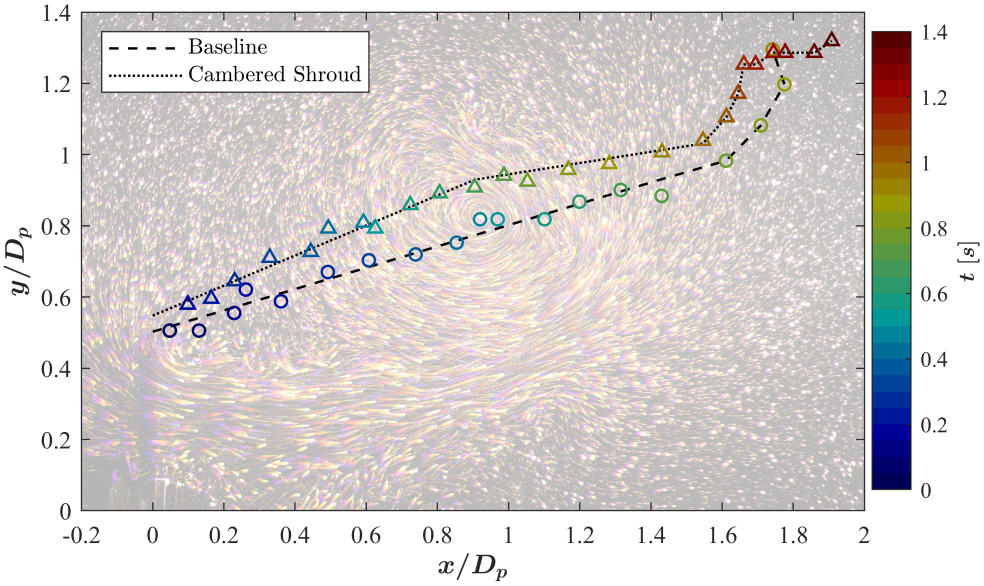

Figure 9.10: Comparison of vortex propagation path of the two propellers as determined by the vortex discriminant method. Marker color corresponds to time.

vortex, the remaining quantity of interest is its strength. Γ^+ integrated over the entire FOV hinted that the shrouded propeller produces a weaker starting vortex ring. This will be addressed in more detail in the subsequent section and interpreted in terms of a dimensionless formation time.

The presence of a rotating shroud seems to have a significant impact on the path, propagation speed, and strength of the propeller's starting vortex. In the case of the shrouded propeller, the jet influenced its path even after it had propagated one propeller diameter downstream, although the thrust produced is largely unaffected by these interactions in a quiescent and isolated environment. These factors can become significant, however, for rotor-rotor interactions, rotor-body interactions, ground effect, or in the vicinity of other obstacles. These are important areas of future work that would help mature the technology and potentially lead to discoveries of new benefits.

9.3 Analogy with vortex ring formation time

Vortex rings occur in many natural and manmade phenomena, from bird flight to the "airzooka" toy. In the laboratory, vortex ring formation has been rigorously studied on a piston-cylinder apparatus, summarized well in review articles such as (Shariff and Leonard, 1992). As a piston is pushed down the cylinder, a boundary layer of vorticity forms and separates from the downstream edge, rolling up into a ring. Vortex rings formed in this way are characterized by a maximum amount of vorticity flux they can accept, corresponding to a limiting dimensionless parameter that represents the ratio $\hat{T}$ of piston stroke length to cylinder diameter (Gharib, Rambod, and Shariff, 1998). They showed that above $\hat{T} \approx 4$, the main vortex ring stopped growing in size and the rejected vorticity flux created trailing secondary vortices, as shown in Figure 9.11. More generally, $\hat{T}$ can be interpreted as a dimensionless time scale referred to as "formation time"

$$\hat{T} = \frac{\int U \, dt}{D} \tag{9.5}$$

where U and D are the characteristic velocity and length scales, respectively, of the shear layer feeding the vortex ring over time period t. The concept has been used to understand optimal vortex formation across various complex biological systems (Dabiri, 2009).

Can the starting vortex ring on propellers also be understood in this framework? This section quantitatively analyzes the growth process of the vortex ring to develop an analogous formation time model.

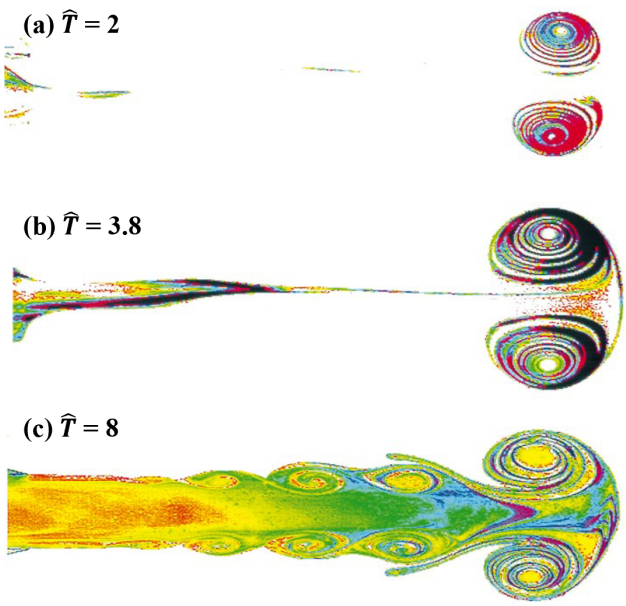

Figure 9.11: Visualization of vortex rings generated by a piston-cylinder apparatus, taken from Gharib, Rambod, and Shariff, 1998. Different stroke ratios were used to vary the formation time $\hat{T}$.

We begin by computing the circulation Γ_v contained inside the starting vortex at various t. The reader is reminded again that this analysis takes a 2D slice of a 3D vortex ring structure. To integrate for Γ_v using the vorticity formulation of Equation 9.2, a closed region S needs to be defined. This is not a simple task, given the turbulent nature of the instantaneous flow field and the ambiguous boundary between the vortex and the jet it entrains from. The shape of the vortex is continuously deforming as well.

These complications notwithstanding, an initial attempt was made which approximates the vortex as a circle of radius $R_v(t)$ whose center $(x_v(t), y_v(t))$ was found from the vortex discriminant method in Figure 9.10. $R_v(t)$ is chosen manually to completely encircle the vortex core (region with high $\omega > 0$) without crossing into the jet ($\omega < 0$) region. Sample snapshots of $S(t)$ are shown in Figure 9.12 for (a) the baseline propeller and (b) the shrouded propeller. There is admittedly some subjectivity in the choice of $R_v(t)$, but the procedure will suffice for the purpose of the following analysis.

Once the circular region $S(t)$ has been defined, the discretized ω field is summed

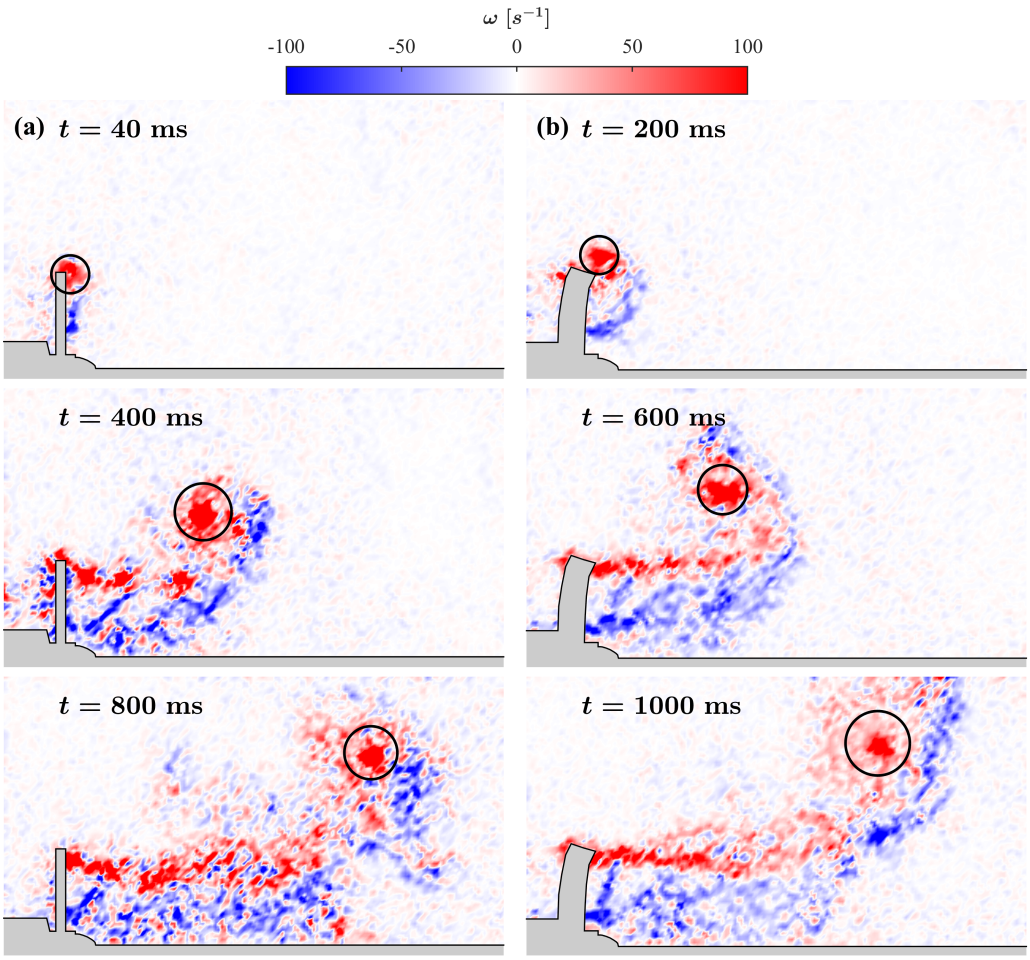

Figure 9.12: Tracking the position and size of the starting vortex at various times for (a) the baseline propeller and (b) propeller with cambered shroud.

over the points contained within:

$$\Gamma_v = \sum_{(x-x_v)^2+(y-y_v)^2 \leq R_v^2} \omega(x,y)\Delta x \Delta y \tag{9.6}$$

Γ_v is plotted against dimensional time in Figure 9.13(a) & (c). Linear trendlines are superposed in red. Initially, the circulation of both propellers' starting vortices grow linearly. Data for the shrouded propeller looks much cleaner, most likely due to the stronger effect of the blade tip vortices with the baseline propeller. Both achieve a maximum value of Γ_v around $t = 0.4$ s, with the baseline propeller's vortex having about 25% more circulation.

Γ_v of the baseline propeller decreases gradually until about $t = 0.9$ s, and then rapidly afterwards as the vortex moves out of the FOV. For the shrouded propeller, it remains relatively constant at about 0.04 m^2/s then decays slightly. It takes much

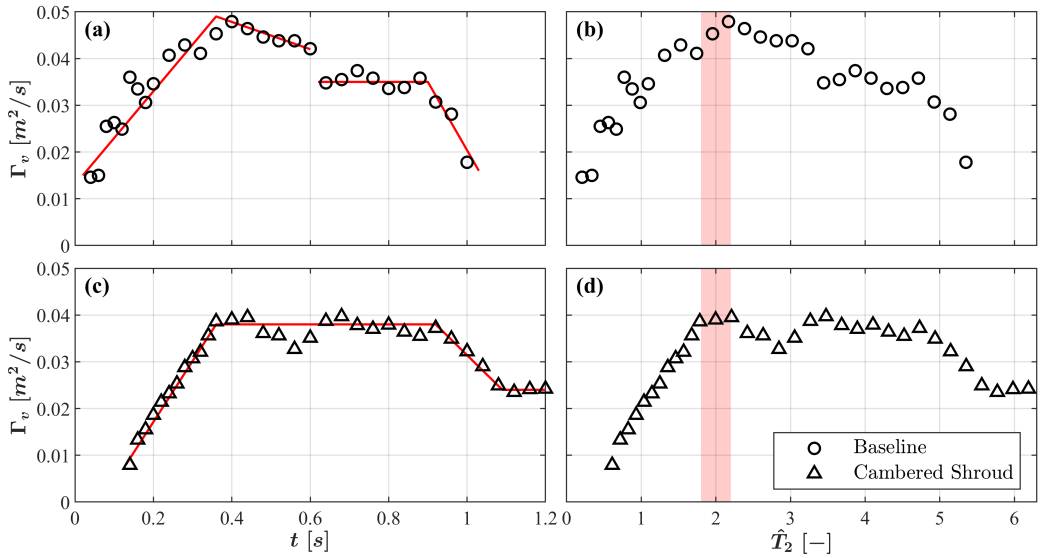

Figure 9.13: Circulation Γ_v contained within the starting vortex plotted against (a,c) dimensional time and (b,d) dimensionless formation time for the two propellers tested.

longer to exit the frame as it has a slower translational speed. Interestingly, the curve dips slightly over 0.5 s $< t <$ 0.6 s but recovers, which correlates with the period over which the vortex tentatively moved slowly according to Figure 9.10.

A limit on vortex growth is clearly observed in both cases, motivating an analysis using dimensionless formation time. We define $\hat{T}_2$ following Equation 9.5 (reason for the subscript 2 will become apparent later), postulating that the characteristic scales of the core jet affect the vorticity flux: U is the average velocity of the jet and D is the propeller diameter which approximates jet diameter. Since the instantaneous velocity field from PIV is quite noisy due to the turbulent 3D nature of the flow, we rely on thrust measurements (Figure 9.4) to infer the spatial average $\tilde{u}_{jet}$ of the jet velocity profile as

$$\mathcal{T}(t) = \int (\rho u^2) dA = \rho \tilde{u}_{jet}(t)^2 \left(\frac{\pi D_p^2}{4} \right) \tag{9.7}$$

The relationship between jet velocity and thrust was discussed in detail in Chapter 8 for the steady-state operation of the propeller. It was found that the measured thrust matched well with the streamwise jet momentum at the propeller outlet, especially for the baseline propeller whose momentum was conserved to within 5% for one propeller diameter in the wake.

Thus, the formation time for the starting vortex is

$$\begin{aligned}\hat{T}_2 &= \frac{1}{D_p}\int_{t_0}^{t} \tilde{u}_{jet}(t')\,dt' \\ &= \frac{2}{D_p^2\sqrt{\pi\rho}}\int_{t_0}^{t} \sqrt{\mathcal{T}(t')}\,dt'\end{aligned} \tag{9.8}$$

Suppose $t_0 = 0$, that is, integration begins the instant the propeller begins to accelerate from rest. The plot of Γ_v is replotted in terms of $\hat{T}_2$ in Figure 9.13(b) & (d). Despite differences in the ramp up time between the two propellers, the circulation of both starting vortices saturate around $\hat{T}_2 \approx 2$, indicated by a light red region in the plot. Thus, the limiting formation time, or "formation number" as coined by (Gharib, Rambod, and Shariff, 1998), of this configuration under the described framework is 2.

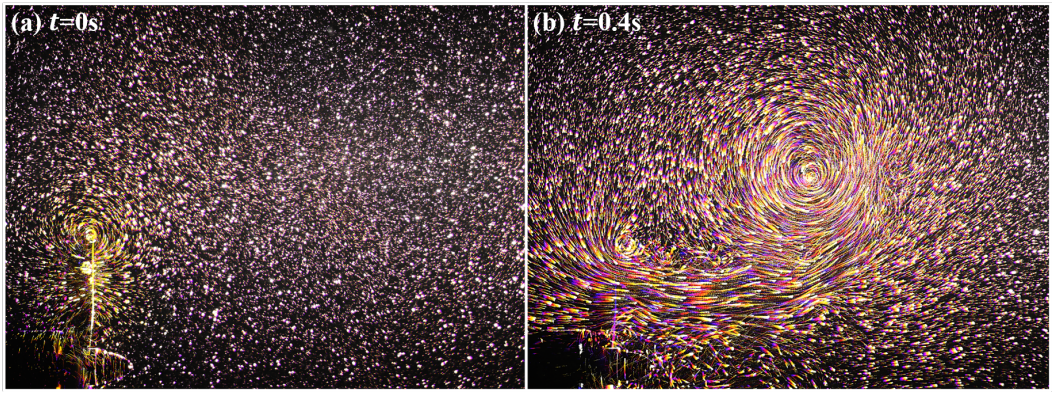

Figure 9.14: The starting vortex grows under different mechanisms (a) at very early times upon initial inception by the blade tip and (b) after it has propagated away from the blades.

Flow visualizations suggest, however, that the inception of the starting vortex occurs before an inner jet core is developed. This is shown by pathlines around the baseline propeller during the first 25 ms in Figure 9.14(a). A vortex can be seen near the blade tip but it is not entraining any mass or vorticity from the inner jet, unlike in (b) which is taken at a much later time. Thus, the vortex growth at very early times $0 \leq t \leq t_0$ must be governed by an entirely different mechanism.

The shear layer feeding the vortex ring during this initial phase must be the boundary layer that develops over the accelerating blades, much like the starting vortex roll-up process shown in Figure 9.1. The characteristic length and velocity scales of this shear layer, therefore, would be the blade chord c and blade tip velocity

$u_{tip}(t) = \frac{1}{2} D_p \Omega(t)$. Considering the existence of two distinct phases of the vortex formation process, the total or cumulative formation time may be expressed as

$$\begin{aligned} \hat{T} &= \hat{T}_1 + \hat{T}_2 \\ &= \frac{1}{c} \int_0^{t_0} u_{tip}(t')\, dt' + \frac{1}{D_p} \int_{t_0}^{t} \tilde{u}_{jet}(t')\, dt' \end{aligned} \tag{9.9}$$

Let $f(\tau) = \Omega/\Omega_0$, where $\tau = t/t_0$ is the normalized time variable. Then, the integral for formation time during the first phase can be written as

$$\hat{T}_1 = \frac{D_p \Omega_0 t_0}{2c} \int_0^1 f(\tau)\, d\tau \tag{9.10}$$

The precise control or determination of $f(\tau)$ (or equivalently $\Omega(t)$) is difficult with a brushless DC motor that is used in the current setup, but estimates can be made by mathematically modeling the ramp up process. We may, for example, consider a linear profile in which a steady rotation rate $\Omega = \Omega_0$ is reached at $t = t_0$, a square root profile, or an exponential profile that reaches $0.9\Omega_0$ at t_0 and approaches Ω_0 as $t \to \infty$. These are shown in Figure 9.15. Then, the definite integral in Equation 9.10 can be evaluated readily as 0.5, 0.667, and 0.609, respectively.

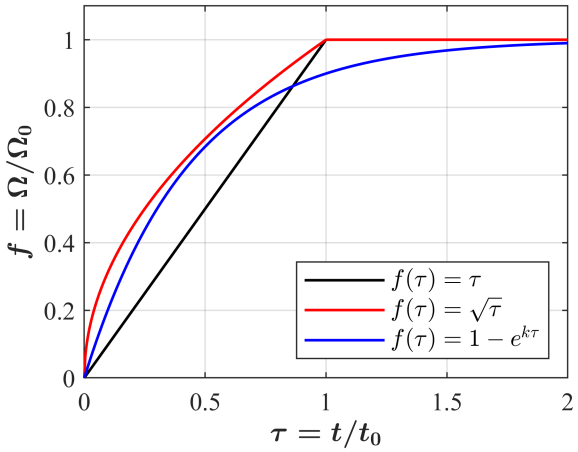

Figure 9.15: Possible mathematical models for the propeller ramp-up velocity profile.

The final challenge is determining the value of t_0 at which the source of vortex growth switches to the inner jet. To do so quantitatively, a few intuitive choices come to mind such as when Γ_0 is reached, the instantaneous velocity on the centerline surpasses some threshold, or a steady thrust level is reached. However, it is not immediately

clear which of these might be "most correct," especially since the actual process is more of a gradual transition. For the baseline propeller, tracking the position of the blade tip with a high-speed camera indicated that $\Omega_0 = 55.1$ rad/s had been reached by $t_0 = 20$ ms, which would give $\hat{T}_1 = 1.87$ assuming linear ramp up. On the other hand, pathline visualizations in Figure 9.16 show the jet core starting to get entrained around $t_0 = 40$ ms even though the vortex center has not yet propagated very far from the blade tip. A steady thrust is not obtained until approximately $t_0 = 80$ ms, which corresponds to the last frame (h) in the sequence.

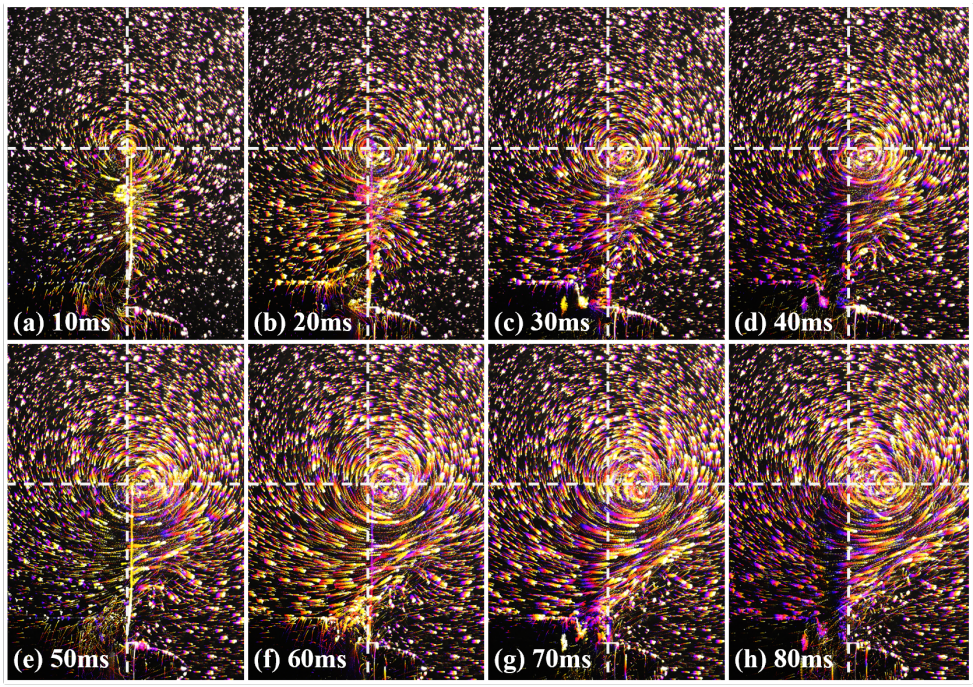

Figure 9.16: Pathline visualizations of 20 ms exposure time in 10 ms increments, showing the transition into the phase where vortex grows via jet entrainment. Dashed grid is aligned with the vortex center in the first frame (a).

Within the scope of this study, we observed the existence of a limit on the growth of the starting vortex ring, both on the propeller with and without a co-rotating shroud. The shroud affected both the trajectory and maximum strength of the vortex. Analogies could be drawn between the propeller start-up and the vortex formation process on a piston-cylinder apparatus, but accurate quantification of the "formation number" proved difficult without further understanding. A more comprehensive exploration of the parameter space in a future study, for example on the ramp up profile $\Omega(t)$ or propeller diameter D_p, could give us further insight into the underlying mechanisms and universalities of the phenomenon.

Chapter 10

CONCLUDING REMARKS & FUTURE WORK

Small-scale unmanned aerial vehicles have garnered widespread attention in the past few decades, serving as indispensable tools in a broad range of civil and military applications where manned missions may not be feasible due to cost, safety, or space constraints. This is a culmination of technological advances on multiple fronts, including but not limited to accurate dynamics modeling, robust flight control algorithms, lightweight composite materials, high-performance batteries, and miniature sensors.

A novel "co-rotating prop-shroud" concept is proposed, and its flow physics is investigated in air and water at similar Re. Thrust and torque measurements revealed that the prop-shroud configuration can achieve hover FM values comparable to the unshrouded configuration, and feasibly outperform it with further geometric optimization and the use of more lightweight materials in the manufacturing process. The best case tested had a NACA 9415 shroud profile with $h/c = 1$ (shroud chord equal to blade chord), angled outward at $\beta = 15^\circ$ such that the interior of the shroud forms a converging nozzle.

Although the unshrouded propeller and best-case shrouded propeller described above had nearly identical thrust and torque curves, time- and phase-averaged DPIV analysis illuminated significant differences in their velocity and vorticity distributions. The strength and streamwise persistence of blade tip vortices are attenuated by the shroud, suggesting reduced acoustic noise levels. At the intake, the shroud increased the induced streamwise velocity by over 30% and entrained more fluid radially inward from the outer region. In the near wake, it eliminated the contraction and acceleration of the flow. Momentum analysis of the jet assuming 2D axisymmetric flow showed that it was 20% higher than the measured thrust at the outlet and decayed rapidly downstream. Turbulent fluctuations did not fully account for this momentum imbalance, so important future work involves measuring the out-of-plane velocity component to better understand the 3D flow structures.

A key limitation of experimental visualization techniques is optical access to the flow inside the shroud. With 3D printing technology, it may be possible to create prototypes from transparent material with matching refractive index to the ambient

fluid (e.g., water, oil, etc.) in the near future. Alternatively, the interior flow may be resolved by leveraging computational approaches. This could also provide access to the surface pressure and shear stress distributions, which would be extremely difficult to obtain experimentally for a rapidly rotating object.

The unsteady vortex dynamics of the propeller startup process was also investigated. Pathline visualizations revealed the formation of a single, approximately axisymmetric vortex ring structure that is separate from the helical tip vortex structure. This motivated analogies to be drawn between this phenomenon and vortex ring formation on the well-studied piston-cylinder apparatus. Quantitative methods were developed to track the vortex propagation and show a limit to its growth. This invoked the concept of dimensionless formation time, and a model was developed such that the circulation contained in the vortex saturates around $\hat{T} \approx 4$, following the results in (Gharib, Rambod, and Shariff, 1998). However, large uncertainties remain in the quantification of formation number, requiring further exploration of the parameter space in search of unifying trends. Various numerical and experimental studies have been able to manipulate the value of the vortex formation number (Rosenfeld, Rambod, and Gharib, 1998; Mohseni, Ran, and Colonius, 2001; Dabiri and Gharib, 2004), and signs of optimal vortex formation have also been observed in biological propulsion (Dabiri, 2009). Thus, a deeper understanding of this vortex shedding mechanism for the propeller can drive future optimizations of the blade and shroud geometry for propulsive efficiency.

The scope of this present study was limited to an isolated propeller in a quiescent fluid. To further mature this concept toward application on real vehicles, its performance in the presence of a freestream along the axial (e.g., VTOL) and normal (e.g., forward flight) directions should be investigated. Rotor-rotor interactions and ground effects should be characterized as well, as these behaviors for a rotating shroud may be completely different from those of a conventional stationary shroud.

According to a forecast by the Teal Group, worldwide UAV expenditures over the next decade may reach as high as 89 billion USD (Cai, Dias, and Seneviratne, 2014). As the technology continues to expand to new applications, the design space and performance trade-offs become increasingly complex. Thus, linking the fundamental aerodynamics of novel configurations to various performance characteristics and metrics is critical to the decision-making process. The co-rotating prop-shroud concept explored in this thesis offers a unique set of aerodynamic and engineering benefits for MAVs that makes it a promising alternative to conventional shrouded

and unshrouded configurations.

BIBLIOGRAPHY

AirfoilTools (2022). *NACA 4 digit airfoil generator*. http://airfoiltools.com/airfoil/naca4digit.

Attinello, J. (1961). "Design and Engineering Features of Flap Blowing Installations". In: *Boundary Layer and Flow Control: Its Principles and Application*. Ed. by G.V. Lachmann. New York: Pergamon Press.

Aviation History (1932). *Caproni Stipa from front*. https://upload.wikimedia.org/wikipedia/commons/f/f3/Caproni_Stipa_from_front.jpg. Photo taken in 1932 and scanned from *Aviation History* magazine, March 2010, p.19.

Barlow, J.B., Rae, W.H., and Pope, A. (1999). "Boundary Corrections I-III". In: *Low-speed Wind Tunnel Testing*. New York, NY: John Wiley & Sons, pp. 328–443.

Bright, M., Korntheuer, A., Komadina, S., and Lin, J. (2013). "Development of Advanced High Lift Leading Edge technology for laminar flow wings". In: *51st AIAA Aerospace Sciences including the New Horizons Forum and Aerospace Exposition*. Grapevine, TX: AIAA. DOI: 10.2514/6.2013-211.

Busemann, A. (1935). "Aerodynamischer Auftrieb bei Überschallgeschwindigkeit". In: *Fifth Volta Congress*. Rome, Italy: Royal Academy of Science.

Cai, G., Dias, J., and Seneviratne, L. (2014). "A Survey of Small-Scale Unmanned Aerial Vehicles: Recent Advances and Future Development Trends". In: *Unmanned Systems* 2.2, pp. 175–199. DOI: 10.1142/S2301385014300017.

Carlton, J.S. (2007). "The starting vortex". In: *Marine Propellers and Propulsion, 2nd Edition*. Burlington, MA: Elsevier, pp. 146–147.

Cattafesta, L.N. and Sheplak, M. (2011). "Actuators for active flow control". In: *Annual Review of Fluid Mechanics* 43.1, pp. 247–272. DOI: 10.1146/annurev-fluid-122109-160634.

Chang, C.-C., Hsiau, Y.-C., and Chu, C.-C. (1993). "Starting vortex and lift on an airfoil". In: *Physics of Fluids A: Fluid Dynamics* 5.11, pp. 2826–2830. DOI: 10.1063/1.858745.

Chekab, M.A.F., Ghadimi, P., Djeddi, S., and Soroushan, M. (2013). "Investigation of Different Methods of Noise Reduction for Submerged Marine Propellers and Their Classification". In: *American Journal of Mechanical Engineering* 1.2, pp. 34–42. DOI: 10.12691/ajme-1-2-3.

Chen, C., Seele, R., and Wygnanski, I. (2012). "Separation and Circulation Control on an Elliptical Airfoil by Steady Blowing". In: *AIAA Journal* 50.10, pp. 2235–2247. DOI: 10.2514/1.J051538.

Chen, C., Seele, R., and Wygnanski, I. (2013). "Flow Control on a Thick Airfoil Using Suction Compared to Blowing". In: *AIAA Journal* 51.6, pp. 1462–1472. DOI: 10.2514/1.J052098.

Chen, C., Zakharin, B., and Wygnanski, I. (2008). "On the Parameters Governing Fluidic Control of Separation and Circulation". In: *46th AIAA Aerospace Sciences Meeting and Exhibit*. Reno, NV: AIAA. DOI: 10.2514/6.2008-629.

Clemmons, M.G. (1992). "Antitorque Safety and the RAH-66 Fantail". In: *American Helicopter Society 48th Annual Forum Proceedings*. Washington, D.C., pp. 169–175.

Dabiri, J.O. (2009). "Optimal vortex formation as a unifying principle in biological propulsion". In: *Annual Review of Fluid Mechanics* 41.1, pp. 17–33. DOI: 10.1146/annurev.fluid.010908.165232.

Dabiri, J.O. and Gharib, M. (2004). "Delay of vortex ring pinchoff by an imposed bulk counterflow". In: *Physics of Fluids* 16.4, pp. L28–30. DOI: 10.1063/1.1669353.

Davidson, I.M. (1956). "The jet flap". In: *Aeronautical Journal* 60.541, pp. 25–50. DOI: 10.1017/S0368393100132389.

Dino, J. and Dunbar, B. (2008). *Life on Earth - Wind Tunnels*. https://www.nasa.gov/centers/ames/research/lifeonearth/lifeonearth-windtunnels.html.

Dougherty, C.J. (May 2022). "On the Experimental Simulation of Atmospheric-Like Disturbances Near the Surface". PhD thesis. Pasadena, CA: California Institute of Technology.

Elsberry, K., Loeffler, J., Zhou, M.D., and Wygnanski, I. (2000). "An experimental study of a boundary layer that is maintained on the verge of separation". In: *Journal of Fluid Mechanics* 423, pp. 227–261. DOI: 10.1017/S0022112000001828.

"ESDU 01005" (2001). In: *Effect of geometry on low speed pitch-break characteristics of swept wings*. IHS ESDU.

Fetter, A.L. (1974). "Translational velocity of a classical vortex ring". In: *Physical Review A* 10.5, pp. 1724–1727. DOI: 10.1103/PhysRevA.10.1724.

Fletcher, H.S. (1957). *Experimental Investigation of Lift, Drag and Pitching Moment of Five Annular Airfoils*. Tech. rep. TN 4117. Langley Memorial Aeronautical Laboratory, Langley Field, VA: National Advisory Committee for Aeronautics.

Furlong, G.C. and McHugh, J.G. (Jan. 1957). *A summary and analysis of the low-speed longitudinal characteristics of swept wings at high Reynolds number*. Tech. rep. 1339. NACA, pp. 1391–1539.

Ganesh, V.V.S., Chakkirala, A.B., Thote, S.P., and Bharadwaj, K.K. (2022). "A comparative analysis of sweeping jet actuators". In: *Materials Today: Proceedings* 68, pp. 2348–2354. DOI: 10.1016/j.matpr.2022.09.101.

Gaster, M., Kit, E., and Wygnanski, I. (1985). “Large-scale structures in a forced turbulent mixing layer”. In: *Journal of Fluid Mechanics* 150, pp. 23–39. DOI: 10.1017/S0022112085000027.

Gharib, M., Hirsch, D., Rider, S., and Wygnanski, I. (2016). *MOBLE Unsteady Blowing (UB) Final Report*. Internal report to Northrop Grumman.

Gharib, M., Rambod, E., and Shariff, K. (1998). “A universal time scale for vortex ring formation”. In: *Journal of Fluid Mechanics* 360, pp. 121–140. DOI: 10.1017/S0022112097008410.

Gonzalez, C. and Taha, H.E. (2022). “A variational theory of lift”. In: *Journal of Fluid Mechanics* 941, A58. DOI: 10.1017/jfm.2022.348.

Graff, E. (2013). *Lucas Wind Tunnel Acquisition Uncertainty Analysis*. Internal report.

Gursul, I., Wang, Z., and Vardaki, E. (2007). “Review of flow control mechanisms of leading-edge vortices”. In: *Progress in Aerospace Sciences* 43.7-8, pp. 246–270. DOI: 10.1016/j.paerosci.2007.08.001.

Han, G., Zhou, M. de, and Wygnanski, I. (2006). “On streamwise vortices and their role in the development of a curved wall jet”. In: *Physics of Fluids* 18.9. DOI: 10.1063/1.2353403.

Hirsch, D.G. (May 2017). “Experimental and Theoretical Study of Active Flow Control”. PhD thesis. Pasadena, CA: California Institute of Technology.

Hornung, H. (1992). “Performance data of the new free-piston shock tunnel at GALCIT”. In: *28th Joint Propulsion Conference and Exhibit*. Nashville, TN: AIAA. DOI: 10.2514/6.1992-3943.

Hrishikeshavan, V., Black, J., and Chopra, I. (2014). “Design and Performance of a Quad-Shrouded Rotor Micro Air Vehicle”. In: *Journal of Aircraft* 51.3, pp. 779–791. DOI: 10.2514/1.C032463.

InsideRobotics (2017). *Expert predicts 1 billion drones in world by 2030*. https://www.insiderobotics.com.au/technology/articles-technology/Expert-predicts-1-billion-drones-in-world-by-2030/. Accessed: 2022-11-12.

Johnson, W. (1980). “Vertical Flight I”. In: *Helicopter Theory*. New York, NY: Dover Publications, Inc., pp. 28–91.

Joukowsky, N. (1910). “Uber die Kunturen der Tragflachen der Drachenflieger”. In: *Aeitschrift fur Flugtechnik and Motorluftschiffahrt* 1, pp. 281–284.

Kasula, S. (2019). *What Has the Evolution of Aircraft Propellers Involved?* https://www.acessystems.com/what-has-the-evolution-of-aircraft-propellers-involved/. Accessed: 2022-11-28.

Katz, Y., Seifert, A., and Wygnanski, I. (1990). “On the evolution of the turbulent spot in a laminar boundary layer with favourable pressure gradient”. In: *Journal of Fluid Mechanics* 221, pp. 1–22. DOI: 10.1017/S0022112090003469.

Kuchemann, D. (1956). *A simple method for calculating the span and chordwise loading on straight and swept wings of any given aspect ratio at subsonic speeds*. Tech. rep. 2935. London, UK: Aeronautical Research Council.

Lentink, D., Dickson, W.B., Van Leeuwen, J.L., and Dickinson, M.H. (2009). "Leading-Edge Vortices Elevate Lift of Autorotating Plant Seeds". In: *Science* 324.5933, pp. 1438–1440. DOI: 10.1126/science.1174196.

Levy, D. and Seifert, A. (2009). "Simplified dragonfly airfoil aerodynamics at Reynolds numbers below 8000". In: *Physics of Fluids* 21.7. DOI: 10.1063/1.3166867.

Lucas, N., Taubert, L., Woszidlo, R., Wygnanski, I., and McVeigh, M. (2008). "Discrete Sweeping Jets as Tools for Separation Control". In: *4th Flow Control Conference*. Seattle, WA: AIAA. DOI: 10.2514/6.2008-3868.

Malavard, L. (1961). "Application of the rheoelectric analogy for the jet flap wing of finite span". In: *Boundary Layer and Flow Control: Its Principles and Application*. Ed. by G.V. Lachmann. New York: Pergamon Press.

Malgoezar, A.M., Vieira, A., Snellen, M., Simons, D.G., and Veldhuis, L.L. (2019). "Experimental characterization of noise radiation from a ducted propeller of an unmanned aerial vehicle". In: *International Journal of Aeroacoustics* 18.4-5, pp. 372–391. DOI: 10.1177/1475472X19852952.

Margalit, S., Greenblatt, D., Seifert, A., and Wygnanski, I. (2005). "Delta wing stall and roll control using segmented piezoelectric fluidic actuators". In: *Journal of Aircraft* 42.3, pp. 698–709. DOI: 10.2514/1.6904.

McVeigh, M.A., Nagib, H., Wood, T., and Wygnanski, I. (2011). "Full-Scale Flight Tests of Active Flow Control to Reduce Tiltrotor Aircraft Download". In: *Journal of Aircraft* 48.3, pp. 786–796. DOI: 10.2514/1.46956.

Mitchell, A.M. and Delery, J. (2001). "Research into vortex breakdown control". In: *Progress in Aerospace Sciences* 37.4, pp. 385–418. DOI: 10.1016/S0376-0421(01)00010-0.

Mohseni, K., Ran, H., and Colonius, T. (2001). "Numerical experiments on vortex ring formation". In: *Journal of Fluid Mechanics* 430, pp. 267–282. DOI: 10.1017/S0022112000003025.

Mueller, T.J. (1999). "Aerodynamic Measurements at Low Reynolds Numbers for Fixed Wing Micro-Air Vehicles." In: *Development and Operation of UAVs for Military and Civil Applications*. Rhode-Sainte-Genese, Belgium: RTO AVT.

Mujires, F.T., Johansson, L.C., Barfield, R., Wolf, M., Spedding, G.R., and Hedenstrom, A. (2008). "Leading-Edge Vortex Improves Lift in Slow-Flying Bats". In: *Science* 319.5867, pp. 1250–1253. DOI: 10.1126/science.1153.

Nagib, H., Kiedaisch, J., Reinhard, P., and Demanett, B. (2006). "Control Techniques for Flows with Large Separated Regions: A New Look at Scaling Parameters". In: *3rd AIAA Flow Control Conference*. San Francisco, CA: AIAA. DOI: 10.2514/6.2006-2857.

NASA Glenn Research Center (2021). *Whirling arms and the first wind tunnels*. https://www.grc.nasa.gov/www/k-12/WindTunnel/history.html.

Neuendorf, R., Lourenco, L., and Wygnanski, I. (2004). "On large streamwise structures in a wall jet flowing over a circular cylinder". In: *Physics of Fluids* 16.7. DOI: 10.1063/1.1703531.

Niehuis, R. and Bitter, M. (2021). "The High-Speed Cascade Wind Tunnel at the Bundeswehr University Munich after a Major Revision and Upgrade". In: *International Journal of Turbomachinery, Propulsion and Power* 6.4, p. 41. DOI: 10.3390/ijtpp6040041.

Oster, D. and Wygnanski, I. (1982). "The forced mixing layer between parallel streams". In: *Journal of Fluid Mechanics* 123, pp. 91–130. DOI: 10.1017/S0022112082002973.

Otto, C., Little, J.C., Rafferty, B., and Woszidlo, R. (2022). "Momentum Coefficient Governing Discrete Jet Actuation for Separation Control". In: *AIAA Journal* 60.2, pp. 809–822. DOI: 10.2514/1.J060680.

Pereira, J.L. (2008). "Hover and wind-tunnel testing of shrouded rotors for improved micro air vehicle design". PhD thesis. College Park, MD: University of Maryland, College Park.

Poisson-Quinton, P. (1948). "Recherches theoretiques et experimentales sur le control de la couche limite". In: *Proceedings of the Seventh International Congress for Applied Mechanics*. South Kensington, London.

Poisson-Quinton, P. and Lepage, L. (1961). "Survey of French research on the control of boundary layer circulation". In: *Boundary Layer and Flow Control: Its Principles and Application*. Ed. by G.V. Lachmann. New York: Pergamon Press.

Polhamus, E.C. (1966). *A concept of the vortex lift of sharp-edge delta wings based on a leading-edge-suction analogy*. Tech. rep. NASA-TN-D-3767. Hampton, VA: NASA Langley Research Center.

Prandtl, L. (1936). *Formation of vortices in water currents - 1. Formation of vortices and its artificial influencing*. https://doi.org/10.3203/IWF/C-1. silent film.

Prandtl, L. and Tietjens, O.G. (1934). "Consecutive stages of flow round airfoil starting from rest". In: *Applied Hydro- and Aeromechanics*. New York, NY: McGraw-Hill, pp. 296–301.

Rosenfeld, M., Rambod, E., and Gharib, M. (1998). "Circulation and formation number of laminar vortex rings". In: *Journal of Fluid Mechanics* 376, pp. 297–318. DOI: 10.1017/S0022112098003115.

Roy, S., Das, B., and Biswas, A. (2022). "A comprehensive review of the application of bio-inspired tubercles on the horizontal axis wind turbine blade". In: *International Journal of Environmental Science and Technology*. DOI: 10.1007/s13762-021-03784-3.

Sacks, A.H. and Burnell, J.A. (1962). "Ducted propellers - a critical review of the state of the art". In: *Progress in Aeronautical Sciences* 3, pp. 85–135. DOI: 10.1016/B978-1-4831-9984-9.50005-8.

Sayed, Y.E., Beck, N., Kumar, P., Semaan, R., and Radespiel, R. (2018). "Challenges in the Experimental Quantification of the Momentum Coefficient of Circulation Controlled Wings". In: *New Results in Numerical and Experimental Fluid Mechanics XI*. Springer International Publishing, pp. 533–543. DOI: 10.1007/978-3-319-64519-3_48.

Scavini, Julien (2011). *Airbus A32X family*. https://upload.wikimedia.org/wikipedia/commons/5/5b/Airbus_A32X_family_v1.0.png. CC BY-SA 3.0.

Schmidt, H.J., Woszidlo, R., Nayeri, C., and Paschereit, C.O. (2016). "Fluidic oscillators for bluff body drag reduction in water". In: *SciTech Forum*. 54th AIAA Aerospace Sciences Meeting. San Diego, CA: AIAA. DOI: 10.2514/6.2016-0591.

Seele, R., Graff, E., Lin, J., and Wygnanski, I. (2013). "Performance enhancement of a vertical tail model with sweeping jet actuators". In: *51st AIAA Aerospace Sciences Meeting including the New Horizons Forum and Aerospace Exposition*. Grapevine, TX: AIAA. DOI: 10.2514/6.2013-411.

Seifert, A., Bahcar, T., Koss, D., Shepshelovich, M., and Wygnanski, I. (1993). "Oscillatory blowing: a tool to delay boundary-layer separation". In: *AIAA Journal* 31.11. DOI: 10.2514/3.49121.

Semaan, R. (2020). "The uncertainty of the experimentally-measured momentum coefficient". In: *Experiments in Fluids* 61, pp. 248–. DOI: 10.1007/s00348-020-03076-5.

Shariff, K. and Leonard, A. (1992). "Vortex Rings". In: *Annual Review of Fluid Mechanics* 24.1, pp. 235–279. DOI: 10.1146/annurev.fl.24.010192.00131.

Spence, D.A. (1958a). "Some simple results for a two-dimensional jet-flap aerofoil". In: *Aeronautical Quarterly* 9.4, pp. 395–406. DOI: 10.1017/S0001925900010799.

Spence, D.A. (1958b). "The lift on a thin aerofoil with a jet-augmented flap". In: *Aeronautical Quarterly* 9.3, pp. 287–299. DOI: 10.1017/S0001925900010726.

Stamhuis, E.J. and Videler, J.J. (1995). "Quantitative flow analysis around aquatic animals using laser sheet particle image velocimetry". In: *The Journal of Experimental Biology* 198, pp. 283–294. DOI: 10.1242/jeb.198.2.283.

Stipa, L. (1932). *Experiments with intubed propellers*. Tech. rep. TM 655. Washington, D.C.: National Advisory Committee for Aeronautics.

Taha, H.E., Kiani, M., Hedrick, T.L., and Greeter, J.S.M. (2020). “Vibrational control: A hidden stabilization mechanism in insect flight”. In: *Science Robotics* 5.46. DOI: 10.1126/scirobotics.abb1502.

Tang, J., Viieru, D., and Shyy, W. (2007). “A Study of Aerodynamics of Low Reynolds Number Flexible Airfoils”. In: *37th AIAA Fluid Dynamics Conference and Exhibit*. Miami, FL: AIAA. DOI: 10.2514/6.2007-4212.

Whalen, E.A., Lacy, D.S., Lin, J.C., Andino, M.Y., Washborn, A.E., Graff, E.C., and Wygnanski, I.J. (2015). “Performance enhancement of a full-scale vertical tail model equipped with active flow control”. In: *53rd AIAA Aerospace Sciences Meeting*. Kissimmee, FL: AIAA. DOI: 10.2514/6.2015-0784.

Whalen, E.A., Spoor, M., Vijgen, P.M., Tran, J., Shmilovich, A., Lin, J.C., and Andino, M. (2016). “Full-scale flight demonstration of an active flow control enhanced vertical tail”. In: *8th AIAA Flow Control Conference*. Washington, D.C.: AIAA. DOI: 10.2514/6.2016-3927.

Willert, C., Schulze, M., Waltenspul, S., Schanz, D., and Kompehnhans, J. (2019). “Prandtl’s flow visualization film C1 revisited”. In: *13th International Symposium on Particle Image Velocimetry*. Munich, Germany.

Woszidlo, R. and Little, J.C. (2021). “Recommended Practices for Characterization and Documentation of Active Flow Control Actuators”. In: *AIAA SciTech 2021 Forum*. virtual event: AIAA. DOI: 10.2514/6.2021-2002.

Wygnanski, I. and Newman, B.G. (1964). “The Effect of Jet Entrainment on Lift and Moment for a Thin Aerofoil with Blowing”. In: *Aeronautical Quarterly* 15.2, pp. 122–150. DOI: 10.1017/S0001925900003085.

Yang, X., Liu, T., Ge, S., Rountree, E., and Wang, C. (2021). “Challenges and key requirements of batteries for electric vertical takeoff and landing aircraft”. In: *Joule* 5.7, pp. 1644–1659. DOI: 10.1016/j.joule.2021.05.001.

Zhang, T. and Barakos, G.N. (2020). “Review on ducted fans for compound rotorcraft”. In: *The Aeronautical Journal* 124.1277, pp. 941–974. DOI: 10.1017/aer.2019.164.

Zhou, M.D., Heine, C., and Wygnanski, I. (1996). “The effects of excitation on the coherent and random motion in a plane wall jet”. In: *Journal of Fluid Mechanics* 310, pp. 1–37. DOI: 10.1017/S0022112096001711.